Optimization of C- and L-band Synthetic Aperture Radar for All-Season Rift Detection: A Case Study of the Larsen C Ice Shelf

by

Kali Ann McDougall

BSc., University of Victoria, 2022

A thesis submitted to the University of Victoria in partial fulfillment of the requirements for the degree of

MASTER OF SCIENCE

in the Department of Geography

University of Victoria

Optimization of C- and L-band Synthetic Aperture Radar for All-Season Rift Detection: A Case Study of the Larsen C Ice Shelf

by

Kali Ann McDougall

BSc., University of Victoria, 2022

Supervisory Committee

Dr. Randall K. Scharien, Supervisor

(Department of Geography)

Dr. David E. Atkinson, Department Member

(Department of Geography)

Abstract

More than half of ice mass loss from Antarctica occurs through calving of large tabular icebergs along rifts at the outer margins of ice shelves, which can lead to ice shelf destabilization and collapse. Synthetic aperture radar (SAR) sensors provide the greatest potential utility for the study of calving-related mechanisms by offering year-round, all-weather imaging and penetration of surface snow. To fully utilize SAR for rift detection, the constraints on fracture detectability posed by surface melt, and radar frequency and polarization, must be characterized. We examined dual-pol (HH and HV) Sentinel-1 C-band frequency (5.4 GHz) and PALSAR-2/SAOCOM L-band frequency (1.2 GHz) SAR images of the Gipps Ice Rise rift system on the Larsen C Ice Shelf during the 2020-2021 melt year. Rift geometry was characterized using the ATL06 land ice height product from ICESat-2, and surface melt was identified using a fixed threshold applied to Advanced Scatterometer (ASCAT) imagery. A Kolmogorov-Smirnov test was performed on ice type classes to determine their spectral separability in SAR images throughout the melt year. To further evaluate the performance of different SAR configurations on rift detection, pixel-based and image object-based Random Forest classifications were tested during late winter and late melt conditions. Overall, rifts that are filled with mélange are difficult to discriminate from the surrounding firn across seasons. Greater consistency in rift detection is found using L-band frequency compared to C-band, with enhanced L-band capability in winter in the presence of a thick ice mélange layer. In general, HV polarization provides greater separability between ice types compared to HH polarization and improves the detection of rifts through most of the melt year, apart from the late melt stage. Lastly, an object-based approach is superior to a pixel-based approach for the application of machine learning to automate rift detection using SAR. Optimizing the full potential of C- and L-band SAR for rift detection, and the development of an object-based machine learning detection method, will lay the groundwork for future automated rift detection and calving studies. Here a bottom-up assessment of SAR-based rift detection is presented, which provides a useful foundation for future algorithm development and the implementation of a standardized rift detection method.

Table of Contents

List of Tables

List of Figures

List of Abbreviations

ALOS	Advanced Land Observing Satellite
AP	Antarctic Peninsula
ASCAT	Advanced Scatterometer
ATLAS	Advanced Topographic Laser Altimeter System
CARD4L	CEOS Analysis Ready Data for Land
CEOS	Committee on Earth Observation Satellites
DEM	Digital Elevation Model
EM	Early Melt
ERA5	European Center for Medium-Range Weather Forecasts (ECMWF) Atmospheric Reanalysis Version 5
ESA	European Space Agency
F	Firn (Class)
FU	Freeze Up
GLCM	Grey-Level Co-occurrence Matrix
GIR	Gipps Ice Rise
GPR	Ground Penetrating Radar
GRD	Ground Range Detected
H	Horizonal transmit or receive polarization
ICESat	Ice Cloud and Land Elevation Satellite
InSAR	Interferometric Synthetic Aperture Radar
IW	Interferometric Wide Swath
KS	Kolmogorov-Smirnov
LCIS	Larsen C Ice Shelf
LM	Late Melt
LW	Late Winter
MFR	Mélange-Filled Rift (Class)
ML	Machine Learning
MO	Melt Onset

NRB	Normalized Radar Backscatter
OBIA	Object-Based Image Analysis
OWR	Open-Water Rift (Class)
PALSAR	Phased Array L-band Synthetic Aperture Radar
QGIS	Quantum Geographic Information System (GIS)
RF	Random Forest
REMA	Reference Elevation Model of Antarctica
ROI	Region of Interest
SAOCOM	Satelité Argentino de Observación COn Microondas
SAR	Synthetic Aperture Radar
SCP	Scatterometer Climate Record Pathfinder
SLC	Single Look Complex
SIR	Scatterometer Image Reconstruction
SNAP	Sentinel Application Platform
TOPSAR	Terrain Observation with Progressive Scans Synthetic Aperture Radar
V	Vertical transmit or receive polarization

Acknowledgements

I would like to express my gratitude to all those who supported me throughout my thesis and my degree. Thank you to:

My supervisor, Dr. Randy Scharien, for the trust and mentorship. Thank you for the many opportunities, for pushing me to do my best, and for understanding when I couldn't.

Dr. David Atkinson, for the support as a member of my committee, and for the continued guidance and friendship.

Dr. Karen Alley, for fulfilling the role of external examiner and challenging me to think critically during my thesis defense.

ICE Lab team – Aikaterini Tavri, Grant Macdonald, Adrià Blanco-Cabanillas, Kalum Delaney, and Neil Brubacher. Thank you for the advice, camaraderie, and occasional shared misery.

My friends, for believing in me and supporting me through yet another degree.

My mom, for your curiosity, and for believing I can answer your questions better than Google.

Connor, for your encouragement, love, and patience. If we can do this, we can do anything.

Dedicated to Obi, who, at times, was my only hope.

The Force will be with you. Always.

1 Introduction

1.1 Antarctica and the global climate system

The cryosphere – made up of snow cover, permafrost, ice caps, glaciers, sea ice, and ice sheets – plays several critical roles in Earth's climate system. The primary role of the cryosphere is the modulation of global temperatures through the ice-albedo feedback mechanism, which concerns the expansion and shrinkage of sea ice and polar ice sheets and the associated change in reflected solar radiation (Barry & Gan, 2022). Additionally, the exchange of heat and carbon between the land and the atmosphere is also partially controlled by the cryosphere, namely through permafrost and seasonally frozen ground (Barry & Gan, 2022). The cryosphere also modulates the global hydrologic cycle due to the storage and release of water (Barry & Gan, 2022). Ice sheets contain the greatest amount of freshwater, holding ~77% of the global total; in particular, the Antarctic Ice Sheet holds more than 90% of global glacier ice volume and 60% of global freshwater, with a 58 m sea-level rise potential (Swithinbank et al., 1988; Fretwell et al., 2013).

As the coldest, driest, and windiest continent, Antarctica plays a critical role in regulating Earth's climate; through its high albedo and interactions with atmospheric and oceanic circulation systems, Antarctica's ice sheets are a key component of global heat exchange. Changes in Antarctic ice dynamics, such as accelerated melting, rifting, and ice shelf collapse, have the potential to contribute significantly to sea-level rise, with widespread implications for coastal regions worldwide. In addition to its influence on sea level, Antarctica's floating ice shelves act as barriers that slow the flow of grounded land ice to the ocean (Schoof, 2007; DeConto & Pollard, 2016). Since ice shelves are exposed to both warming air and the warming ocean, they respond to temperature changes faster than the adjacent ice sheets (Shah et al., 2020). The sensitivity of ice shelves to changes in atmospheric and oceanic temperatures makes them critical indicators of the impacts of climate change. Therefore, understanding and monitoring changes in the Antarctic Ice Sheet is essential for improving climate models and predicting how Antarctica will respond to global warming.

1.2 Need for monitoring rift development

The disintegration of the Larsen A, Larsen B, and Wilkins Ice Shelves, and several major calving events since the 1990s, have highlighted the vulnerability of the Antarctic Ice Sheet to changing atmospheric and oceanic conditions (Larour et al., 2021; Walker et al., 2021; Qi et al., 2021; Francis et al., 2022; Davison et al., 2023; Marsh et al., 2023). Rift development within Antarctic ice shelves can be an early indicator of structural weakening and potential collapse (Massom et al., 2018). Rifts are elongated fractures that propagate through the entire thickness of ice shelves, often leading to the detachment of massive icebergs. Loss of ice at the shelf front reduces the internal resistive (a.k.a., "backstress") forces in an ice sheet, lowering its resistance to flow and causing dynamic thinning and mass loss (DeConto & Pollard, 2016). These mechanisms can eventually result in complete collapse of the ice shelf which will significantly accelerate the seaward flow of grounded ice (Schoof, 2007; DeConto & Pollard, 2016; Massom et al., 2018). Monitoring rift development is therefore essential for understanding the processes driving ice shelf instability. Accurate monitoring of rift activity requires detection of rifts at high temporal and spatial resolutions and requires detection to be maintained regardless of ice surface conditions. This will enable tracking of rift propagation over time and assessments of how atmospheric and oceanic conditions impact rift formation and growth. Additionally, monitoring rift activity will locate the orientation and distribution of stresses within an ice shelf, allowing better predictions of where fractures may form and how they might propagate. Developing robust methodologies for identifying and analyzing rift features year-round will improve our ability to forecast ice shelf collapse, inform global sea-level rise projections, and support international efforts to mitigate the impacts of climate change.

Due to the relative inaccessibility and harsh environmental conditions of glaciated regions, monitoring of ice sheets is currently done primarily through satellite remote sensing. Synthetic aperture radar (SAR) sensors are particularly advantageous for rift detection and monitoring by providing year-round, all-weather imaging capabilities. Additionally, SAR sensors offer a clear view of rift structure by providing surface penetration, therefore revealing features that are buried in snow. The penetration depth of SAR signals is dependent on SAR imaging parameters such as frequency, polarization, and incidence angle, and the surface medium. Under ideal conditions (i.e., smooth, dry, cold ice and snow), high frequencies such as C-band can reach penetrate up to 10 m

below the surface, while low frequency L-band can penetrate up to 100+ m (Rignot et al., 2001). The accuracy of rift detection is therefore constrained by SAR imaging parameters, the spatial resolution of the scene, and the physical and electrical properties of the surface affecting the interaction of microwaves (i.e., roughness, moisture content; Moreira et al., 2013). Given these constraints, an investigation into which sensor and surface parameters provide the greatest contrast between fractures and their surroundings is required to optimize the use of SAR in rift studies. A more detailed overview of SAR and its constraints and applications is given in Section 2.5.2 and 2.6 below.

1.3 Research objectives

Given the relative dearth of detailed studies on the constraints of rift detection on SAR imaging, the overall goal of this research is to advance the utility of C- and L-band SAR to detect rifts in ice shelves. The objectives of this research are as follows:

1. Evaluate the rift behaviour of the LC2017 rift prior to the A68 calving event from the Larsen C Ice Shelf using C- and L-band SAR.

The first objective of this study is to use C- and L-band SAR as the basis for evaluating rift behaviors preceding the calving of iceberg A68 from the Larsen C Ice Shelf. This objective will involve visual inspections of the size and relative location of the LC2017 rift in the years prior to detachment using optical, C- and L-band SAR images. This calving event, and the development of the rift during the preceding years, has been well-documented using optical and C-band SAR imagery. However, this objective aims to evaluate which information is retrievable from different satellite sensors, and whether the use of lower frequency SAR, i.e., L-band rather than C-band, can provide enhanced information about the rift structure that has not been previously determined.

2. Examine how SAR frequency and polarization, fracture geometry, and surface melt-freeze conditions influence the detection of rifts in SAR imagery.

The second objective of this study is to examine the combined influences of SAR frequency and polarization, fracture geometry, and surface melt-freeze conditions on rift detectability. To understand how rifts appear in SAR imagery under various constraints, the statistical separability of different ice surface types will be compared throughout the melt year using C- and L-band SAR.

Additionally, fractures with different widths and depths will be assessed according to their relative visibility to quantify the effect of rift geometry on rift detection. Understanding how rift visibility is constrained by sensor and surface conditions will allow for future development of improved, automated detection techniques which leverage the most suitable sensor parameters. Furthermore, understanding how the geometry of rifts influences their visibility will provide insight into the limitations and capabilities of SAR-based rift detection.

3. Compare the performance of object- and pixel-based classification techniques for the application of SAR to automated rift detection.

The final objective of this research is to compare the performance of pixel- and object-based classification techniques and assess the proportion of correctly classified rifts. This will build on the results from objective #2 to understand how sensor and surface constraints influence the detectability of rifts with different automated classification techniques. Several different classification techniques and machine learning methods have been used in fracture detection studies, each ranging in performance and ease of application. Therefore, developing a rift detection technique using C- and L-band SAR will allow for implementation of a standardized detection method which operates on widely available data with high temporal resolution. Overall, optimizing SAR for rift detection and mapping will lay the groundwork for future studies into calving mechanisms, particularly in the face of ongoing and improved C-band and L-band SAR missions, and in particular, the launch of the NASA-ISRO (NISAR) L-band mission in 2025.

2 Literature review

2.1 Physical Geography of the Antarctic Ice Sheet

The Antarctic Ice Sheet holds nearly 91.5% of global glacier ice volume on an area of 13.9 million km^2, with approximately 58 m of sea-level rise potential (Swithinbank et al., 1988; Fox & Cooper, 1994; Fretwell et al., 2013; Morlighem et al., 2020). Ice sheet systems have three main components: slow-moving grounded ice, fast-flowing ice streams or outlet glaciers, and floating ice shelves (Bell & Seroussi, 2020). Most Antarctic ice is grounded ice, which maintains contact with the underlying bedrock and reaches ice thicknesses of ~4,800 m in the interior with ice velocities of a few cm yr^{-1} (Rignot et al., 2011; Fretwell et al., 2013). In contrast, fast-flowing ice streams and glaciers transport grounded ice towards the ocean at rates of several km yr^{-1} (Rignot et al., 2011); the presence of water and sediment at the base of these features reduces basal friction and enables their fast flow (Mouginot et al., 2017; Bell & Seroussi, 2020). Lastly, ice shelves are expansive, flat, floating bodies of ice attached to fast-flowing ice streams. While these features do not directly influence global sea levels, they play a critical role in moderating sea-level rise by buttressing the seaward flow of the glaciers and grounded ice that feeds them (Schoof, 2007; Bell & Seroussi, 2020).

Floating glaciers and ice shelves make up 75% of the 43,450 km long Antarctic coastline, with a cumulative area of more than 1.56 million km^2 (Rignot et al., 2013). These ice shelves drain 80% of Antarctica's grounded ice and collect 20% of Antarctic snowfall over 11% of its area (Pritchard et al., 2012; Rignot et al., 2013). The Antarctic continent is broadly divided into three regions: the Antarctic Peninsula (AP), West Antarctica, and East Antarctica. The Transantarctic Mountains separate the West Antarctic Ice Sheet from the East Antarctic Ice Sheet. The AP contains many small outlet glaciers and the Larsen [A-D] ice shelves on the eastern side, next to the Weddell Sea. West Antarctica is characterized by very large ice shelves and low-lying bed elevation – the Ross and Ronne ice shelves have a combined size of > 100,000 km^2, and much of the ice sheet lies on bedrock hundreds to thousands of meters below sea level (Rignot et al., 2013; Fretwell et al., 2013; DeConto & Pollard, 2016). In contrast, much of East Antarctica consists of a thick layer of ice that lies well above sea level, apart from outlet glaciers in Victoria and Wilkes Land, and ice shelves along the northern & eastern coastlines; the East Antarctic Ice Sheet is the

largest and thickest ice sheet in the world (Fretwell et al., 2013). The East Antarctic Ice Sheet has remained relatively stable in the face of climate change (Gardner et al., 2018), while West Antarctica and the AP are experiencing rapid warming and ice mass loss (Vaughan et al., 2003; Bromwich et al., 2013).

Ice in Antarctica flows seaward along a complex set of tributaries that originate near topographic divides (Rignot et al., 2011). Recent ice velocity and thickness measurements estimate Antarctica's contribution to sea-level rise was around 7.6 ± 3.9 mm between 1992-2017, and 13.9 ± 2.0 mm between 1979-2017 (IMBIE, 2018). Under high greenhouse gas emissions, Antarctica has the potential to contribute > 1 m of sea-level rise by the end of 2100 and > 15 m by 2500, thus exceeding contributions from both alpine glaciers and the Greenland Ice Sheet (DeConto & Pollard, 2016). Single glaciers account for 13% of Antarctica's contributions to sea-level rise, with glaciers such as Pine Island and Thwaites contributing 4.8 mm since 1979 – nearly twice the amount contributed from the entire Antarctic Peninsula (Rignot et al., 2019).

2.1.1 Atmospheric and oceanic circulation

Most of the Antarctic interior is classified as a polar desert, receiving just 25 mm yr^{-1} of precipitation (Turner et al., 2019). The highest precipitation rates occur along the western AP, which receives ~985 mm yr^{-1}; spatially averaged accumulation rates on the AP are roughly three and seven times greater than West and East Antarctica, respectively (IMBIE, 2018; Turner et al., 2019). This high spatial variability in precipitation makes many regions in Antarctica dependent on episodic extreme precipitation events to provide the snowfall required to offset mass losses; some regions of the Antarctic Ice Sheet receive 40-60% of their annual precipitation from the largest 10% of precipitation events (Wille et al., 2021). These events mainly occur as atmospheric rivers, which transport high volumes of atmospheric moisture from the lower latitudes (Pohl et al., 2021). While atmospheric river landfalls are relatively infrequent in Antarctica (~1-3 times per year in a given region), they have a significant impact on Antarctic surface mass balance, contributing ~20% of annual snowfall across parts of the Antarctic Ice Sheet and accounting for ~70% of the 1% most intense precipitation events (Wille et al., 2021). In some parts of East Antarctica, atmospheric rivers are responsible for up to 80% of annual snowfall (Wille et al., 2021). Despite their overall positive influence on snowfall accumulation and surface mass balance,

atmospheric rivers can also cause strong melt events as they are associated with warmer, wetter air masses (Pohl et al., 2021). Atmospheric rivers bring warm, dry, downslope winds (foehn winds) to the eastern side of the AP, triggering winter surface melt on AP ice shelves and causing most of the summer melt events over West Antarctica (Pohl et al., 2021).

Atmospheric and oceanic circulation around Antarctica is dominated by the Southern Hemisphere westerlies, which control circulation between 30-60°S (Convey et al., 2009). Westerly winds drive the Antarctic Circumpolar Current – a major component of Antarctic climate and global oceanic circulation (Figure 1, Figure 2). The Antarctic Circumpolar Current forms a boundary between warm subtropical ocean water and colder water near Antarctica's coast, which keeps the continent cold. Additionally, westerly winds create upwelling of relatively warm Circumpolar Deep Water into the continental shelf (Convey et al., 2009). Further to the south, the polar easterlies dominate atmospheric circulation between 60-90°S, thus controlling wind flow over much of the ice sheet interior. These winds are strongly influenced by the topography of the Antarctic continent and tend to be oriented in the direction of the coastline (Neme et al., 2022). Fluctuations in the easterlies near the coast bring about temperature anomalies responsible for warming of the continental shelf; additionally, coastal easterlies influence the strength of the Antarctic Circumpolar Current, and local sea-ice formation and advection (Neme et al., 2022).

Regional climate trends and variability across Antarctica are closely linked to changes in atmospheric circulation over the Southern Hemisphere (Favier et al., 2017); these changes impact ocean circulation and stratification, sea ice concentration and extent, and basal melt of ice shelves (Pritchard et al., 2012; Turner et al., 2015, 2016; Jones et al., 2016). These trends vary in response to fluctuations in the Southern Annular Mode and the El Niño-Southern Oscillation, particularly over West Antarctica (Thomas et al., 2015; Turner et al., 2016a,b; Favier et al., 2017). Positive phases of the Southern Annular Mode and El-Niño are associated with enhanced sea ice formation in the Weddell and Ross Seas, which increases the production of Antarctic Bottom Water (Silvano et al., 2020; Hattermann et al., 2021). The increasing strength of the Southern Annular Mode has also intensified and shifted the westerly winds poleward across the AP and West Antarctica, thus enhancing marine air advection and surface warming, particularly on the northeastern side of the AP (Lefebvre et al., 2004; Bromwich et al., 2012; Grosvenor et al., 2014; Thomas et al., 2015; Favier et al., 2017).

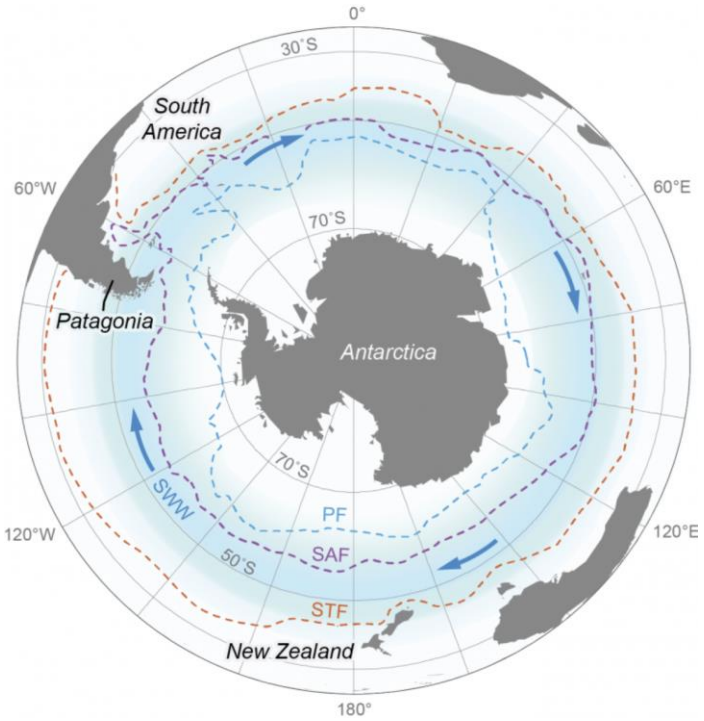

Figure 1. *Synoptic-scale atmospheric circulation patterns around Antarctica. PF: Polar Front, SAF: Sub-Antarctic Front, STF: Sub-Tropical Front, SWW: Southwesterly Winds (Credit: B. Davies, retrieved from Antarctic Glaciers in January 2025).*

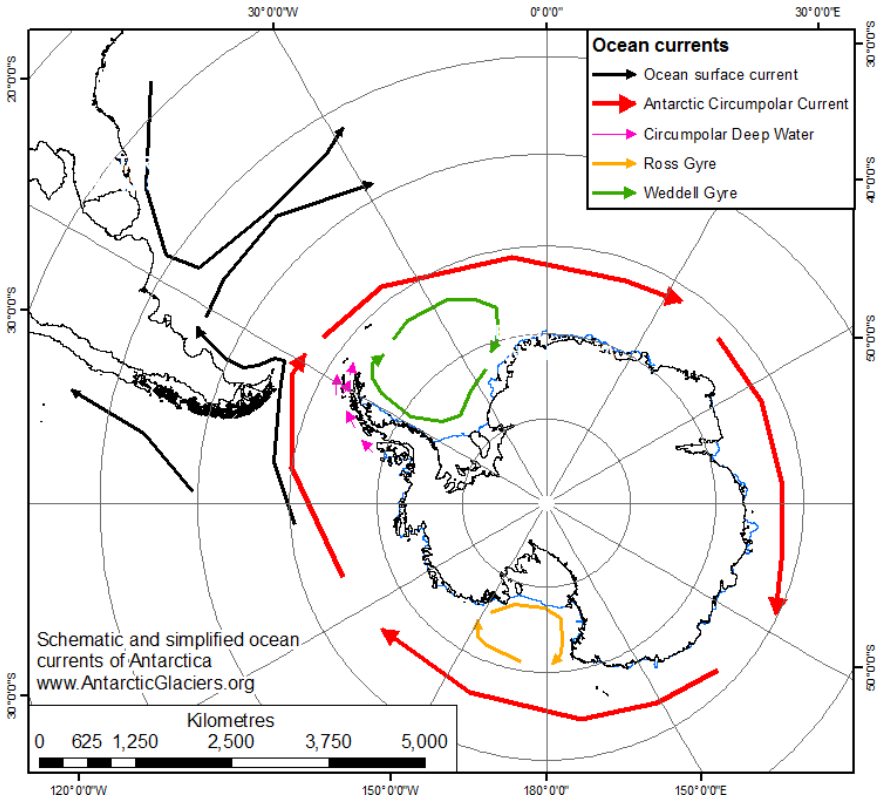

Figure 2. *Ocean currents around Antarctica. Surface speed shown in the background (Credit: B. Davies, retrieved from Antarctic Glaciers in January 2025).*

2.1.2 Sea ice

Sea ice is another major component of the Antarctic energy budget and the global climate system. Sea ice increases surface albedo and provides a barrier to the exchange of heat, momentum (e.g., wind), and mass (e.g., water vapour, CO_2) between the ocean and the atmosphere (He et al., 2016). Fluctuations in sea ice cover influence regional temperature, air pressure, and drive changes in the polar easterlies (Raphael et al., 2011). In autumn, when ice cover is at its maximum, surface temperature and air pressure around Antarctica are higher, and the easterlies are stronger and extend further north (Raphael et al., 2011). This pattern extends into the midlatitudes, strengthening the westerlies between 45-60°S and weakening them between 30-45°S. These responses also occur in the opposite sense during summer, when ice cover is at its minimum. While Arctic sea ice extent (i.e., the cumulative area of all grid cells in a region that have ice concentrations of at least 15%) has been decreasing since the 1980s, Antarctic ice extent showed an opposing trend, increasing from the 1970s to the early 2010s (Parkinson & Cavalieri, 2012). However, since 2015, Antarctic ice extent has experienced a rapid decline, equivalent to ~30 years of ice loss in the Arctic (Parkinson, 2019). Following a record high in 2014, ice extent dropped to a record low in 2017, with seasonal retreat occurring earlier and faster (Parkinson, 2019; Eayrs et al., 2021). This shift in the seasonal sea-ice cycle has changed the nature of its thermodynamic relationships with the atmosphere and ocean. The earlier retreat of sea ice allows more solar radiation to be absorbed by the ocean during the spring, accelerating melt of adjacent ice cover. As a result, the longer ice-free season leads to increased oceanic absorption of radiation during the summer, thus delaying the formation of sea ice in the following autumn (Eayrs et al., 2021).

Sea ice also controls the formation of Antarctic Bottom Water, which is a key component of the global ocean system (Jacobs, 2004). The seasonal cooling and salinification of the sea surface from the formation of sea ice around the continental shelf produces cold, dense waters; this water sinks to the abyssal layer of the ocean and supplies the lower limb of the global overturning circulation (Lumpkin & Speer, 2007; Silvano et al., 2020). Antarctic Bottom Water supplies ~30-40% of the total volume of the ocean and stores heat and carbon dioxide for several centuries, thus regulating atmospheric CO_2 concentrations and ultimately the global climate (Orsi et al., 1999; Johnson et al., 2008; de Lavergne et al., 2017). Key regions of Bottom Water formation are the Weddell and Ross Seas which possess the greatest winter sea ice extent, and low-pressure

systems located to the east of the Ross and Ronne ice shelves which drive sea ice production (Drucker et al., 2011).

2.2 Antarctic mass loss

Mass loss in Antarctica is dominated by the Amundsen and Bellingshausen Sea sectors, Wilkes Land, and the western AP (Rignot et al., 2019). The standard way to measure the health of glaciers and ice sheets is through mass balance estimates; it is the sum of all mass gained through accumulation and mass lost through ablation. While a positive mass balance exists in some regions of the Antarctic Ice Sheet (e.g., Dronning Maud Land), the overall mass balance has been trending negative since the 1970s (Rignot et al., 2019). Net estimates of Antarctic mass balance are -71 ± 53 Gt yr^{-1} from 1992-2011, though this number has increased to -219 ± 43 Gt yr^{-1} from 2012-2017 (Shepherd et al., 2012; IMBIE, 2018). Ice shelf mass balance can be represented as:

$$MB = SMB + DMB$$

where SMB is the surface mass balance, or the net accumulation between precipitation, sublimation, wind-driven snow transport, and liquid water (i.e., rain or melt) that is neither refrozen nor stored within the snowpack (Favier et al., 2017; Figure 3), and DMB is dynamic mass balance, representing losses due to solid ice discharge to the ocean (i.e., calving) and variations in flow velocity caused by basal melting and thinning and thickening of ice. Ice shelf mass balance is generally dominated by ice dynamics (Figure 4), with surface processes playing a comparatively smaller role (Rignot et al., 2011). Of the ~2,000 Gt yr^{-1} of precipitation received on the Antarctic Ice Sheet, over 90% of that mass is removed through solid ice discharge, and the remainder is removed through surface processes and basal melt (Gardner et al., 2018). However, these trends exhibit significant regional variability; dynamic losses are concentrated around West Antarctica and the AP, while surface losses occur mainly around low latitude areas of East Antarctica such as Wilkes Land and Dronning Maud Land (Rignot et al., 2019). Additionally, surface mass balance processes exhibit considerable temporal variability, largely due to fluctuations in snowfall and snowmelt rates across the continent (IMBIE, 2018; Rignot et al., 2019).

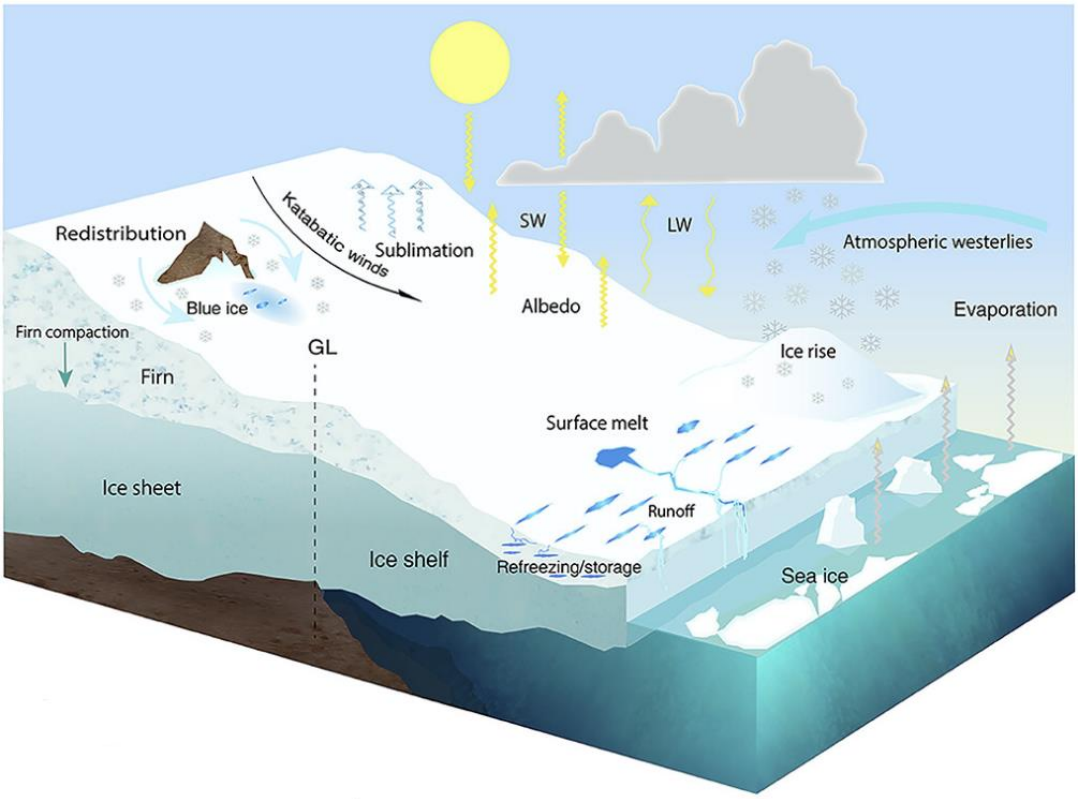

Figure 3. *Surface mass balance processes on Antarctic ice shelves. SW: shortwave, LW: longwave, GL: grounding line (Credit: Lenaerts et al., 2019).*

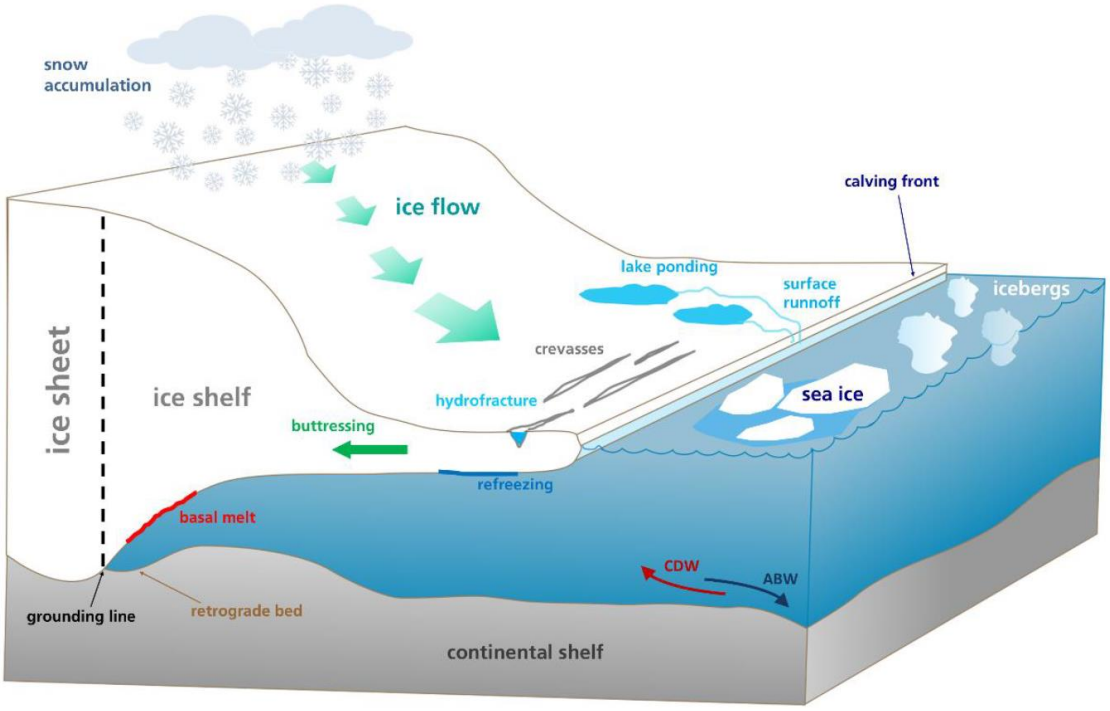

Figure 4. *Ice dynamics processes. Diagram shows the effects of basal melt, surface melt and ponding, hydrofracture, crevassing, and calving. CDW: Circumpolar Deep Water, ABW: Antarctic Bottom Water (Credit: Baumhoer, 2020).*

2.2.1 Ice shelf dynamics

In recent decades, rapid thinning and acceleration of outlet glaciers has increased solid ice discharge from the Antarctic Ice Sheet, with ice sheet elevation decreasing dramatically in the AP, West Antarctica, and in Wilkes Land (Shepherd et al., 2019). This can be attributed to the retreat, disintegration, and thinning of ice shelves and glacier tongues along the coast (Baumhoer, 2020). Floating ice shelves are crucial to the stability of the ice sheet, as they buttress the seaward flow of ice and stabilize marine grounding zones (Depoorter et al., 2013; DeConto & Pollard, 2016, Fürst et al., 2016). The loss of ice shelves therefore enhances discharge from tributary glaciers, which directly contributes to global sea-level rise (Schoof, 2007).

Ice shelves exhibit highly variable rates of areal change, and the location of the calving front follows a cycle of alternating retreat and advance. Therefore, the calving front is rarely stationary and reflects behaviours ranging from steady advance to catastrophic collapse after calving events. Overall, Antarctic ice shelf area has increased by 5,305 km^2 from 2009-2019, with 18 ice shelves retreating and 16 ice shelves advancing (Andreasen et al., 2023). The greatest retreat has occurred on the Larsen C Ice Shelf, which lost 5,917 km^2 during the calving of the A68 iceberg in 2017; alternatively, the greatest advance has occurred on the Ronne Ice Shelf, which has gained 5,889 km^2 of ice between 2009-2019. Shelf loss is concentrated along the AP (6,693 km^2) and West Antarctica (5,563 km^2); these losses are counteracted by large gains in East Antarctica, and on the Ronne and Ross Ice Shelves (Andreasen et al., 2023). From 2009-2019, six ice shelves experienced major calving events where > 5% of their total area was removed: the Wilkins, Wordie, Larsen C, Mertz, and Nansen Ice Shelves, and Thwaites Glacier (Andreasen et al., 2023). Thwaites Glacier has experienced the largest relative area change, with a total of 53.7% of its original area lost via iceberg calving and glacier retreat. Additionally, the Larsen C, George VI, and Wordie ice shelves experienced the greatest reduction in area in the 50 years prior to 2009, aside from Larsen A, B, and Wilkins prior to their collapse (Cook & Vaughan, 2010). Rapid calving front retreat was observed for the Larsen A remnant, Swinburne Ice Shelf, and the Pine Island Glacier, which all experienced sustained and significant ice loss from 2009-2019 (Andreasen et al., 2023). However, the fast-flowing glaciers feeding these ice shelves provide moderate annual advance despite their retreat (Andreasen et al., 2023). In contrast, ice shelves that have advanced from 2009-2019 include the Ninnis, Brunt, and Crosson Ice Shelves (Andreasen et

al., 2023). Larsen B continued to advance until the 1990s when it rapidly retreated just prior to its collapse in 2005; recently, tributary ice flow into the Larsen B embayment has caused rapid calving front advance (Cook & Vaughan, 2010; Andreasen et al., 2023).

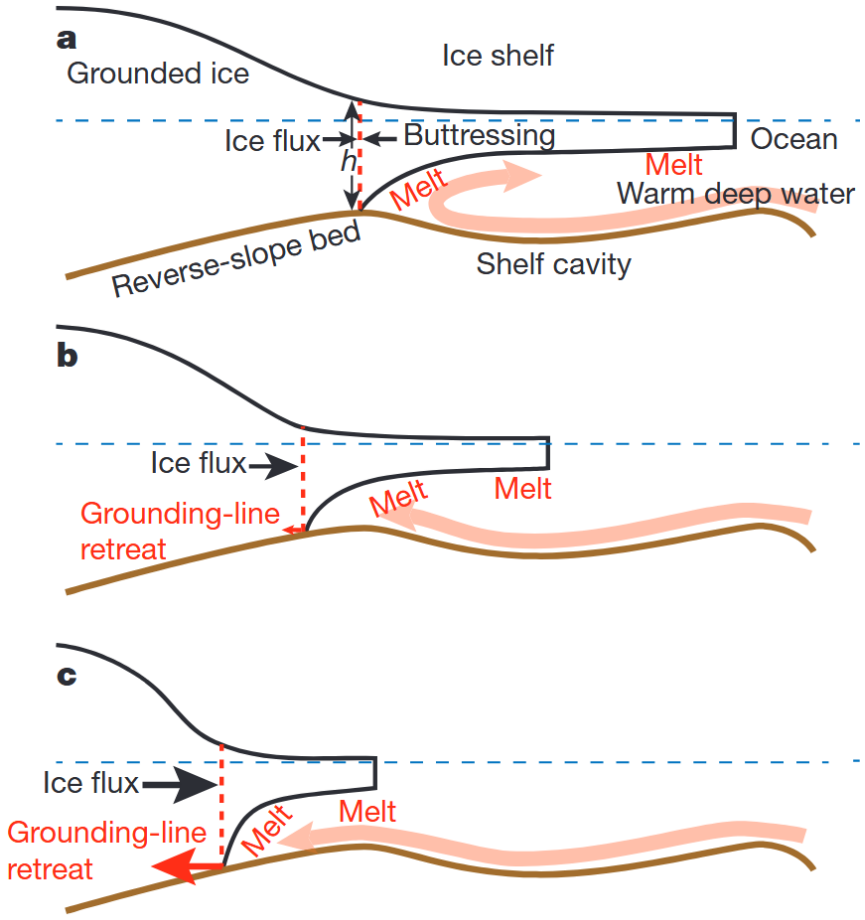

Figure 5. *Processes contributing to the marine ice sheet instability. The pink arrow represents the incursion of warm Circumpolar Deep Water into the ice shelf cavity.* ***(a)*** *Stable, marine-terminating ice sheet margin with a buttressing ice shelf. Seaward ice flux is dependent on grounding line thickness h.* ***(b)*** *Thinning ice shelves and reduced buttressing increase seaward ice flux, and grounding line retreats onto a reverse-slope bed.* ***(c)*** *Increasing h with grounding line retreat leads to an increase in ice flow across the grounding line until the bed reaches a new downward-sloping position and temporarily stabilizes (Credit: DeConto & Pollard, 2016).*

Dynamic mass loss from Antarctic ice shelves has historically been attributed to iceberg calving, while basal melting is considered a minor contributor, responsible for just 10-28% of total mass loss. The more recent understanding is that they contribute almost equally to ablation, with an average calving-to-melting ratio of 0.45 ± 0.3 (Rignot et al., 2013). However, basal melt rates vary considerably with thermal forcing, as a function of local ocean temperature and ice thickness (Pritchard et al., 2012). Area-average melt rates across Antarctica range from negative to more

than 40 m yr-1, with the strongest melt rates found near the grounding zones of major glaciers and along the fronts of ice shelves (Rignot et al., 2013). Basal melt is responsible for most of the mass loss occurring across West Antarctica and the AP (Rignot et al., 2013). Basal melt of floating ice in Antarctica is driven mainly by the incursion of relatively warm water into the ice shelf cavity, which occurs primarily through upwelling of Circumpolar Deep Water along the coast (Baumhoer, 2020). The introduction of warm ocean water to the ice shelf bed enhances basal melt, causing the grounding line to retreat inland (Depoorter et al., 2013). Retreat of the grounding line along a reverse slope (on which many Antarctic Ice Sheet grounding zones are located) can trigger a feedback mechanism known as the marine ice sheet instability (Figure 5; DeConto & Pollard, 2016). When the grounding line is positioned along a reverse-slope bed, grounded ice thickness increases if the grounding zone retreats, which accelerates ice flow and causes thinning. This continues until a new, downward-sloping position (a.k.a., "pinning point") is reached and the system temporarily stabilizes (Hanna et al., 2013). Through this mechanism, the stability of the ice sheet is vulnerable to the impacts of ocean warming, particularly along ice shelves which lie below sea level (DeConto & Pollard, 2016).

Thinning of ice shelves can also occur through warming-induced surface melt and iceberg calving. Meltwater accumulates in surface ponds or lakes formed through a reduction in firn air content, which encourages ponding when no further percolation is possible (Holland et al., 2011; Luckman et al., 2014). Melt ponds introduce flexural stresses on the ice surface, which can initiate the development of fractures and crevasses (Banwell et al., 2013). Any ice crevasse in the vicinity of a melt pond will fill with water; this creates an outward pressure at the crevasse tip which results in further cracking in a process known as hydrofracture (Scambos et al., 2000; Larour et al., 2021). Typically, any crevasse that is filled at least 90% with water will result in the crevasse propagating through the entire ice thickness. Therefore, ice shelves that show frequent surface melt ponding near the shelf front are likely to retreat via hydrofracture (Scambos et al., 2000). The loss of ice at the shelf front can reduce internal backstress forces in the ice sheet, thereby decreasing its resistance to flow and causing dynamic thinning (Wearing et al., 2015; DeConto & Pollard, 2016). Dynamic thinning, together with surface and basal melt, reduces the material strength of floating ice as it flows seaward (Massom et al., 2018). When the strain rate gets too high, iceberg calving occurs at the ice shelf front, originating from front-parallel rifts at the outer margins of ice shelves (Larour et al., 2021). Changes in ice fronts are linked to atmospheric and oceanic forcings, and

internal ice-sheet dynamics, though most ice shelves display multi-decadal cycles of growth and retreat (Benn & Astrom, 2018). The acceleration in flow velocity, dynamic thinning, and structural weakening due to melt ponds and hydrofracture leads to ice shelf instability, increasing the likelihood of disintegration events, particularly along the AP (Scambos et al., 2000; MacAyeal et al., 2003; Massom et al., 2018).

2.2.2 Drivers of Antarctic surface melt

The distribution of surface melt in Antarctica is driven by regional shifts in climate and the influence of local- and micro-scale processes. The upper limit of Antarctic surface melt is ~1,400 m above sea level during weak, but spatially extensive, melt episodes in West Antarctica (Nicolas et al., 2017; Bell et al., 2018). The most intense melt is observed over ice shelves, particularly along the AP (e.g., Larsen C, Wilkins, George VI), as well as the low latitude East Antarctic ice shelves (e.g., West and Shackleton; Bell et al., 2018). Highly localized, intense melt occurs on several other East Antarctic ice shelves which display extensive surface hydrological networks (e.g., Amery, Roi Baudouin; Lenaerts et al., 2017; Bell et al., 2018). Melt intensification across the northeastern AP is associated with the strengthening of circumpolar westerlies, which is related to a positive phase shift in the Southern Annular Mode since the 1970s (Bell et al., 2018). Regional and synoptic scale climate dynamics also influence surface melt distribution, including ocean-atmospheric variability in the tropical Pacific (Tedesco & Monaghan, 2006). Several widespread, anomalous melt events across the West Antarctic Ice Sheet and the Ross Ice Shelf provide evidence of this effect, suggesting a link to the El-Niño teleconnection which brings warm, marine air into West Antarctica (Nicolas et al., 2017). Local-scale processes such as the exposure of low albedo blue ice and bedrock near the grounding zone of ice shelves can enhance surface melt through the positive feedback between ice melt and albedo (Lenaerts et al., 2017). Additionally, local winds play an important role in surface meltwater production. Descending katabatic winds originating from the Antarctic interior are associated with downslope warming, wind scouring, and blue ice exposure, and are known to locally enhance surface melt along the grounding zones in areas such as Dronning Maud Land, and the Amery and Ross Ice Shelves. Similarly, foehn winds produce episodic melt events across the eastern AP ice shelves and in the McMurdo Dry Valleys (Bell et al., 2018). This process has been linked to the depletion of firn air content and the generation of meltwater ponds and hydrofracture, particularly on the Larsen C Ice Shelf (Luckman et al., 2014).

2.2.3 Iceberg calving from ice shelf rift systems

Approximately half of mass loss from the Antarctic Ice Sheet occurs through calving, driven by ice dynamic processes (Rignot et al., 2013; DeConto & Pollard, 2016). Throughout Antarctica, calving rates exhibit considerable variability as they are a function of complex, spatially dependent interactions between ice dynamics, atmospheric and oceanic temperatures, and adjacent sea ice cover (Shah et al., 2020). Calving of large (up to ~10^4 km^2 in area; Benn & Astrom, 2018) tabular icebergs from ice shelves is associated with the propagation of large rifts, which extend through the entire thickness of the ice (van der Veen, 2002). In the last decade, several large tabular icebergs have calved from ice shelves around Antarctica, including but not limited to A74 (~1,270 km^2; Francis et al., 2022) and A81 (~1,550 km^2; Morris et al., 2023) from the Brunt Ice Shelf, D28 (~1,650 km^2; Zhu et al., 2021) from the Amery Ice Shelf, and A68 (~6,000 km^2; Hogg & Gudmundsson, 2017) from the Larsen C Ice Shelf. Structural weaknesses (i.e., fractures, thinner ice) are introduced into the ice shelf from a combination of factors such as extensive surface flooding, hydrofracture, decreasing sea-ice coverage, and enhanced flexural strain and longitudinal extension from ice motion and ocean wave energy (DeConto & Pollard, 2016; Massom et al., 2018; Benn & Åström, 2018). These weaknesses control the rate of iceberg production such that initial calving events typically occur along front-parallel rifts at the outer margins of the ice shelf (Massom et al., 2018); precursor rifts that delineate the outline of future icebergs can sometimes be identified decades prior to calving (van der Veen, 2002). This process has been identified as a possible indicator of ice shelf collapse, as large calving events may result in a front position that is conducive to further retreat (Fürst et al, 2016; Massom et al., 2018).

Sea ice – particularly landfast ice – also plays an important role in protecting ice shelves from the impacts of ocean swells, particularly on thinner ice shelves (< ~200 m; Bassis & Walker, 2012). Sea ice-free conditions allow large swells to reach the shelf front, introducing flexural strain and triggering the propagation of rifts which eventually result in calving (Massom et al., 2018). Landfast ice can also bond together fragments from previous disintegration events, which maintains the mechanical strength of the ice shelf and reduces the rate of calving (Massom et al., 2018). The relationship between sea ice and calving is so pronounced that 94% of calving events on the eastern AP throughout the satellite era occurred during or shortly after the removal of sea ice (Christie et al., 2022). This suggests that abrupt changes in sea ice cover can initiate the final

weakening and calving of even the largest ice shelves, as seen in the disintegration of Larsen A in 1995 and Larsen B in 2002 (Massom et al., 2018).

2.4 Structure and development of ice shelf rifts

Rifts are large, full-thickness fractures that span up to several hundred meters deep and tens to hundreds of kilometers long; rift width varies from tens of meters wide at the rift tip to several kilometers at the widest part. On the Amery Ice Shelf, the Loose Tooth rift system spans 900 km^2; this system consists of multiple rifts which are ~10-20 km long and up to several km wide (Fricker et al., 2005; Bassis et al., 2008). On the Brunt Ice Shelf, the Chasm 1 rift was 22 km long and up to 2 km wide, and the Halloween Crack was ~50 km long and 1-2 km wide (De Rydt et al., 2018). On the Larsen C Ice Shelf, the LC2017 rift was ~200 km long and 0.2-2 km wide; other rifts around the Gipps Ice Rise range from 1-4 km wide.

First-order control on rift development is the internal glaciological stresses that create longitudinal and transverse stress gradients in the ice (MacAyeal & Rignot, 1998; Joughin & MacAyeal, 2005; Walker et al., 2013; Benn & Åström, 2018). Stress gradients in the ice are impacted by the orientation of existing fractures such that crevasses oriented perpendicular to rifts may hinder propagation, while crevasses oriented in the same direction may serve as conduits for sudden bursts of rift growth (Walker et al., 2013; Lipovsky, 2020; Larour et al., 2021). Rifts can either be formed by a bottom crevasse propagating upward, or a surface fracture propagating to the bottom (van der Veen, 2002); these fractures typically originate along the outer margins of ice shelves and extend seaward to the shelf front, eventually developing into the planes from which tabular icebergs calve (Hulbe et al., 2010). Rifts are likely to form where an ice rise is present or in the vicinity of coastal roughness such as sidewalls, islands, or local bedrock highs (i.e., pinning points; Figure 6). The margins between grounded, confined ice and unconfined “free-floating” ice are referred to as detachment zones (Miele et al., 2023); these regions delineate the spatial transition from buttressing ice to passive ice and represent a loss in lateral shear strength that resists the outward flow of the ice shelf (Fürst et al., 2016; Jeong et al., 2016; Lipovsky, 2020). As such, detachment zones are prone to high stresses and damage and are significant drivers of iceberg calving (Miele et al., 2023). Fractures can also originate from basal channels located beneath the ice shelf, which form due to concentrated buoyant plumes of ocean water and meltwater that carve

troughs upwards into ice shelf bases (Alley et al., 2019, 2022). These features cause localized thinning and mechanical weakening which can initiate the development of fractures and promote rifting (Alley et al., 2019). Additionally, fractures can form or be exacerbated by hydrofracture due to meltwater loading from heavy surface ponding (Scambos et al., 2009).

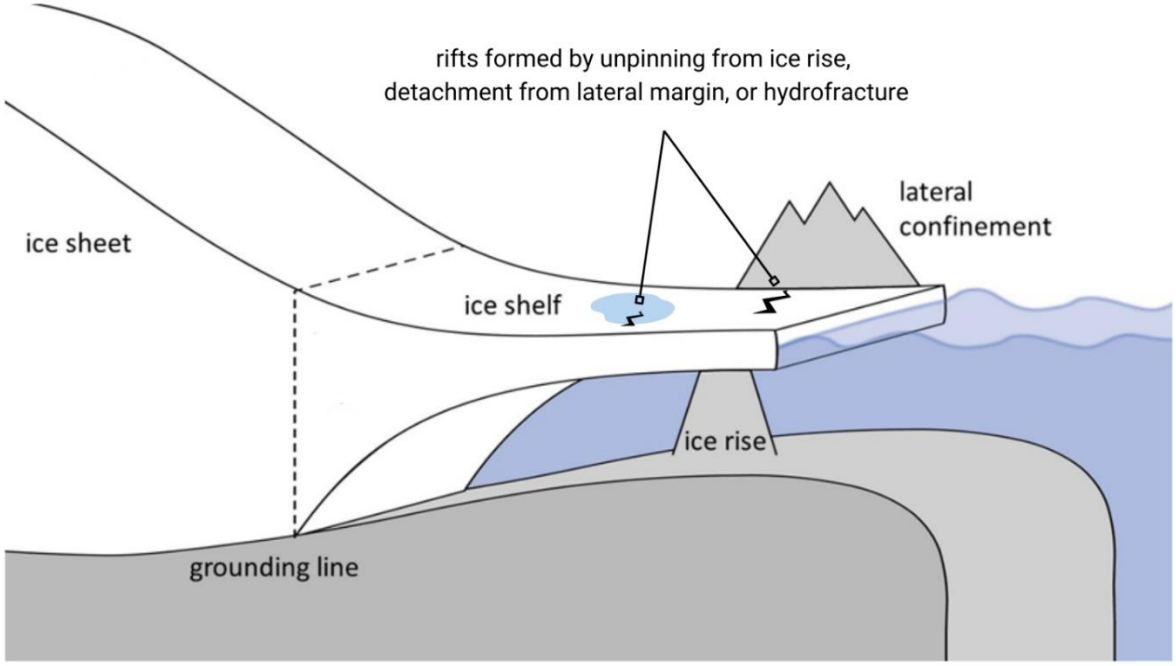

Figure 6. *Mechanisms of rift formation. Rifts form where the ice shelf unpins from an ice rise, detaches from the lateral margins or is freed from a confining bay, or through hydrofracture due to surface meltwater loading (Modified from R. Reese & M. Zeitz, retrieved from the Antarctic and Southern Ocean Coalition in January 2025).*

Many studies have reported little to no relationship between episodic rift propagation rates and environmental forcings such as ocean swell or sea ice concentration (Bassis et al., 2008; Walker et al., 2013; Walker et al., 2015). While environmental forcings do not appear to affect background rift propagation or calving rates, they have been suggested to play a role in triggering ice shelf disintegration events (Massom et al., 2018; Larour et al., 2021; Bassis et al., 2024). Extensive surface flooding and hydrofracture, sea-ice clearance and swell-induced flexure were found to precede the catastrophic disintegration of the Larsen A, Larsen B, and Wilkins ice shelves (Massom et al., 2018). Additionally, sustained exposure to atmospheric river events was a contributing factor in the collapse of Larsen A and B, and the calving of iceberg A68 from Larsen C (Wille et al., 2022); these events weaken ice shelf stability through their tendency to increase surface melt and reduce sea ice cover at the shelf front (Wille et al., 2022). These processes can initiate ice shelf collapse through a chain reaction of firn saturation, accumulation of melt ponds,

and subsequent hydrofracture (Scambos et al., 2000; Banwell et al., 2013; Luckman et al., 2014; Kuipers Munneke et al., 2014; Hubbard et al., 2016; Massom et al., 2018). These mechanisms suggest that environmental forcings may exert more influence on rift propagation as the rift approaches the ice front.

Episodic variability in rift propagation is instead suggested to be due to material heterogeneities in the ice shelf (Hulbe et al., 2010; McGrath et al., 2014; Jansen et al., 2013; Borstad et al., 2017). One such example is from the Nascent Rift on the Ross Ice Shelf, where no observable rift propagation occurred despite significant wave-induced stresses; this may suggest that the rift experienced cohesive strengthening due to the presence and refreezing of ice mélange, which resisted flexural strain by ocean swells (Lipovsky, 2018). Rapid rift propagation events have been observed to terminate when the rift tip reach a "suture zone" – a heterogeneous mixture of accreted marine ice, calved ice shelf blocks, and blown snow – which stabilizes the rift (MacAyeal & Rignot, 1998; Borstad et al., 2017; Lipovsky, 2018). These features evolve longitudinally in an ice shelf, forming downstream of peninsulas where flows from tributary glaciers meet and are bonded together by marine ice (Borstad et al., 2017). Ice of marine origin has a similar temperature to the sub-shelf ocean waters from which it originates, making it softer and more resistant to brittle fracture than meteoric ice originating from glaciers (Holland et al., 2009; Kulessa et al., 2014). By dissipating shear stress without fracturing, suture zones containing marine ice can slow the propagation of rifts and stabilize the ice shelf (Jansen et al., 2013; Borstad et al., 2017). Marine ice layers have been observed on the Amery, Ronne, and Larsen C ice shelves (Oerter et al., 1992; Craven et al., 2009; Hulbe et al., 2010; Jansen et al., 2013; McGrath et al., 2014). On Larsen C, marine ice concentrated in suture zones stalls the propagation of rifts by introducing heterogeneity into the ice shelf (Glasser et al., 2009; McGrath et al., 2014; Borstad et al., 2017), thus controlling iceberg formation and ice front position (Holland et al., 2009). The LCIS has six suture zones which originate from the Churchill Peninsula, Cole Peninsula, Maremelon Point, Francis Island, Tonkin Island, and Joerg Peninsula (Glassier et al., 2009; Borstad et al., 2017). These suture zones – particularly the Joerg Peninsula zone – play a significant role in stabilizing the ice shelf (Borstad et al., 2017). Without the Joerg Peninsula suture zone, rifts originating near Cape Agassiz would likely propagate across the ice shelf, well within the bounds of the critical "compressive arch," which acts as a limit for ice shelf viability (Doake et al., 1998; Borstad et al., 2017; Lipovsky, 2020). In 2017, following its sporadic advance since 2010, a large transverse rift calved a 5,800

km^2, 200 m thick iceberg from Larsen C; this was the largest calving event from Antarctica up to that point and presented a significant risk to the stability of the ice shelf. Factors which contributed to the propagation of the 2017 rift across the Joerg suture zone are therefore an important consideration for the stability of the LCIS, as this suture zone had previously stabilized dozens of fractures for decades (Borstad et al., 2017).

2.5 Remote sensing of ice sheets

2.5.1 Optical sensors

Satellite remote sensing of ice sheets can be broadly divided into techniques using optical or microwave frequencies, though less common approaches including gravity-based techniques exist. Optical satellites are passive sensors such that they either detect solar radiation reflected, or radiation absorbed and re-emitted, by the Earth's surface, typically within an electromagnetic range of 0.4 μm – 1 mm (Agrawal & Khairnar, 2019). Optical sensors can possess high spatial resolution with large swath widths, making them particularly useful for glacier mapping over extensive regions (Racoviteanu et al., 2008). In glaciology, observations made in the visual to near-infrared (NIR) spectrum are most valuable, as thermal imagery tends to have too coarse a resolution for the application to glacial remote sensing (Gao & Liu, 2016). The spectral reflectivity of ice features (e.g., glacier ice, fresh snow, firn) is governed by their surface albedo, which exhibits considerable spatial and spectral variability (Figure 7). Parameters such as grain size and shape, impurity content, near-surface liquid water content, and surface roughness impact the surface albedo of ice features and, subsequently, their reflectivity (Hall, 2012). Freshly fallen snow has very high reflectance in visible wavelengths (0.4-3 μm); as it ages, the reflectivity of snow decreases in the visible and NIR spectrums, largely due to melting and refreezing within surface layers, increasing grain sizes due to snow metamorphism, and the natural addition of impurities (Hall, 2012; Dietz et al., 2012). Reflectivity of snow, firn, glacier ice, and dirty ice vary greatly with wavelength (Hall, 2012). The reflectivity of glacier ice is quite low, but the presence of snow and firn increase reflectivity in the accumulation zone. Meltwater in lower zones and the presence of impurities tend to reduce the reflectivity, particularly at visible and NIR wavelengths (Hall, 2012). Ice feature identification with optical sensors can sometimes be challenging since different ice types often have similar spectral characteristics (Gao & Liu, 2016; Baumhoer et al., 2018). Ice

types must be spectrally separated to be accurately identified; a sensor with sufficient spectral resolution is therefore required to discriminate glacial features (Gao & Liu, 2016). However, high spectral resolution often comes at the cost of low spatial resolution, as decreasing the sensor's instantaneous field-of-view will result in less energy reaching the sensor. To reduce this effect and improve the signal-to-noise ratio, spectral resolution must be decreased. For this reason, mapping of glacial features with similar spectral characteristics at large spatial scales is not possible.

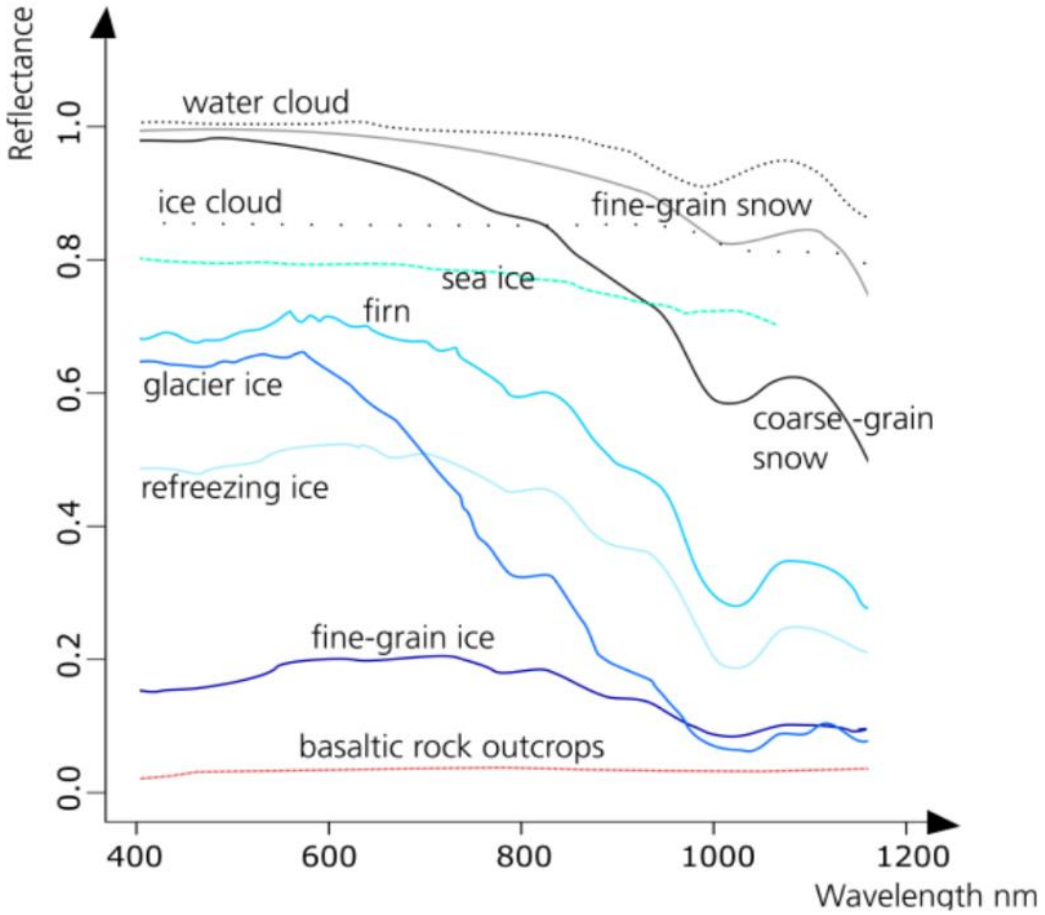

Figure 7. *Reflectance spectra of ice surface features and clouds in the visual and near-infrared spectrum (Credit: Baumhoer, 2020).*

Ice feature identification with optical sensors can also be challenging as the sensitivity of optical sensors to atmospheric water vapour also means they are unable to penetrate cloud cover. This presents one of the major disadvantages of optical sensors: their limitation to daylight and cloud-free conditions. Long-term monitoring of ice features with optical sensors is therefore difficult due to the limited availability of image acquisitions during the polar night and/or cloudy weather. Optical wavelengths are also sensitive to atmospheric attenuation and scattering by

atmospheric gases. Furthermore, the spectral signatures of atmospheric water vapour and ice clouds overlap with those of snow, particularly at shorter wavelengths (Dietz et al., 2012). This problem can be partially solved by correcting for atmospheric effects, which removes signals from atmospheric gases so that reflectance values correspond better with *in situ* surface reflectance (Gao & Liu, 2016).

2.5.2 Imaging radars

Active microwave sensors (i.e., radars, altimeters, and scatterometers) operate by transmitting a pulse of radiation towards the Earth's surface and measuring the proportion that is scattered back (i.e., backscattered) to the sensor. This value normalized over unit area is known as the backscatter coefficient (σ^0); the strength of σ^0 is used in conjunction with the radar equation 1 to determine the value of σ^0 for that part of the surface (Rees, 2012):

$$P_r = \left(\frac{P_t G_t}{4\pi R^2}\right) \sigma_{rt} \left(\frac{A_r}{4\pi R^2}\right) \qquad [1]$$

where P_r and P_t are received and transmitted power, respectively, G_t is the gain of the transmitting antenna, R is the distance between the target and antenna, σ_{rt} is the radar cross-section, and A_r is the effective receiving area of the receiving antenna aperture. Microwave radars typically use radiation that occupies the 1 mm – 1 m (or 300 – 0.3 GHz) region of the electromagnetic spectrum (Agrawal & Khairnar, 2019). Wavelengths greater than ~1 cm can penetrate through clouds and beneath the Earth surface, thus microwave sensors can collect imagery during all weather conditions and reveal buried features (Gao & Liu, 2016).

The spatial resolution of SAR imagery is two-dimensional and is determined by the length of the aperture (i.e., antenna length) and the distance between the target on the ground (Moreira et al., 2013). The resolutions – termed the azimuth resolution and the slant range resolution – refer to the orientation of the sensor relative to the flight path; the azimuth (i.e., along-track) direction is the sensor flight path and the range (i.e., across-track) direction is perpendicular to the flight path (Figure 8). Azimuth resolution is defined by the inverse relationship between the aperture and the radar beamwidth; a larger aperture will produce a narrower beam and thus a finer resolution. The azimuth resolution increases with altitude and features in this direction can only be distinguished if their size exceeds the track length, making targets more difficult to separate at

greater distances (Richards, 2009). In contrast, slant range resolution is independent of altitude but limited by the radar pulse duration; features must be farther apart than the pulse length to avoid overlapping echoes (Richards, 2009). During processing, SAR imagery must be converted from slant range to ground range, which involves correcting for compressional image distortions caused by slant range geometry. Since the ground range is the horizontal projection of the slant range onto the Earth's surface, the spatial resolution of a processed SAR pixel typically refers to the ground range resolution. The ground range resolution is derived from slant range but is a function of the incidence angle (θ), or the angle between the radar beam center and the local topography; the resolution will therefore vary across the swath width such that it is finer at steeper θ and coarser at shallower θ (Richards, 2009). While traditional radar systems are limited by the physical size of the antenna – since spatial resolution is inversely related to radar beamwidth – SAR overcomes this limitation by synthesizing a larger aperture through sequential, overlapping scans using a smaller antenna. This technique enables SAR sensors to make observations over large areas while maintaining high spatial resolution.

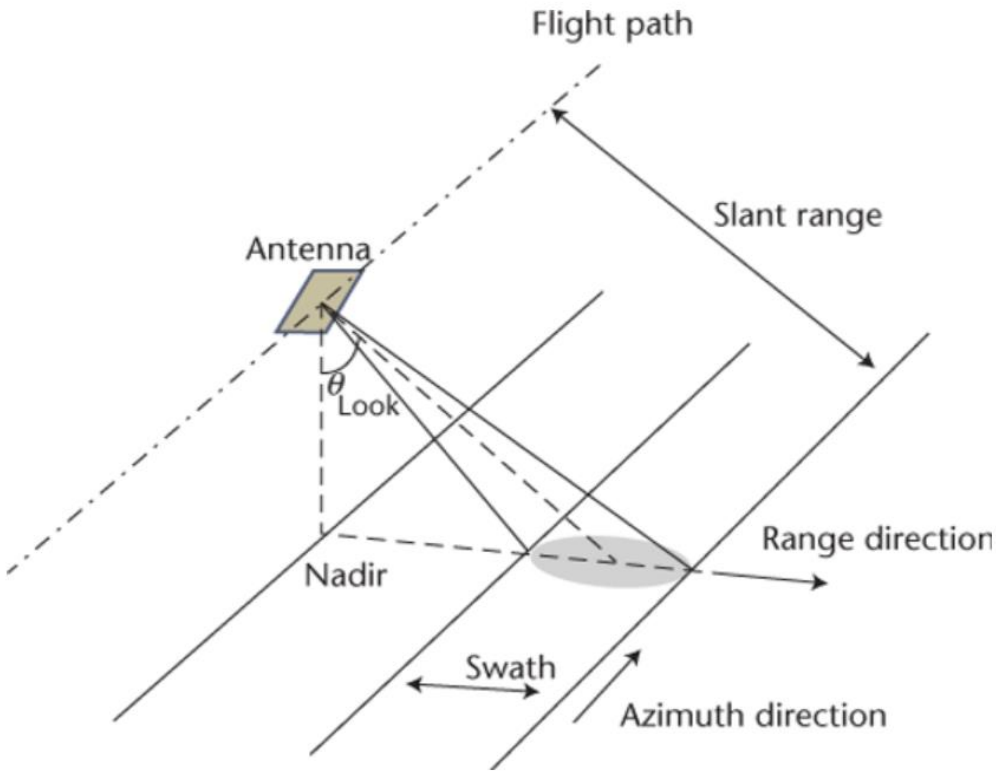

***Figure 8**. SAR imaging radar geometry (Credit: NASA, retrieved from Capella Space in January 2025).*

SAR images contain information on the phase and amplitude of backscattered radiation. Phase describes the position of the radar wave within its wavelength, while amplitude describes the strength (i.e., intensity) of the returned signal; phase is largely determined by the distance between the sensor and the target, while amplitude depends on various surface and sensor imaging properties. The brightness of SAR image pixels is determined by the intensity of the backscattered radiation. When radar signals interact with Earth surfaces, the degree and direction of scattering depends on the target's physical and electrical properties; as a result, σ^0 is highly sensitive to surface roughness and moisture content (Moreira et al., 2013). These characteristics influence the amount of radiation returned to the sensor, which controls the σ^0 intensity of an image pixel; smooth surfaces tend to scatter the radar signal away from the sensor in specular reflection, while rough surfaces scatter the signal diffusely in all directions and return more energy to the sensor. Smooth surfaces therefore do not typically produce strong σ^0 unless they are tilted in such a way that the signal is directed back toward the sensor, thus they appear dark in SAR imagery. Alternatively, rough surfaces typically produce strong σ^0 and appear bright in SAR imagery.

An important characteristic contributing to the appearance of SAR image features is the penetration depth (δ_p) of the radar signal into a medium. In the microwave region of the electromagnetic spectrum, δ_p is a function of the frequency of transmitted radiation and the moisture content of the surface. With decreasing frequency, the radiative attenuation in a volume increases, thus longer wavelengths such as L-band (1.2 GHz) have a greater δ_p and experience lower signal attenuation compared to shorter wavelengths such as C-band (5.4 GHz) (Figure 9; Moreira et al., 2013). As the liquid water content of the surface increases, δ_p decreases since microwaves are absorbed in water more than a few millimeters (Richards, 2009), and water presents a smoother surface that favours specular reflection and resists the penetration of microwaves. For the application of radar to ice sheet monitoring, the introduction of liquid moisture into the snowpack results in a large increase in the imaginary part of the dielectric constant (ε"). Even a modest increase of 0.5% liquid moisture content can raise ε" by more than one order of magnitude; this reduces δ_p and results in a dramatic decrease in σ^0 (Ulaby & Stiles, 1981; Ulaby et al., 1984). As a result, C-band δ_p is up to 10 m on cold, dry firn, ~5 m on damp snow, and 1-2 m on exposed ice; in contrast, L-band δ_p is typically much higher than C-band, penetrating up to 20 m on dry firn, ~10 m on damp snow, and up to 60-120 m on smooth, cold, exposed ice (Rignot et al., 2001).

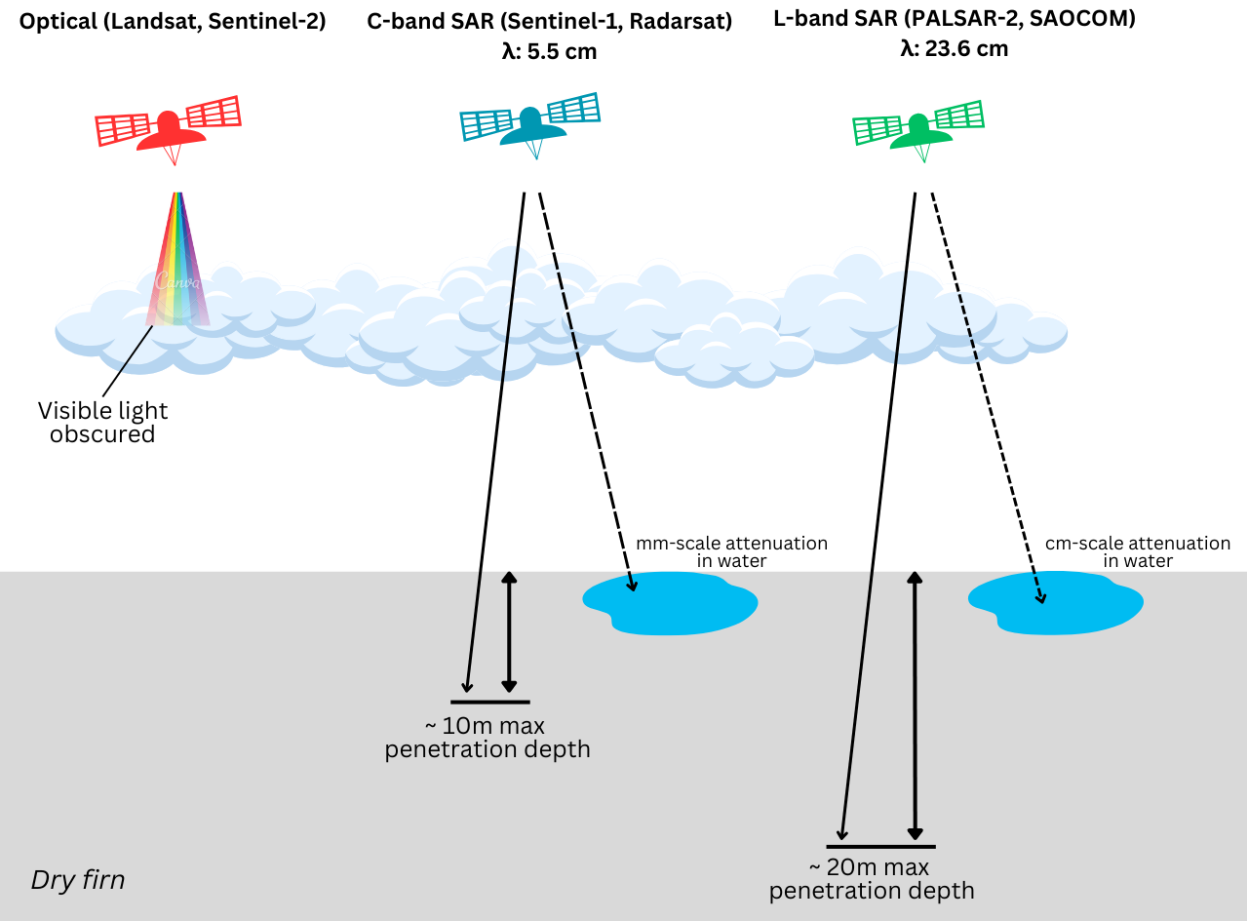

Figure 9. *Penetration depth of optical and C- and L-band SAR into glacial ice and melt water. Maximum penetration depth refers to the penetration potential in dry, cold firn. Values retrieved from Rignot et al., 2001.*

2.5.3 Non-imaging radars

The most commonly used non-imaging remote sensing radars include scatterometers and altimeters. The primary application of these instruments is in oceanography and cryospheric studies, particularly for spaceborne platforms. Altimeters are specialized non-imaging radars designed to measure surface topography and elevation. Altimeters transmit a laser or radar pulse toward the surface and measures the time delay from pulse transmission to receival; this time delay, combined with information about the precise orbit of the spacecraft (or aircraft), is used to calculate surface height with centimeter-scale precision (Ulaby & Long, 2014). For cryospheric applications, satellite altimeters can be used estimate sea ice freeboard and thickness, snow accumulation rates, and ice sheet elevation and mass balance, and map glacial features such as crevasses and supraglacial lakes (Zwally et al., 2008; Shu et al., 2018; Shepherd et al., 2019;

IMBIE, 2018; Morris et al., 2022; Xiao et al., 2023). Radar altimeters can penetrate through the snow cover to the snow-ice interface, while laser altimeters do not offer surface penetration; these two instruments can be flown together to measure the height of both the ice surface (radar) and the snow surface (laser), allowing for coincident retrieval of snow depth and ice thickness (Tedesco, 2015; Kacimi & Kwok, 2022). These estimates of both sea and land ice thickness are crucial for modelling glacier and ice sheet flow, and annual sea ice distributions.

Scatterometers are instruments designed to measure the reflectivity of targets by transmitting a microwave signal and observing the scattered and returned signal. The simplest scatterometers measure only the amplitude of the returned signal, while more sophisticated systems can extract additional information by analyzing the time delay and Doppler frequency shift of the received signal (Ulaby & Long, 2014). Although classified as non-imaging sensors, reconstruction-based processing techniques (Early & Long, 2001) have expanded their capabilities by enabling scatterometers to function as imaging sensors and produce low-resolution imagery. While scatterometers measure backscatter very precisely, they do not have aperture synthesis technology and therefore have much lower resolutions than SARs; regardless, scatterometer imagery remains highly useful in climate and polar research. Radar scatterometers enable accurate determination of wind speed and direction over the ocean, and their polar orbits enable them to provide broad-swath backscatter measurements over the entire polar region (Ulaby & Long, 2014). As a result, many polar locations are observed multiple times a day, making scatterometer data invaluable for cryospheric research such as sea ice mapping and surface melt detection. The sensitivity of active microwave frequencies to surface roughness means that first-year ice (FYI) and multi-year ice (MYI) can be easily differentiated due to their distinct o^0 signatures (Zhai et al., 2023; Zhang et al., 2022). These differences enable daily mapping of FYI and MYI using wind scatterometer data. Scatterometer data can also provide sub-daily observations of surface melt and sea ice extent due to the dramatic o^0 difference in between wet and dry surfaces (Ashcraft & Long, 2006; Arndt & Haas, 2019; Xu et al., 2023; Liu et al., 2023).

2.6 Synthetic aperture radar

2.6.1 Polarization

SAR backscatter is largely dependent on the polarization, i.e., the orientation of the electric field vector, typically horizontal or vertical (Richards, 2009). The polarization of the reflected wave provides insight into the characteristics of the surface as it is defined by scattering response of surface materials to different polarizations (Richards, 2009). SAR sensors that transmit and receive radiation that is either horizontally (H) or vertically polarized (V), are potentially capable of possessing one of four potential transmit and receive polarization combinations: HH, VV, HV, and VH. SAR sensors can possess several different polarization combinations and produce single, dual, or quad-polarization imagery (Table 1). Co-polarized signals (e.g., HH, VV) are transmitted and received in the same polarization; these signals are sensitive to roughness scattering or double-bounce scattering, as radiation is returned to the sensor in the same polarization upon interaction with the surface. HH polarization also helps to differentiate between rough and smooth surfaces, as smooth surfaces reflect a greater proportion of the signal away from the sensor in specular reflection. In contrast, cross-polarized signals (e.g., HV, VH) are transmitted in one polarization and received in another; these signals are sensitive to volume scattering from within the surface medium, which tends to depolarize the radar wave upon interaction with internal structures such as snow grains or vegetation (Casey et al., 2016).

Table 1. *Polarization channels for single-, dual-, and quad-polarization radar sensors.*

Polarization designation	**Channels used**
Single-polarization	HH or VV, HV or VH
Dual-polarization	HH and HV, VV and VH, or HH and VV
Quad-polarization	HH, VV, HV, and VH

2.6.2 Incidence angle

The incidence angle determines the appearance of a surface relative to the viewing geometry of the sensor and controls the occurrence and degree of topographic image distortions. The portion of the image swath closest to nadir represents the smallest θ (~20-30°) and is referred to as the near-range, while the portion of the swath farthest from nadir with the largest θ is called

the far range (40°+). The backscatter coefficient depends on θ variations throughout the image – this dependence can be shortened as $\sigma^0(\theta)$. While backscatter intensity is generally determined by the surface roughness and dielectric properties of the surface, the dependence on θ is primarily governed by the surface geometry and dominant scattering mechanisms inherent to that surface (Rees, 2012). In most cases, surface scattering is dominant so the dielectric constant, surface roughness characteristics, and imaging geometry all influence $\sigma^0(\theta)$. Backscatter from smooth surfaces decreases rapidly with increasing θ whereas, for rough surfaces, the reduction is relatively small (Rees, 2012). When volume scattering dominates, such as with dry snowpacks or vegetation canopies, the relationship between σ^0 and θ is more complicated and a weaker $\sigma^0(\theta)$ can be observed (Rees, 2012).

2.6.3 Radar image distortions

Because range resolution varies across the swath, the resolution in the *x* direction is typically different than in the *y* direction. Since imagery is typically displayed using uniformly sized pixels, larger regions on the ground at near-range are displayed with the same dimensions as smaller regions at far-range (Richards, 2009). Consequently, the ground at near-range appears compressed in comparison to the ground at far-range. Additionally, two features with different vertical reliefs appear differently in SAR imagery since the radar echo from the taller feature returns to the sensor faster than from the smaller feature (Richards, 2009). This causes taller features to appear as though they are laying over smaller features, thus this distortion is referred to as layover. Topographic relief also modifies the brightness of the image. Slopes facing the sensor will be foreshortened and appear brighter due to a smaller θ, while slopes facing away from the sensor will be lengthened and appear darker due to a larger θ (Richards, 2009). Shadowing is inevitable in radar images and is most severe in the far-range and for larger θ, and almost nonexistent for smaller θ. While distortions due to shadow cannot be corrected, distortions caused by compression, layover, and topographic relief can generally be corrected during pre-processing using a digital elevation model (DEM) and the local θ. The severity of these distortions is dependent on θ; for low relief areas, larger θ will emphasize topographic features and enhance image interpretability (Richards, 2009). Since space-borne radars possess mid-range θ (35-50°) for which there is generally little layover and shadowing, imagery from these sensors provides a good basis for surface roughness interpretation (Richards, 2009).

2.6.4 SAR pre-processing

Unlike optical sensors, visualizing raw SAR data typically does not give any useful information about the scene; it is only after signal processing that an image is obtained (Moreira et al., 2013). The aim of SAR pre-processing is to remove unwanted noise and distortions and enhance important image features. The standard pre-processing steps typically include radiometric calibration, geometric and radiometric correction, and speckle filtering; further processing can be performed depending on the specific SAR application. Radiometric calibration refers to the conversion of raw digital numbers to physical units of radar reflectivity. This step is essential to ensure pixel values appropriately represent surface reflectance; without calibration, SAR images from different sensors or acquisition modes or dates is not possible (Weiβ, 2018). Geometric correction (i.e., terrain correction) is performed to assign geometric coordinates to image pixels and remove topographic distortions such as foreshortening, layover, or shadow. This process requires information about the terrain (normally provided by a DEM) to remove topographic distortions (Weiβ, 2018). Geometric correction is often combined with radiometric correction (i.e., radiometric terrain flattening), which leverages the local θ and a DEM to remove variations in backscatter caused by variable topography. Lastly, speckle filtering is necessary to reduce noise associated with the speckle noise inherent to SAR imagery. Speckle arises from the constructive and destructive interference of radar signals reflected from multiple scatterers within a single resolution cell (Moreira et al., 2013, Weiβ, 2018). This degrades the quality of SAR images and results in information loss; therefore, speckle must be removed prior to image analysis. Speckle filtering impacts the spatial resolution of SAR images through filtering and averaging of pixel values; while some filters preserve the sharpness of edges within the image, fine details are often sacrificed. The effect of speckle tends to be reduced for very high-resolution systems, as the number of scatterers within an image cell is lower (Moreira et al., 2013).

2.6.5 Scattering mechanisms and backscatter characteristics of snow and ice

An ice sheet can be divided into different radar glacier zones that reflect the glacier facies based on variations in backscatter intensity. The dry snow zone, located in the highest regions of the ice sheet where no melt occurs, is characterized by deep radar signal penetration into the snowpack (Baumhoer, 2020). Fresh, dry snow is generally transparent at L- to X-band frequencies

(0.4 to 11 GHz) as the radar wavelengths are typically much larger than the size of fresh snow grains (Rott & Matzler, 1987); as a result, low volume scattering occurs, and this region displays intermediate backscatter in SAR imagery (Baumhoer, 2020). Variations in backscatter from this zone are largely attributable to variations in snow grain sizes (Rau et al., 2000). In contrast, the wet snow zone below is characterized by low snow accumulation rates and seasonal percolation of meltwater into the snowpack. High energy inputs into the snowpack enables wet snow metamorphism, which enhances snow crystal growth and snowpack densification. This layer is characterized by large snow grain sizes and rough, horizontal ice layers created by refreezing meltwater. The appearance of the wet snow zone in SAR imagery varies seasonally with temperature change. During winter when the snowpack is dry, volume scattering from internal layers dominates and the surface displays high backscatter; during summer, the accumulation of slush and melt ponds at the surface drastically reduces the backscatter coefficient. These differences make the boundary between wet and dry snow is very apparent in SAR imagery, particularly at higher frequencies. For mapping wet snow cover, X- and C-band frequencies are more effective than lower frequencies such as L-band; this is because only the uppermost layer of wet snow contributes to backscattering at high frequencies, while the microwave response for low frequencies is dominated by interactions with internal ice layers (Rott & Matzler, 1987; Fowler & Ng, 2021).

On exposed glacier ice, the radar return is dominated by surface scattering which is dependent on surface roughness relative to the wavelength (Rott & Matzler, 1987). Glacier ice surfaces are typically rougher than snow surfaces, therefore the radar return is dominated by scattering from the glacier surface over the volume (Rott & Matzler, 1987; Fowler & Ng, 2021). In contrast, the radar return from snow targets frequently includes contributions from the air-snow interface and the boundaries of internal snow layers (Rott & Matzler, 1987). Consequently, the backscatter return from snow is largely driven by the depth of the overlying snow layer and the frequency of the radar wave. A strong radar return can be observed for dry, deep snowpacks (i.e., greater than several meters) as contributions from volume scattering increase with snow depth. Conversely, a thin layer of dry snow on glacier ice will only slightly modify the return signal and the backscatter coefficient will be largely defined by the snow surface or by interactions with internal ice layers. At high frequencies such as X- and C-band, surface scattering contributions are greater, thus they are less sensitive to snow depth and the presence of snow covering the ice has a

relatively small impact in the backscattering coefficient. As frequency decreases, the sensitivity to snow depth increases and the return signal becomes dominated by interactions with underlying ice layers.

2.7 Current and future potential of satellites to monitor rifts

Satellite remote sensing provides the greatest utility for continuous monitoring of ice sheets and the study of calving related mechanisms; this is particularly appropriate for rapidly changing glacial systems as satellites provide continuous surveillance at large spatial scales. Developing accurate remote sensing-based techniques for rift detection will provide an opportunity to monitor rift growth at large spatial scales. Currently, remotely sensed monitoring of rifting and calving activity occurs either through periodic observations of specific ice shelves at high spatial resolutions (Larour et al., 2004; Fricker et al., 2005; Jeong et al., 2016; Banwell et al., 2017; Larour et al., 2021; Li & Wu, 2022; Pang et al., 2023), or more extensive observations made at lower spatial and temporal resolutions (Cook & Vaughan, 2010; Walker et al., 2013; Liu et al., 2015; Qi et al., 2021). Most calving studies occur along the AP, likely due to increased interest after the collapse of the Larsen A and B ice shelves, and the major calving event from Larsen C in 2017 (Baumhoer et al., 2018); a number of other studies also exist for the Brunt Ice Shelf (De Rydt et al., 2018; Marsh et al., 2021; Libert et al., 2022; Morris et al., 2023). Many ice shelves remain unstudied, thus introducing uncertainties in our estimates of ice shelf retreat.

The highly dynamic nature of ice shelves and rift features also requires regular monitoring, as changes in rift size are episodic and sometimes occur suddenly, leading to rapid weakening of the ice shelf. Rift features are often mapped in shorter time intervals to assess individual calving events, or to observe disintegration events; as a result, there are significant temporal gaps in rift detection studies as well. One of the greatest demands for satellite remote sensing of ice shelves is the need for longer, more frequent, and spatially complete measurements, and more freely available data (Bhardwaj et al., 2016; Baumhoer et al., 2018). Regular acquisitions by SAR (e.g., Sentinel-1) and optical (e.g., Sentinel-2, Landsat, MODIS) satellites present the potential for abundant data; to fully maximize the benefits of this, automated techniques should be developed to extract glacial features from these sources. Accurate, automated rift detection techniques do not yet exist, as these algorithms would need to consider how backscatter from rifts and surrounding

features varies across seasons and with different morphologies. Investigation into the optimal parameters for rift detection and classification would accelerate the development of such an algorithm, leading to the development of a standardized procedure that is comparable across disciplines.

2.7.1 Techniques for monitoring fractures

Since optical sensors are constrained by solar illumination and cloud cover, observations of rifts using optical data are mostly limited to the summer season (Walker et al., 2013; Jansen et al., 2015). Studies using optical data are often unable to detect true rift propagation rates or detect the precise location of the rift tip during times of significant cloud cover. At optical wavelengths, shadows severely limit the detection of fractures (Bhardwaj et al., 2016). Thermal imagery may provide an advantage here since crevasses tend to be cooler than the surrounding glacier surface; however, thermal imagery often has a very coarse spatial resolution which will limit the detection of smaller fractures. Thermal bands also help distinguish between surface types in the slush zone, where there are often many crevasses (Bhardwaj et al., 2016). Observations of subsurface rift propagation or any portion of the rift obscured by snow is not possible with optical data (Walker et al., 2013; Bhardwaj et al., 2016). Seasonal snow often covers smaller fractures, and parts of larger fractures, on ice sheets and alpine glaciers; crevasses obscured by snow cannot be detected at multispectral or thermal wavelengths, though their detection is possible at microwave frequencies such as with SAR (Bhardwaj et al., 2016). Despite its limitations, optical imagery is not affected by speckle noise or geometric distortions that make SAR imagery difficult to interpret (Shah et al., 2019).

SAR provides a significant advantage to fracture and rift detection studies by allowing year-round, all-weather imaging of polar regions. The appearance of fractures in SAR images is constrained by δ_p of the radar signal; thus, the success of SAR-based rift detection is constrained by imaging parameters which impact δ_p such as polarization, frequency, and incidence angle (Marsh et al., 2021; Zhao et al., 2022). The rough surfaces of rifts typically appear as bright, linear features in a SAR image, though the fracture depth plays a large role in the degree of scattering observed. Marsh et al. (2021) applied SAR to crevasse detection and found that, δ_p corresponds to the approximate thickness of snow bridges after which crevasses become visible to the sensor; δ_p

of several meters or higher is desirable to image shallow subsurface fractures. Rifts with a deep mélange layer may be obscured at shorter wavelengths or in the presence of surface melt due to reduced δ_p. Additionally, if a snow bridge exists but its thickness is less than the δ_p, there is a second air-snow interface at the base of the snow bridge which provides an additional scattering surface; the base of this layer provides a stronger return than the fracture sidewall, therefore enhancing the backscatter (Figure 10; Thompson et al., 2020; Marsh et al., 2021). Both bridged and unbridged fractures have a vertical surface at the side wall which provides an additional scattering surface; in the case of a bridged fracture, the side wall and base of the snow bridge may interact further through double-bounce scattering (Marsh et al., 2021). This can be extrapolated to ice shelf rifts which also provide a horizontal scattering surface due to a layer of ice mélange within the rift. Rifts without a mélange layer do not display this horizontal surface, thus large open fractures tend to appear as dark regions with low backscatter. Additionally, open fractures without a mélange layer promote interaction between the SAR signal and the ocean below, which also contributes to the observed low backscatter as the signal is attenuated by open water.

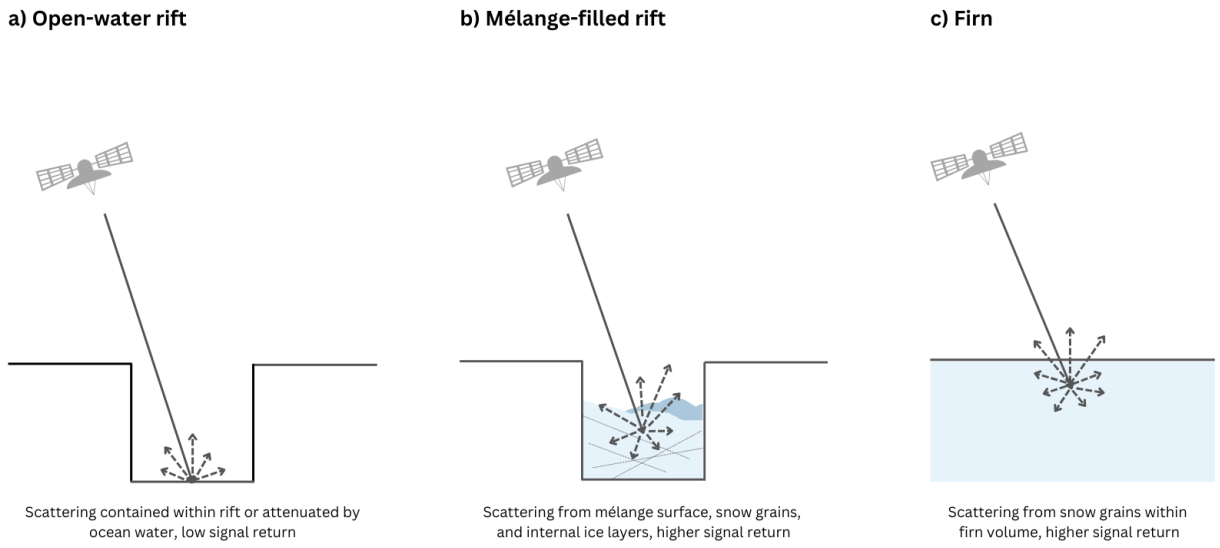

Figure 10. *Scattering mechanisms of different ice surface types with SAR.* ***(a)*** *Open-water rift: scattering occurs within the rift, signal is largely attenuated by ocean water and not returned to the sensor.* ***(b)*** *Mélange-filled rift: scattering occurs at the surface of the mélange layer, causing a higher signal return.* ***(c)*** *Firn: scattering occurs near the surface and within the firn/snow layer, also causing a higher signal return.*

Studies using SAR to study crevasses frequently report dependence on crevasse and imaging geometry (Brock, 2010; Thompson et al., 2020; Marsh et al., 2021; Zhao et al., 2022). Crevasses often present an efficient scattering surface, but the portion of returned energy is

dependent on the fracture geometry (Brock, 2010). The rough surface of glaciers and ice sheets often contains signals from terrain variations, snow ridges, and steep glacier slopes; these features increase the complexity of the surface and interfere with the detection of fractures (Zhao et al., 2022), especially with automated extraction techniques. The orientation of fractures relative to the sensor therefore impacts their visibility in a SAR image as it defines their separation from other features. Crevasses which are oriented perpendicular to the sensor look direction typically produce high backscatter contrast which helps discriminate them from the surrounding snow, while crevasses oriented parallel to the sensor display forward scattering and are more difficult to distinguish (Marsh et al., 2021). Resolution also impacts fracture detectability as SAR sensors can only discriminate fractures that are above the spatial resolution scale (Brock, 2010; Marsh et al., 2021).

Most studies using SAR for fracture detection have used either X- or C-band (Brock, 2010; Thompson et al., 2020; Marsh et al., 2021; Zhao et al., 2022). While frequencies such as X-band provide high spatial resolution which allows the discrimination of fractures as narrow as a few cm in width (Marsh et al., 2021), they are limited to a δ_p of < 3 m in dry snow. SAR Studies using X-band have been reasonably successful at detecting fractures with snow bridges up to 10 m thick (Thompson et al., 2020), with some studies even suggesting that X-band is the optimal wavelength to image fractures at a depth of 4 m (Brock, 2010). Higher frequencies are also more sensitive to surface roughness such that subsurface fractures will be more difficult to distinguish when the snow surface is significantly rough (Brock, 2010). Low frequencies such as L-band can penetrate up to 100 m (Rignot et al., 2001); while this may be excessive for imaging fractures near the surface, it may provide enhanced detection of subsurface rifts through reduced sensitivity to surface scattering. The success of detection greatly depends on the moisture content of the snow, with studies reporting that fracture detection with X-band may only be possible during cold, dry conditions which maximize δ_p (Thompson et al., 2020; Marsh et al., 2021). Snow moisture content appears to be the more important factor contributing to fracture visibility (Marsh et al., 2021), as liquid water in the snowpack will reduce δ_p and obscure the presence of fractures. L-band may present an advantage to fracture detection in this context as well due to lower signal attenuation and reduced sensitivity to moisture.

In contrast to SAR backscatter, interferometric SAR (InSAR) uses phase measurements to detect fine-scale displacements between coincident radar passes. InSAR techniques avoid the limitations associated with fracture and acquisition geometry, speckle noise, and reduced spatial resolution that are typically associated with SAR backscatter techniques. Propagating cracks and fractures typically correspond to phase discontinuities in an interferogram, which reflect areas of high surface deformation (De Rydt et al., 2018; Libert et al., 2022); this occurs as rifting activity deforms the ice by changing the stress field and altering ice flow patterns. This allows for identification of rifting activity before it is visible in SAR backscatter images. One advantage of this method is that it can detect fractures smaller than the sensor wavelength, therefore detecting extremely fine-scale changes in rift growth (Libert et al., 2022). However, phase artefacts may introduce noise and cause discontinuities which are easily mistaken for physical signals (De Rydt et al., 2018; Libert et al., 2022), and interferometric techniques rely on good coherence between an image pair in order to provide usable information. Changes in snow grains, snow drift and melt, or simply fast ice flow can cause temporal decorrelation, thus InSAR cannot be used for rift studies on fast-flowing glaciers or in highly dynamic regions of the ice sheet (Joughin et al., 2010; Libert et al., 2022). InSAR is also inappropriate for slowly propagating rifts with very small deformations, as interferograms do not pick up cracks that are not moving (De Rydt et al., 2018). These issues indicate that interferometric rift techniques may not be widely applicable, and results may not always be reliable.

Elevation data from airborne and spaceborne altimetry can also complement rift detection. Altimetry helps to identify abrupt changes in elevation which aids in indicating the presence of fractures and accurately delineating their boundaries. This adds crucial information to rift detection, especially to regions that are darkened by extensive surface melt and shadow. Several studies have used laser altimeters such as ICESat-2 to catalog rift features (Morris et al., 2023), characterize rift morphology and geometry (Wang et al., 2021; Li et al., 2021), and supplement optical segmentation of crevasses (Zheng et al., 2024). Airborne ground-penetrating radars (GPR) have also been applied to fracture detection as they can provide reliable imaging of subsurface features over large regions of an ice sheet. GPR can provide images of both surface and basal crevasses; both features have variable signatures associated with different snow and firn properties, and crevasse and acquisition geometry. (Thompson et al., 2020). Due to diffraction from crevasse walls, crevasses usually appear as stacked hyperbolae in GPR returns (Colgan et al., 2016). Similar

to SAR backscatter techniques, visibility of fractures with GPR is dependent on their orientation relative to the flight path; when crevasses are oriented roughly parallel to the flight path, their appearance is much more complex than the distinct hyperbola shape they typically assume, thus they are more difficult to identify (Thompson et al., 2020). Both altimetry and airborne GPR are limited by relatively spare observation density; GPR data is limited to the extent of the flight track, while laser altimetry is often collected in alternating X-shaped scans; therefore, there are often significant temporal and spatial gaps in data collection. Regardless, both techniques indicate good potential for improving the detection of fractures by providing insight into the vertical structure of fractures and validating satellite-based observations (Arcone et al., 2016; Wang et al., 2021). Supplementing satellite-based rift detection with high resolution elevation data can enhance the detection of rifts and provide information about rift geometry beyond what is possible with only satellite imagery.

A prominent limitation in fracture detection studies is the inadequate availability of free satellite imagery to the research community (Bhardwaj et al., 2016). GPR data is limited to what has been made publicly available from airborne field campaigns, and specialized microwave imagery such as X-band are not regularly acquired over the polar regions. Additionally, there is a demand for automating fracture detection to save time and effort. To address these gaps, developing fracture detection algorithms which leverage freely available, user-friendly data, is crucial. Algorithms developed using SAR backscatter techniques, particularly at widely available frequencies such as C- and L-band, are therefore a major benefit to many researchers. Along with the benefits of SAR to polar fracture detection, these frequencies – particularly C-band (Sentinel-1, Radarsat) – offer high temporal resolutions (< 1 day in the polar regions), and possess greater δ_p to detect buried fractures. Therefore, C- and L-band offer good potential to improve the detection of rifts, provide continuous monitoring of their growth, and satisfy the demand for a standardized method of rift detection.

2.7.2 Application of machine learning to rift detection

Automated fracture detection is desirable as visual interpretation introduces an element of subjectivity, and manual delineation is very time-consuming. Machine learning and deep learning techniques address these limitations by offering an opportunity to detect and classify features with

limited user interference. Machine learning (ML) seeks to automatically learn meaningful relationships and patterns from a set of training observations; deep learning is a ML concept which is based on artificial neural networks (Janiesch et al., 2021). ML algorithms are more complicated to apply compared to manual delineation, but they allow for efficient identification of features at large spatial scales. This structure is more computationally intensive and requires more input data than other ML algorithms, though they can automatically produce highly representative results since they are capable of learning from their own errors (Janiesch et al., 2021). For complex tasks with high-dimensional data, deep learning algorithms outperform ML algorithms; however, in cases of low-dimensional data input and limited training data availability, ML can produce superior results which tend to be more interpretable than those produced by neural networks (Janiesch et al., 2021). ML techniques are typically divided into supervised and unsupervised learning, with the latter arriving at a result without any previous labelling. Supervised learning algorithms such as support vector machine or random forest requires a training dataset which provides labelled observations (Janiesch et al., 2021).

Zhao et al. (2022) and Surawy-Stepney et al. (2023) used C-band SAR images to train a fully convolutional neural network (based on the U-Net architecture) to detect fractures in Antarctic ice shelves. This deep learning method has been modified so that it works with very few training images and yields more precise image segmentations (Ronneberger et al., 2015). These studies reported good visual consistency between automatically and manually detected fractures, showing high potential for the application of SAR and ML techniques to rift detection. Similarly, Lai et al. (2020) applied a neural network to optical MODIS imagery to map fractures at a continent-wide scale; the authors report good agreement between fracture locations identified with the neural network and a fracture mechanics model, despite morphological similarities between surface fractures, full-thickness rifts, and surface expressions of basal fractures. Other machine-learning based observations of fractures have used morphological filtering to detect fractures in SAR imagery (Moctezuma-Flores & Parmiggiani, 2016; Zhu et al., 2021). This approach works by applying a sequence of “opening” and “closing” processes to enhance or eliminate image structures; in the case of rifts, an opening following by a closing could indicate the presence of a fracture. Morphological filters and edge detectors help to enhance linear features while addressing limitations in SAR-based fracture classification due to speckle noise and high interclass and intraclass backscatter variability.

2.7.3 Rift classification techniques

In remote sensing, traditional image classification has been done using pixel-based approaches, where each pixel is classified solely based on its spectral information. Pixel-based classification is widely used because of its simplicity and ability to identify features based on spectral signatures. Spectral values are by far the most important factor in classifying features using pixel-based classification; therefore, classification proves difficult when classes have overlapping spectral signatures (Blaschke et al., 2014). Misclassification can also occur when an image pixel contains the average of several spectral classes, each reflected by a different type of material (Blaschke et al., 2014). Pixel-based approaches also struggle to classify features in imagery with high spatial resolution, as classified features will be significantly larger than the image pixels. This issue – termed the "H resolution problem" – occurs because a single object may be represented by multiple pixels with varying spectral values, increasing within-class spectral variability. As a result, the potential accuracy of pixel-based classification is reduced, as the variability within a single class can be substantial.

Object-based classification – or Object-Based Image Analysis (OBIA) – addresses some of these challenges by shifting focus from individual pixels to groups of pixels that form meaningful segments or objects within the image. Unlike pixel-based classification, OBIA integrates not only spectral information but also spatial properties such as shape, size, and relationships between objects; this allows for better handling of complex classes that are defined by their topological relationships. As a result, OBIA can achieve better classification accuracy, particularly when dealing with classes that do not have unique spectral signatures but are distinguishable by their spatial characteristics. The goal of OBIA is to leverage the spatial context and geometry of features in the imagery, addressing the limitations of pixel-based approaches.

OBIA consists of two main phases: segmentation and feature extraction/classification (Blaschke et al., 2014; Hossain & Chen, 2019). The process of segmentation divides the image into spatially continuous, homogeneous regions that differ according to their color, texture, shape, and size. This process lays the foundation for subsequent classification, thus the accuracy of feature extraction and classification is heavily dependent on the quality of the initial segmentation. Segmentation allows the use of statistical, textural, and geometric values for entire segments, thus providing more information for classification. There are two main types of segmentation methods

used in OBIA: edge-based and region-based (Hossain & Chen, 2019). Edge-based methods focus on delineating the object boundaries and filling in the regions defined by those edges. Edged-based methods assume that pixel properties between edges change abruptly; edges are detected and transformed into closed boundaries based on the presence or absence of a change in intensity values (Hossain & Chen, 2019). Alternatively, region-based methods identify homogeneous regions and expand outward until they reach the boundaries of an object. The basic approach to this is to obtain an initial segmented image and then merge or split segments that satisfy the criteria for homogeneity, then repeat this until the final segmentation is complete (Hossain & Chen, 2019).

3 Study area and data

The Antarctic Peninsula (AP) is characterized by many small outlet glaciers and ice shelves (i.e., Wilkins, George VII, and Larsen A-D ice shelves) which contain a collective 127,375 km^2 of ice (Rignot et al., 2013). This region is considered one of the most dynamic and climatologically variable regions in Antarctica; its climate is controlled by the Trans-Antarctic Mountains which act as a barrier to the Southern Hemisphere westerlies. As a result, the western side of the AP is generally colder and experiences the highest precipitation rates in Antarctica (Morris & Vaughan, 2003; Turner et al. 2019), while the eastern side frequently experiences strong warming from foehn winds on the leeward side of the mountains (Turton et al., 2018). Given its low latitude and complex regional climate, the AP is particularly sensitive to climate warming. Since 1950, the AP has shown a 2.5°C increase in mean annual air temperature and a total ice shelf area loss of 28,000 km^2 (Cook & Vaughan, 2010; Scambos et al., 2017). Mass loss occurs mainly through ice dynamic processes, with ~185 Gt of ice discharging into the Bellingshausen and Weddell Seas per year (Rignot et al., 2013). In the west, mass loss is dominated by basal melt through coastal upwelling of Circumpolar Deep Water, while iceberg calving dominates mass loss in the east (Rignot et al., 2013; Rignot et al., 2019).

At 46,465 km^2, the Larsen C Ice Shelf (LCIS) is the largest ice shelf on the AP; it drains a land area of 18,120 km^2 and has an ice volume equivalent to a global sea-level rise of 0.9 cm (Rignot et al., 2019). Ice thickness throughout the shelf varies from ~1,000 m near the grounding line to ~200 m near the ice front (Wang et al., 2022). The LCIS is confined by the Jason Peninsula

in the north and the Kenyon Peninsula in the south (Figure 11). There are two pinning points – the Bawden Ice Rise and the Gipps Ice Rise – which anchor the northern and southern ice fronts, respectively. The LCIS is the 3rd largest source of icebergs in Antarctica, calving more than ~80 Gt yr^{-1}, and is expected to be one of the next ice shelves to collapse (Qi et al., 2021; Larour et al., 2021). For this study, fractures within the Gipps Ice Rise (GIR) rift system, a ~16,500 km^2 region west of Cape Agassiz, were examined. In 2017, the A68 iceberg calved from GIR, reducing the size of the LCIS by 12%; this was the largest recorded calving event on the AP (Shah et al., 2020). This region therefore presents an active and geographically relevant case study when looking to understand the mechanisms behind rift propagation.

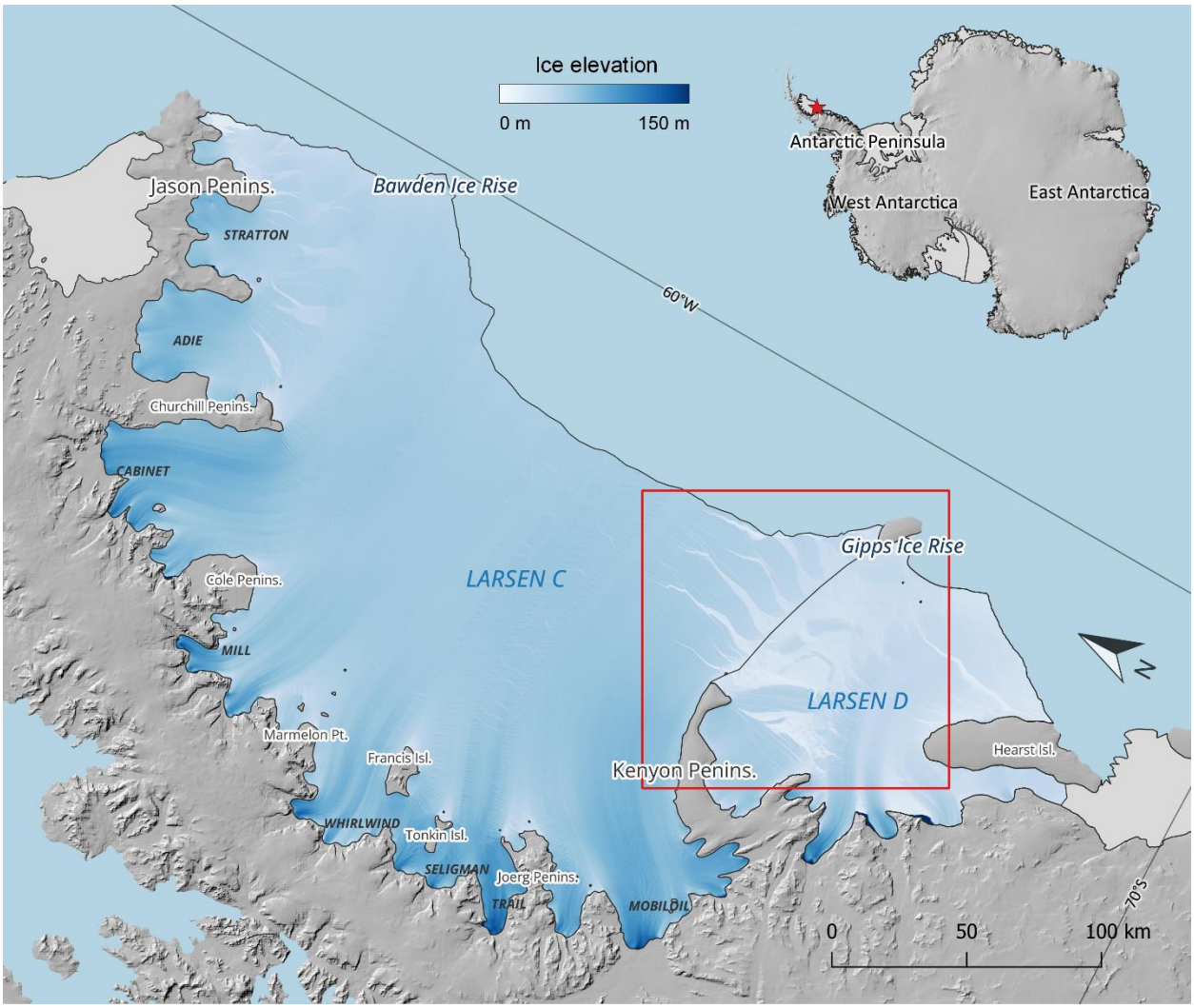

Figure 11. *Study area map of the Larsen Ice Shelf with Gipps Ice Rise rift system shown in red. Ice surface elevation retrieved from the TanDEM-X PolarDEM 90 m data product.*

3.1 Satellite data and pre-processing

Table 2. *Summary of primary SAR datasets and scenes used in this study.*

Sensor	Frequency	Polarization	Date	Mode	Pass	Pixel size	Objective(s)
Sentinel-1	C-band	HH+HV	19-09-2020 26-10-2020 30-11-2020 10-02-2021 12-03-2021	GRD EW GRD EW GRD EW GRD EW GRD EW	Descending Descending Descending Descending Descending	40 m 40 m 40 m 40 m 40 m	2 & 3 2 2 2 & 3 2
PALSAR-2	L-band	HH+HV	25-09-2020 12-02-2021	ScanSAR ScanSAR	Ascending Ascending	40 m 40 m	2 & 3 2 & 3
SAOCOM	L-band	HH+HV	25-10-2020 02-12-2020 19-03-2021	TOPSAR N TOPSAR W TOPSAR W	Descending Descending Ascending	40 m 50 m 50 m	2 2 2

3.1.1 Sentinel-1

The Copernicus Sentinel-1 mission is a two-satellite constellation currently consisting of Sentinel-1A and Sentinel-1C, with Sentinel-1A launched in 2014 and Sentinel-1C in late 2024 by the European Space Agency (ESA). These are identical satellites which occupy a sun-synchronous polar orbit and operate in C-band (5.4 GHz) frequency with a 6-day revisit time. In 2021, the failure of the Sentinel-1B satellite reduced the temporal resolution to 12 days and significantly limited data availability over the Antarctic coastline. Sentinel-1 provides single- and dual-polarization imagery in Single Look Complex (SLC) and Ground Range Detected (GRD) format, where SLC contains the phase and raw amplitude data, and GRD contains amplitude data and has been multi-looked and projected to ground range. This study used dual-polarization HH+HV GRD products in the EW (extra wide swath) and IW (interferometric wide swath) beam modes with 40 m and 20 m pixel resolutions, respectively. All Sentinel-1 data were accessed through the Alaska Satellite Facility.

Towards objective #1, 62 HH-polarization images in IW mode from 16 August 2015 to 12 July 2017 were used to manually track the development of the rift that calved the A68 iceberg from Larsen C in July 2017 (termed here LC2017). These images were radiometrically calibrated, speckle filtered with an edge-preserving median filter with a 5 × 5 window size, terrain corrected using the ALOS 3D 30 m (AW3D30) DEM and Antarctic Polar Stereographic projection (EPSG:3031). With respect to objective #2, five HH+HV Sentinel-1 scenes were analyzed (Table

2). To apply them to the separability analysis, these scenes were radiometrically calibrated to backscatter values in sigma-naught (σ^0), terrain flattened and corrected using the AW3D30 DEM and EPSG:3031 projection, and speckle filtered using a 5 × 5 median filter. Terrain flattening is and correction were performed to remove the influence of topographic distortions on backscatter and convert slant-range geometry into a map coordinate system (see Section 2.6.4); terrain flattening uses the local θ and a DEM and involves the process of converting backscatter values from σ^0 to gamma-nought (γ^0). The objective #2 steps differ from the processing applied during objective #1 as they were chosen to match the processing performed on PALSAR-2 Level 2.2 products (see Section 3.1.2). Lastly, for objective #3, the scenes from 19 September 2020 and 10 February 2021 were used to represent deep freeze and deep melt conditions; the same processing was applied for these scenes as with the objective #2 scenes, but the filter window size was increased to 7 × 7 to improve speckle reduction during classification. Processing was completed in ESA's Sentinel Applications Platform (SNAP) software and final γ^0 backscatter values, representing the radar cross section after consideration of the local θ through the DEM, are reported in decibel (dB) units following conversion using equation 2:

$$dB = 10 \times log\ 10(n) \qquad [2]$$

where n is γ^0 in linear units.

3.1.2 ALOS PALSAR-2

PALSAR-2 (Phased-Array L-band Synthetic Aperture Radar) is an L-band (1.27 GHz) frequency SAR instrument on the ALOS-2 (Advanced Land-Observing Satellite-2) satellite, operated by the Japan Aerospace Exploration Agency (JAXA). ALOS-2 is a sun-synchronous, polar-orbiting satellite that was launched in 2014 and can provide global coverage every ~2 weeks, depending on operation mode. PALSAR-2 imagery is provided in single-, dual-, quad-, and compact polarization at several imaging modes (Spotlight, Stripmap, and ScanSAR), though only ScanSAR imagery is publicly available. For this study, ScanSAR Normal imagery with Level 2.2 processing was used; these data come processed in a format that conforms with the Committee on Earth Observation Satellites (CEOS) Analysis Ready Data for Land (CARD4L) Normalized Radar Backscatter (NRB) product guidelines (CEOS, 2021). Images are orthorectified and terrain corrected using the AW3D30 DEM and provided in γ^0 by JAXA to minimize the effect of

observation geometry on radar backscatter values. The availability of publicly available PALSAR-2 data is limited, as typically only two coincident images are available over the LCIS per year. Two PALSAR-2 scenes from 25 September 2020 and 10 February 2021 were used in objectives #2 and #3 for separability analysis and rift classification, respectively. These scenes were speckle filtered with a median filter and reprojected to EPSG:3031 in SNAP; the scenes used in objective #2 used a filter with a window size of 5 × 5, while the objective #3 scenes used a window size of 7 × 7. Pixel resolution was downsampled from 25 to 40 m to match the resolution of Sentinel-1 EW imagery. Backscatter values were converted to linear units from raw digital numbers using equation 3:

$$Linear\ units\ = \frac{n^2}{10^{8.3}} \qquad [3]$$

where *n* is backscatter in digital numbers. Final values are reported in decibels after conversion using equation 1. An additional seven scenes from 22 August 2014, 8 June 2015, 17 June 2015, 21 August 2015, 19 August 2016, 23 December 2016, and 6 January 2017 were used for objective #1 to track the development of the LC2017 rift; these scenes were speckle filtered with a median 5 × 5 filter and projected to EPSG:3031.

3.1.3 SAOCOM

Due to limitations in data availability over the LCIS with PALSAR-2, SAOCOM (Satelité Argentino de Observación COn Microondas) L-band (1.25 GHz) SAR imagery was also acquired to satisfy objective #2. The SAOCOM-1 constellation consists of two sun-synchronous satellites, SAOCOM-1A and SAOCOM-1B, launched in 2018 and 2020, respectively, by the Argentinian space agency CONAE (Comisión Nacional de Actividades Espaciales). These satellites provide single-, dual-, quad-, and compact polarization imagery with an 8-day revisit time. SAOCOM has two operational modes, StripMap and TOPSAR; TOPSAR Narrow (TNA) has a spatial resolution of 25 m, and TOPSAR Wide (TW) has a resolution of 50 m. Three scenes were acquired during the 2020-2021 melt year (see Table 2). The December 2020 and March 2021 scenes were in TOPSAR Wide mode, while the October 2020 scene was in TOPSAR Narrow; this scene was resampled to 40 m to match the resolution of PALSAR-2. All SAOCOM scenes were delivered in Level 1C Geometric Ellipsoid Corrected (GEC) format, which have been radiometrically

calibrated, geocoded, and ellipsoid corrected using the WGS84 (World Geodetic System 1984) ellipsoid; ideally, for comparison to PALSAR-2 L-band, SAOCOM data would be acquired in Level 1A SLC format and pre-processed to match the CARD4L NRB guidelines, as with PALSAR-2 and Sentinel-1. Due to incompatibilities between SNAP and SAOCOM Level 1A data, Level 1C GEC data were required. As a result, PALSAR-2 has been terrain flattened and terrain corrected while SAOCOM has been ellipsoid corrected, which may present slightly different backscatter values for the two sensors; however, this effect is expected to be minimal as the relatively flat surface of the LCIS likely does not experience large terrain-related variations in backscatter. SAOCOM scenes were provided in σ^0 and converted to γ^0 using the ellipsoid θ and equation 4:

$$\gamma^0 = \frac{\sigma^0}{cos\theta} \quad [4]$$

where θ is the incidence angle in radians, and γ^0 and σ^0 are expressed in linear units. Using the ellipsoid θ instead of the local θ to convert to γ^0 can lead to inaccuracies in regions with significant topography, but this should again be reduced due to the flat surface of the LCIS. Finally, all scenes were speckle filtered and reprojected in SNAP following the same processing methods as for PALSAR-2 and Sentinel-1, and final backscatter values are reported in decibels following conversion using equation 5:

$$dB = 20 \times log\ 10(n) \quad [5]$$

where n is γ^0 in linear units.

3.1.4 ICESat-2

Towards objectives #2 and #3, the ATL06 Land Ice Along-Track Height product from the Advanced Topographic Laser Altimetry system (ATLAS) instrument on board ICESat-2 (Ice, Cloud, and Land Elevation Satellite-2) was used to verify fracture location, characterize rift geometry and develop ice surface classes (Section 4.3), and assess the performance of classification methods (Section 5.2.2). ICESat-2 was launched in 2018 as the second generation of the laser altimetry ICESat mission, owned and operated by the National Aeronautics and Space Administration (NASA). The ATLAS instrument is a photon-counting laser altimeter, which records the transit time of individual photons to reconstruct along-track surface height. ATLAS

collects elevation data using six green (523 nm) laser beams, arranged into a 2 × 3 array. Beams are arranged into strong and weak patterns relative to each other which changes depending on the orientation of the instrument; when ATLAS is oriented backward (forward) the strong beams are on the left (right) side of the beam pairs (Smith et al., 2019). The ATL03 Geolocated Photon Heights product was used as the foundation of the ATL06 product, which provides measurements of land ice height at ~40 m spatial resolution.

3.1.5 ASCAT

Towards objective #2, data from the Advanced Scatterometer (ASCAT) were used to discriminate surface melt and freeze conditions across the LCIS. ASCAT is a fan-beam scatterometer instrument on board ESA's polar-orbiting MetOp satellite. ASCAT operates at a C-band (5.3 GHz) frequency with VV polarization and provides radar backscatter measurements up to three times a day, at a 25 km spatial resolution. This study used the Enhanced Resolution Image product available through the Scatterometer Climate Record Pathfinder (SCP), where data has been normalized to a 40° θ and enhanced to a 4.45 km resolution using the Scatterometer Image Reconstruction (SIR) algorithm produced by the Brigham Young University Center for Remote Sensing (Early & Long, 2001). This algorithm combines multiple passes of the spacecraft to produce a higher spatial resolution, at the cost of a reduced temporal resolution. SIR products over Antarctica are created by combining imagery collected during morning and evening orbit passes to produce once-daily imagery. This study used daily ASCAT images from 5 May 2020 to 31 March 2021, to cover the full 2020-2021 melt year, from the end of the previous winter to the following freeze up. ASCAT SIR data are produced in the .sir file format, which stores imagery along with information required to earth-locate the image pixels. SIR files must be converted to a different format (e.g., netCDF or GeoTIFF) before analysis can take place; in this study SIR images were converted to netCDF format and merged into one file using a combination of C programs provided by SCP and in-house developed shell scripts. The resulting file was clipped to a shapefile of Larsen C to allow for accurate averaging (i.e., did not contain σ^0 values from the mountains or the ocean). Surface melt was identified using a fixed C-band threshold of -2.7 dB below the previous winter mean (Ashcraft & Long, 2006). The previous winter was defined as 1 June 2020 to 31 August 2020 and the mean was calculated over the entire ice shelf. ASCAT surface melt is

discussed in terms of absolute σ^0 deviation from the winter mean and a Boolean melt/freeze condition where melt is any pixel that is below a fixed backscatter threshold for that date.

3.1.6 Landsat

Landsat optical data were used to track the progression of rift growth on the LCIS for objective #1. This study primarily used Landsat 8 imagery, though Landsat 7 was also used to track the LC2017 rift prior to 2013. The Landsat program is a joint operation between NASA and the United States Geological Survey (USGS) that has involved nine satellites to date. Both Landsat 7 and 8 satellites have sun-synchronous, near-polar orbits with a 16-day revisit times. The Landsat 8 satellite was launched in 2013 and carries two instruments: the Operational Land Imager (OLI) and the Thermal Infrared Sensor (TRS). OLI collects imagery in nine spectral bands spanning the visible, near infrared, and shortwave infrared portions of the electromagnetic spectrum, plus a panchromatic band; these bands have a spatial resolution of 30 m (aside from the panchromatic band which has a 15 m resolution); alternately, TRS collects two bands of thermal infrared imagery at a 100 m spatial resolution. Landsat 7 was operational from 1999-2024 and carried the Enhanced Thematic Mapper Plus (ETM+) instrument, which collected imagery in eight bands at visible, near infrared, and shortwave infrared wavelengths, plus a thermal and a panchromatic band. These bands also have a spatial resolution of 30 m, except for the thermal (60 m) and panchromatic (15 m) bands.

To track the LC2017 rift, 75 Landsat 7 and Landsat 8 images were collected between February 2010 and July 2017. It is important to note that all Landsat 7 scenes used displayed an error due to the Scan Line Corrector failure and, at times, this error obscured the rift. Data were retrieved from both the Level 1 Systematic Terrain Correction (L1GT) and Level 2 Surface Reflectance (L2SR) products. L1GT data were radiometrically calibrated and geometrically corrected using the Radarsat Antarctic Mapping Project (RAMP) Version 2 DEM, and brightness values are reported in scaled digital numbers. L2SR data has been geometrically and atmospherically corrected to surface reflectance values and was processed to meet the CARD4L Surface Reflectance data requirements (CEOS, 2020). A L2SR Landsat 8 scene from 30 August 2020 was applied to objective #3 to test the performance of optical object-based classification and produce the objects during the final segmentation.

3.2 Ancillary datasets

3.2.1 REMA DEM

The Reference Elevation Model of Antarctica (REMA) DEM is a high-resolution (2 m) digital surface model of the entire Antarctic continent. The model is constructed from hundreds of thousands of stereoscopic DEMs extracted from pairs of submeter (0.23-0.5 m) resolution satellite imagery, including data from WorldView-1, WorldView-2, and GeoEye-1, acquired between 2009 and 2021 over the austral summer seasons (December to March). Each DEM has been vertically registered to satellite altimetry measurements from Cryosat-2 and ICESat, resulting in absolute uncertainties of < 1 m over most of its area. Output DEM raster files are available as "strip" files which are direct outputs, and "mosaic" files which are compiled from multiple strips and co-registered, blended, and feathered. Towards objective #2, REMA DEM was used alongside ICESat-2 ATL06 data to divide the ice shelf surface into ice classes, validate the presence of rifts and characterize their geometry. Mosaic tiles were used for most of the analysis, but more recently collected strips were used individually when exact rift locations or depths could not be verified with the mosaic dataset.

3.2.2 ERA5 Reanalysis

Hourly 2-meter air temperature data from 1 January 2020 to 31 December 2021 was retrieved from the fifth generation of the European Center for Medium-Range Weather Forecasts (ECMWF) atmospheric reanalysis (ERA5), with a grid resolution of 0.25° x 0.25°. ERA5 data were clipped to a bounding box of 65-71° S and 65-60° W, which covers the entire LCIS. Temperature was converted from Kelvin to Celsius, aggregated to a daily timescale, and a regional mean was calculated for each timestep. This dataset was used in conjunction with ASCAT σ^0 to determine ice seasons and contextualize ice surface conditions for objective #2.

4 Methodology

4.1 Visualizing the LC2017 rift and qualitative comparison of satellite sensors

For objective #1, to visualize and track the development of the LC2017 rift, and at the same time qualitatively assess the performance of each sensor type for this task, the following sensors were used: Landsat 7 and 8, Sentinel-1, and ALOS-2/PALSAR-2. The Landsat panchromatic band (B8) and Sentinel-1 IW imaging mode were used due to their higher spatial resolution and therefore enhanced ability to discriminate fractures at finer spatial scales. Occasionally, when the Landsat 8 panchromatic band was unavailable, the lower resolution near infrared (B5) or shortwave infrared bands (B11) were used instead. The rift was manually tracked from February 2010 to July 2017, at a temporal resolution that was subject to the availability of satellite imagery. Landsat 7 provided imagery until January 2014, after which Landsat 8 was used. Sentinel-1 and PALSAR-2 imagery were only available from mid- to late 2014, and only seven coincident PALSAR-2 scenes existed over the region for the entire study period. This case study presents an example of how various sensing types differ in their ability to detect and monitor ice shelf rifts.

4.2 Melt detection and melt season identification

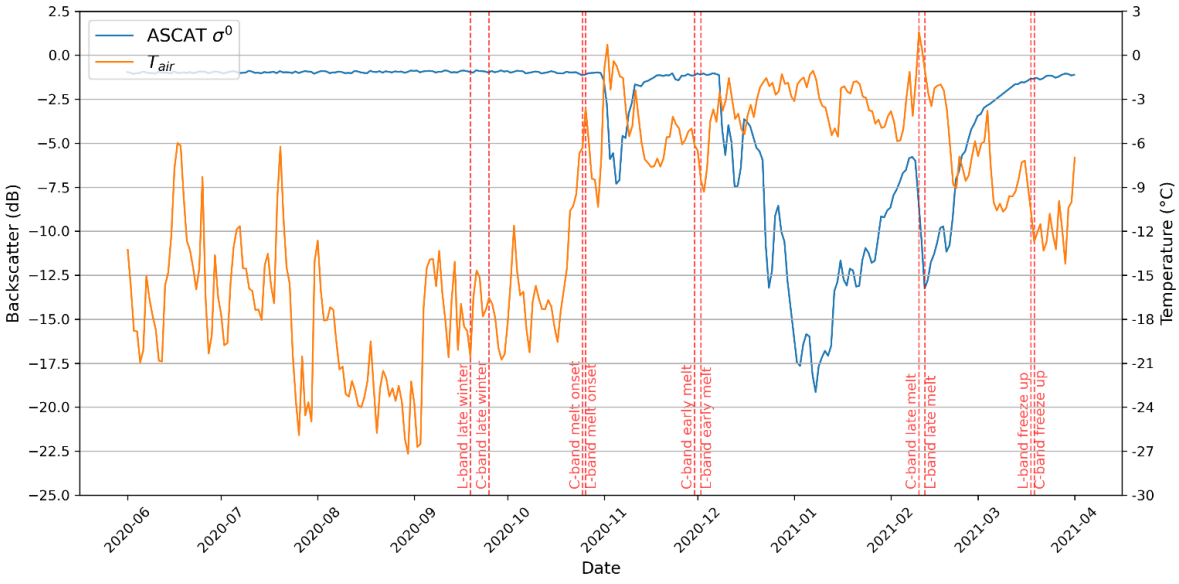

Figure 12. *Mean ASCAT σ^0 and ERA5 2-meter air temperature (T_{air}) over the Larsen C Ice Shelf from June 2020 to April 2021. Mean σ^0 was calculated over the entire LCIS for each timestep. Red lines indicate the dates of SAR scenes used for the five seasons (late winter, melt onset, early melt, late melt, and freeze up).*

For objective #2, surface melt was defined using a threshold of -2.7 dB below the previous winter mean, applied to ASCAT C-band σ^0 (Ashcraft & Long, 2006). This threshold was developed for C-band radar with a center frequency of 5.3 GHz and identifies wet snow conditions based on the difference in observed backscatter relative to dry snow conditions. To calculate the winter mean, the austral winter is defined here as 1 June to 31 August, with the austral melt year beginning on 1 August (Bevan et al., 2018). Time series of mean ERA5 air temperature and ASCAT σ^0 from 1 June 2020 to 1 April 2021 (Figure 12) were used to determine the ice seasons used in this study: late winter (LW), melt onset (MO), early melt (EM), late melt (LM), and freeze up (FU).

Late winter is defined as the period during the end of the austral winter, with very low air temperatures and high σ^0; this period reflects the conditions prior to the melt season, when the snowpack is dry and deep, and no melt is present (Figure A1). Melt onset is defined as the time when melt has been detected for more than three consecutive days (Tedesco et al., 2007; Barrand et al., 2013); however, due to the low availability of L-band imagery, SAR scenes representing MO were actually acquired 6-7 days before true MO (2 November 2020). This date reflects the period immediately before a short-lived melt event in early November; the use of this date to represent melt onset is justified here as changes to the ice surface can be observed (i.e., a reduction in ASCAT σ^0) over the GIR region, though the reduction in σ^0 has not yet reached -2.7 dB (Figure A2, A3). Additionally, these changes can be attributed to the introduction of liquid water as indicated by steadily increasing air temperature. While air temperature does not reach above 0°C until 2 November, liquid water may still exist below 0°C depending on other contributions to the energy balance (Barrand et al., 2013). Melt conditions are divided into two sub-seasons: EM and LM. EM occurs during a period of refreezing, < 1 week away from the initiation of full shelf-wide melt. This season was added to assess whether fluctuations in ice surface conditions during seasonal transitions cause significant changes in backscatter signatures and/or influence ice type separability. From 31 October 2020 to 1 April 2021, there are no more than two consecutive days without melt; these days are 5 and 6 December 2020, which is approximately 1 week after the early melt scenes were collected. Late melt is defined as the season during which the entire ice shelf is in a state of melt (Figure A1). Though shelf-wide melt had been occurring since early January (lowest σ^0 on 8 January, highest air temperature on 10 February), L-band SAR images for this season were only available in mid-February. Lastly, the freeze up season represents the period immediately after air temperatures and σ^0 have returned to pre-melt conditions.

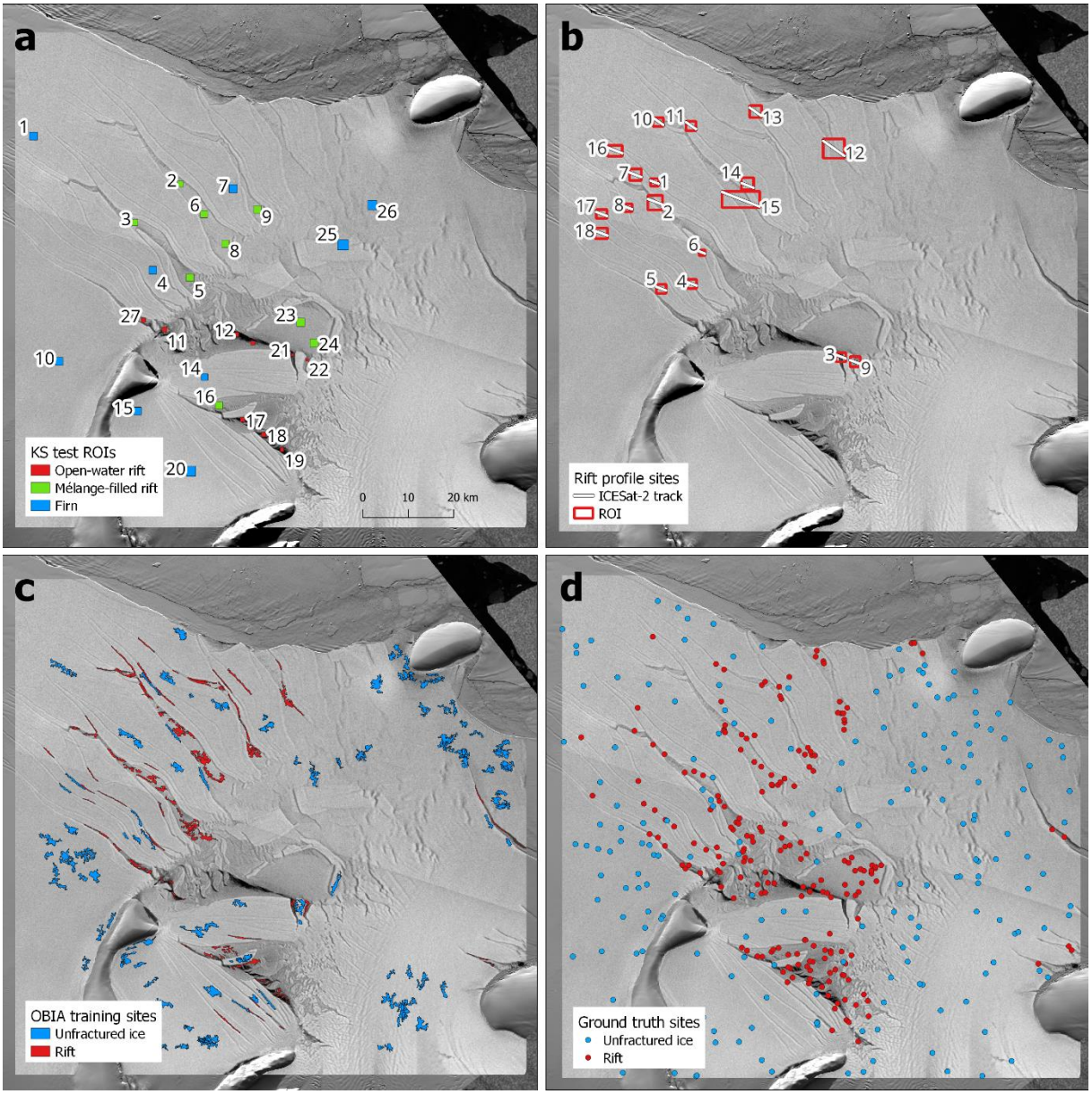

Figure 13. *Samples used for ice type separability (Section 4.3) and rift classification (Section 4.4).* ***(a)*** *ROIs used in KS tests with ROI numbers shown. Blue sites belong to the firn class, green sites are mélange-filled rifts, and red sites are open-water rifts.* ***(b)*** *Sites used for rift elevation and SAR backscatter profiles, with rift numbers and ICESat-2 tracks shown.* ***(c)*** *Training site polygons used in object-based classification, blue sites are unfractured ice and red sites are rifts.* ***(d)*** *Accuracy (i.e., ground truth) sites generated from truth polygons created in manual classification.*

4.3 Ice type separability and feature-wise backscatter analysis

Towards objective #2, five coincident pairs of dual-polarization HH and HV Sentinel-1 C-band, ALOS PALSAR-2 L-band, and SAOCOM L-band SAR images of the GIR rift system between September 2020 and March 2021 were analyzed to determine ice type separability. Scenes that aligned temporally with each of the five seasons were selected to ensure that ice surface

conditions throughout the whole melt year were adequately represented. Following visual identification, rift locations were validated and their geometry characterized using the ATL06 land ice heights product from ICESat-2. The ice surface throughout GIR was divided into three classes: firn (F), open-water rifts (OWR), and mélange-filled rifts (MFR) (Figure 13a). Nine regions of interest (ROIs) were selected for each class; ROIs were chosen such that most samples were within the boundaries of ASCAT-identified surface melt during the late melt dates (10 and 12 February; Figure A2, A3). Within each ROI, fifty random samples were generated, resulting in a total of 400 samples per class. Classes were identified using elevation from the REMA DEM and ice height from ICESat-2 ATL06 product, and depth was calculated by subtracting the ice height at the center or deepest part of the rift from the ice height at the top of the rift edge. Open-water rifts were characterized by having ≥ 20 m depth, very low backscatter values, and either no mélange or mélange far below the rift edge; most of these features expose the ocean below, thus their scattering signature is dominated by interaction with open water. Most of the observed open-water rifts are between 20-30 m deep, but some reach up to 35 m depth in their deepest parts. Mélange-filled rifts have ≤ 20 m depth and are filled with ice mélange that comprises much of the rift interior; in SAR images, these features appear as horizontal surfaces of brighter backscatter that extends just below the rift edge, giving them higher backscatter values and visually distinguishing them from darker open-water rifts. This class has a typical depth of 10-20 m, but the most important determinant is the presence of a mélange layer that comprises much of the interior and provides an additional scattering surface; small cracks and fractures that have a depth ≤ 20 m but do not contain this layer are not considered part of this class. It is important to emphasize that rift features are inherently full-thickness fractures with the same depth; therefore, "depth" in the context of this study refers only to the elevation difference between the rift edge and the rift interior. In the case of mélange-filled rifts, the fracture often extends to the ocean below but the thick mélange layer inside the rift reduces the elevation difference and causes the fracture to appear shallower. Lastly, the firn class refers to flat, undeformed regions of the ice shelf, i.e., those areas with no apparent cracks or fractures detectable upon visual inspection or with REMA/ICESat-2; this class is characterized by a deep firn layer that lies on top of shelf ice.

To generally assess the backscatter of the main ice features, the mean, standard deviation, and variance were calculated for each class, SAR frequency-polarization combination (herein termed "configuration"), and season to evaluate the spread of γ^0 values changes under each

condition. Unique configurations used in this study include C-band HH (C_{HH}), C-band HV (C_{HV}), L-band HH (L_{HH}), and L-band HV (L_{HV}). Kernel density estimates (KDEs) were used to represent the distribution of γ^0 values for each variable. The contrast ($\gamma^0_{\text{Class 1}} - \gamma^0_{\text{Class 2}}$) between mean γ^0 values was also calculated for each class combination (i.e., F-MFR, F-OWR, and MFR-OWR), across all configurations and seasons. Additionally, to evaluate how SAR backscatter varies across rift features, cross-sectional profiles of ice height and C- and L-band γ^0 were created for 18 rifts with varying shapes and depths using ICESat-2 tracks that crossed over the GIR between August 2020 and May 2021 (Figure 13b). The 18 profiles were organized by rift structure (i.e., wide and deep, wide and shallow, narrow and deep, narrow and shallow), and notable rifts from each structure type are discussed in Section 5.2.2. These profiles were also used to assess how rift detection and classification are affected by rift geometry (Section 6.2).

To evaluate statistical separability between the three ice classes, the two-sample Kolmogorov–Smirnov (KS) non-parametric test was used. The KS test is a goodness-of-fit test which finds the maximum distance between the empirical distribution functions of two samples to determine whether they are from the same underlying distribution (Dodge, 2003). This test was chosen as it does not assume normal distribution or equal variances. The KS statistic ranges from 0 to 1, where 1 indicates complete separability; KS statistics ≥ 0.7 were identified as reasonably separable. Prior to KS tests, z-score criteria were applied to remove outliers ± 3 standard deviations from the mean, and only significant ($p \leq 0.05$) results are reported. KS tests were performed for each class combination for all SAR configurations and seasons. Separability measurements differ from contrast measurements such that contrast measures the absolute difference in mean backscatter values between two classes, while separability considers the entire distribution and how well they can be distinguished from one another. Two classes may have high contrast but poor separability if their mean values are very different but there is a large overlap in their distributions (i.e., high degree of variance within each class). Conversely, two classes can be separable even if they have similar means and low variance, as long as their distributions do not significantly overlap.

Lastly, to further assess separability between firn and mélange-filled rifts, F-MFR ROI pairs with KS statistics < 0.7 were identified across all SAR configurations and seasons and the Bhattacharyya distance and coefficient were calculated for notable ROI pairs to assess the degree

of similarity and overlap between the distributions of the two samples (Dodge, 2003). The Bhattacharyya coefficient indicates the degree of overlap between the two distributions, while the distance indicates how dissimilar the mean values are (i.e., how far the distributions are from each other in feature space). A Bhattacharyya coefficient of 1 indicates complete overlap between distributions, while a coefficient of 0 indicates no overlap; Bhattacharyya distance values range from 0 to ∞ with larger values indicating a lower degree of similarity between distributions. In this case ROI pairs with a Bhattacharyya distance < 0.5 are considered to possess high similarity, while pairs with a distance > 1.5 possess low similarity. These measures provide insight into which characteristics contribute to low separability between F and MFR for each ROI.

4.4 Rift detection and classification

The process of rift classification in SAR images can be either pixel-based or object-based. Pixel-based techniques classify pixels based on their absolute spectral values. The classifier assigns a class label to each pixel using the pixel's colour, intensity, or reflectance values in different bands. In SAR imagery, the intensity values of each polarization band or derived bands (e.g., band ratios, texture measures, etc.) are used. Alternatively, object-based techniques (i.e., Object-Based Image Analysis (OBIA)) use a segmentation algorithm to separate coherent shapes composed of pixel groups, called segments, which are then used to classify the image. Segmentation divides the image into meaningful objects (groups of pixels) based on spectral similarity, texture, shape, and other attributes; the classifier then labels these objects instead of individual pixels. In contrast to pixel-based classification, object-based classification can also consider contextual features such as the size, relative/absolute location, and topological relationships between features (Blaschke et al., 2014).

Table 3. *List of all object- and pixel-based classifications tested. Object-based classifications tested more extensively to fully investigate the success and limitations of this approach.*

Object-based classifications	**Pixel-based classifications**
C-band HH & HV (freeze & melt) L-band HH & HV (freeze & melt) C+L-band HH & HV (freeze & melt) C-band HH & L-band HH (freeze & melt) C-band HV & L-band HV (freeze & melt) Optical panchromatic (freeze)	C-band HH & HV (freeze & melt) L-band HH & HV (freeze & melt) C+L-band HH & HV (freeze & melt)

For objective #3, to evaluate how successful different SAR configurations were at identifying rifts, supervised classifications were performed using pixel- and object-based techniques with three main combinations: C-band, L-band, and C+L-band (Table 3). Here, the C-band configuration represents the combined use of C_{HH} and C_{HV} images as separate input channels during classification; similarly, L-band uses L_{HH} and L_{HV} and C+L-band uses C_{HH}, C_{HV}, L_{HH}, and L_{HV}. Object-based classifications were also tested with a Landsat 8 panchromatic image, and with HH and HV polarizations, as per Table 3. Both pixel- and object-based approaches were tested during freeze (September 2020) and melt conditions (February 2021; Table 2); since the goal is to determine whether an object- or pixel-based approach works better, only a freeze case and a melt case were selected for testing. Classifications also used only two ice surface classes, "Unfractured ice" and "Rift," where Rift includes both OWR and MFR features; the OWR and MFR classes were combined to facilitate future rift classifications and detection studies, which would likely only be concerned with fractured vs. unfractured ice.

Table 4. *Attributes calculated from objects and used in the OBIA classification.*

Statistical	**Geometric**	**Texture**
Minimum σ^0 Maximum σ^0 Mean and standard deviation of σ^0	Elongation Compaction Circularity Rectangularity	Mean and standard deviation of GLCMs Entropy of GLCMs Angular second moment of GLCMs Contrast of GLCMs

For object-based classification, the Object Analyst module in the software CATALYST Earth was used (CATALYST Earth, n.d.). The first step in the OBIA process, prior to training and classification, is segmentation. After several tests, the most effective segmentation layer, based on a visual assessment of the segmentation result (i.e., human vision system confirmation) was created with panchromatic optical and L-band SAR. Specific criteria regarding scale, shape, and compactness are used by CATALYST Earth to constrain the segmentation: a scale value of 100, shape value of 0.5, and compactness value of 0.7 was used since they produced objects that best reflected the narrow, elongated shape of rifts. A moderate shape parameter places equal weight on the colour (i.e., γ^0 value and panchromatic reflectance) and shape characteristics, while a moderate to high compactness parameter helps avoid over-segmentation due to speckle noise and allows for extraction of features that are closely spaced and differentiated only by weak spectral contrast. After segmentation, 150 training objects were selected for each class, with emphasis on

maximizing the spectral and geometric diversity of features (Figure 13c). Statistical, geometric, and texture attributes (Table 4) were calculated for each object prior to classification; statistical attributes were calculated from the γ^0 values of the objects, while texture attributes were calculated from the grey-level co-occurrence matrices (GLCMs).

The final OBIA step was classification, here performed using the SAR sensor configurations shown in Table 3 and a Random Forest (RF) algorithm. Random forests are a popular machine learning algorithm used for classification and other predictive tasks. The algorithm is an ensemble learning method, meaning it combines multiple decision trees to make a prediction (Breiman, 2001). In classification, input data are split into branches depending on feature values and the separation between classes; this process continues until it satisfies a condition (i.e., maximum tree depth, minimum samples per leaf, etc.), resulting in a tree structure where each leaf represents a prediction. After enough trees are generated, the algorithm votes for the most popular class, and the feature is assigned (Breiman, 2001). The RF algorithm was chosen as it handles overlapping data well due to ensemble learning; this reduces noisy data patterns and allows modelling of complex, non-linear relationships between classes (Breiman, 2001). RF is also generally less sensitive to parameter choices, producing good results without excessive tuning of the algorithm. The object-based classifications used a maximum tree depth of 25 and maximum tree number of 200, whereas pixel-based classifications used a maximum tree depth and maximum tree number of 100.

4.4.1 Classification accuracy assessment

Classification accuracy is reported using three measures: the overall accuracy, the Kappa Coefficient (κ), and the percent agreement with a manually classified "truth" polygon layer created in QGIS. Overall accuracy reflects the proportion of the classified objects that were correctly classified, with 100% being a perfect classification; values are calculated using the number of correctly classified sites over the total number of reference sites. We report on the producer's accuracy, which refers to the probability that a class is correctly identified. κ is a measure of interrater reliability, which evaluates how well the classification performs compared to random assignment; values range from -1 to 1, with 0 indicating that the classification performance is equivalent to random, +1 indicating performance is significantly better than random, and -1 is

significantly worse than random. Overall accuracy and κ were retrieved from the confusion matrices computed in the Object Analyst module. To compute the confusion matrices, CATALYST Earth requires ground truth point samples to compare the classification results to; these were created in QGIS by generating 200 random samples within the "Unfractured ice" and "Rift" class layers (Figure 13d). Overall accuracy values from the confusion matrices were supplemented by comparing the percent agreement (i.e., percent of overlap) between automatically and manually classified objects. To ensure the robustness of the accuracy assessment, the mean of the overall accuracy and the percent agreement were taken; these values are reported when discussing classification accuracy. Classification accuracy is discussed for both the entire classification, and for the two classes independently to determine if a bias exists towards one class.

5 Results

5.1 Visibility of the LC2017 rift and qualitative comparison of satellite sensors

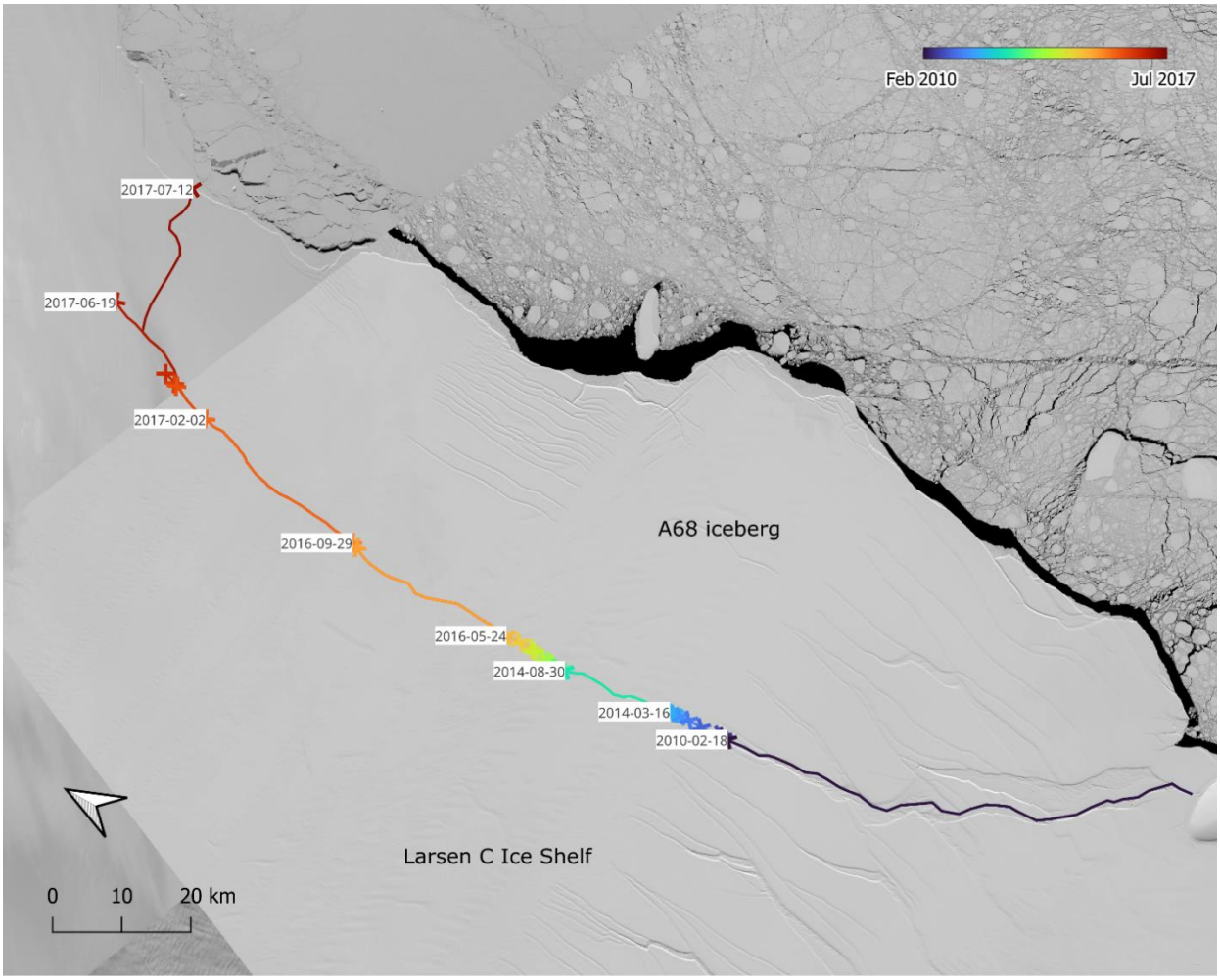

***Figure 14**. Propagation path of the LC2017 rift from January 2012 to July 2017 as delineated from Landsat 8 and Sentinel-1. "X"'s indicate confirmed length increases and the track is colorized using a graduated symbology for each rift segment. Background images are Landsat 8 images from 2 February 2016 and 16 April 2017.*

The LC2017 rift was present on the LCIS as early as 2005 (Borstad et al., 2017). At the start of monitoring in this study (February 2010), the rift was approximately 72 km long, extending roughly northward from the GIR (Figure 14). The rift was dormant until 2014, maintaining a length below 81 km; during this time, the rift tip was located within the Joerg Peninsula suture zone, which slowed the rate of propagation (Walker & Gardner, 2019). Between March and August 2014, the rift exited the suture zone and grew up to 98 km; it then entered a second suture zone (Borstad et al., 2017) and slowly propagated to 108 km until 2016, when it began experiencing

rapid growth and surged to 134 km between May and July. These growth rates were maintained until the A68 iceberg calved. By February 2017, the rift was 163 km in length, grew to 170 km from February to March, and reached 185 km by June. The rift then turned eastward and propagated to the shelf front, calving into A68 at a final length of 200 km on 12 July. The rift track discussed here follows the observations made in Borstad et al. (2017) and was created based on Landsat and Sentinel-1 imagery; therefore, the track follows the surface- or near-surface-level expression of the fracture and does not include any changes in size that occur within the depth of the rift.

This case study presents an example of how various sensors and frequencies differ in their ability to detect and monitor ice shelf rifts. Of main concern in this case was the discrimination of the rift tip, as this is the smallest and most difficult portion of the rift to identify and has the greatest relevance to studies looking to monitor rift growth. The higher resolution of Landsat allows for discrimination of the rift tip at finer spatial scales when compared to C- or L-band SAR. Although Sentinel-1 has roughly the same spatial resolution as Landsat (20 m for Sentinel-1 IW, 15 m for Landsat panchromatic), the Sentinel-1 images include speckle noise and reducing this effect using spatial filtering effectively decreases the image resolution. As a result, through qualitative examination, it is difficult to pinpoint the exact location of the rift tip in Sentinel-1 imagery. Here, the panchromatic optical scene provides an advantage over the C-band SAR scene by providing a clear view of the rift tip without interference from speckle. As is the case with optical imagery, continuous monitoring of rift size is challenging due to limitations in data availability during the austral winter and the presence of clouds. C-band therefore provides a view of the rift at a higher temporal resolution as imagery is unaffected by cloud cover and the polar night.

When comparing rift characteristics between satellite sensors, changes in rift structure are observed more effectively with SAR imagery. During the 2010-2017 study period, C- and L-band SAR highlighted changes in rift width that were not visible in panchromatic optical. One example is the case of 14-16 December 2015, where Sentinel-1 showed a widening of the rift by ~30-50 m while Landsat did not show any change in rift geometry. The most striking example of the superiority of SAR – particularly L-band – for monitoring rift activity is the detection of a thin, 100+ km crack with PALSAR-2 as early as 22 August 2014; this crack is never visible in any of the examined optical or C-band scenes (Figure 15). Propagation of the main rift does not occur

along the path of this crack, but growth patterns are oriented in the same direction for the duration of the rift's lifetime. While the fracture is clearest in winter L-band imagery, it is still visible in the summer scene, though slightly more blurred.

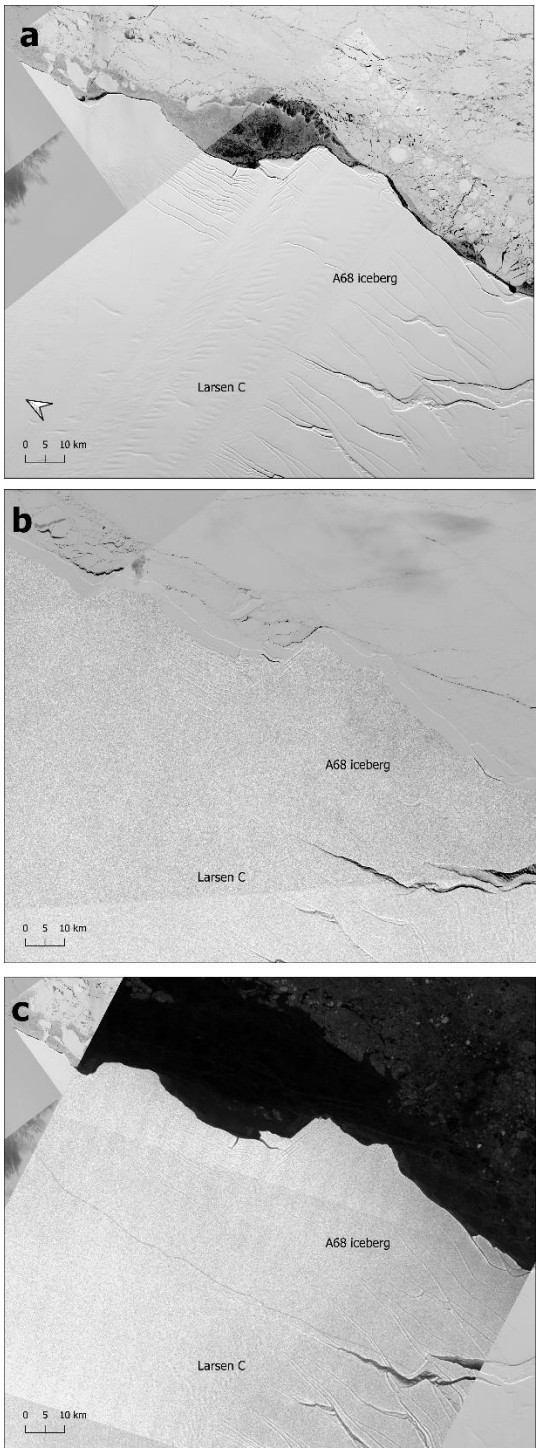

Figure 15. *Differences in rift visibility between* ***(a)*** *Landsat 8 panchromatic band, retrieved on 1 September 2014,* ***(b)*** *Sentinel-1 HH, retrieved on 17 January 2015, and* ***(c)*** *PALSAR-2 HV, retrieved on 22 August 2014*

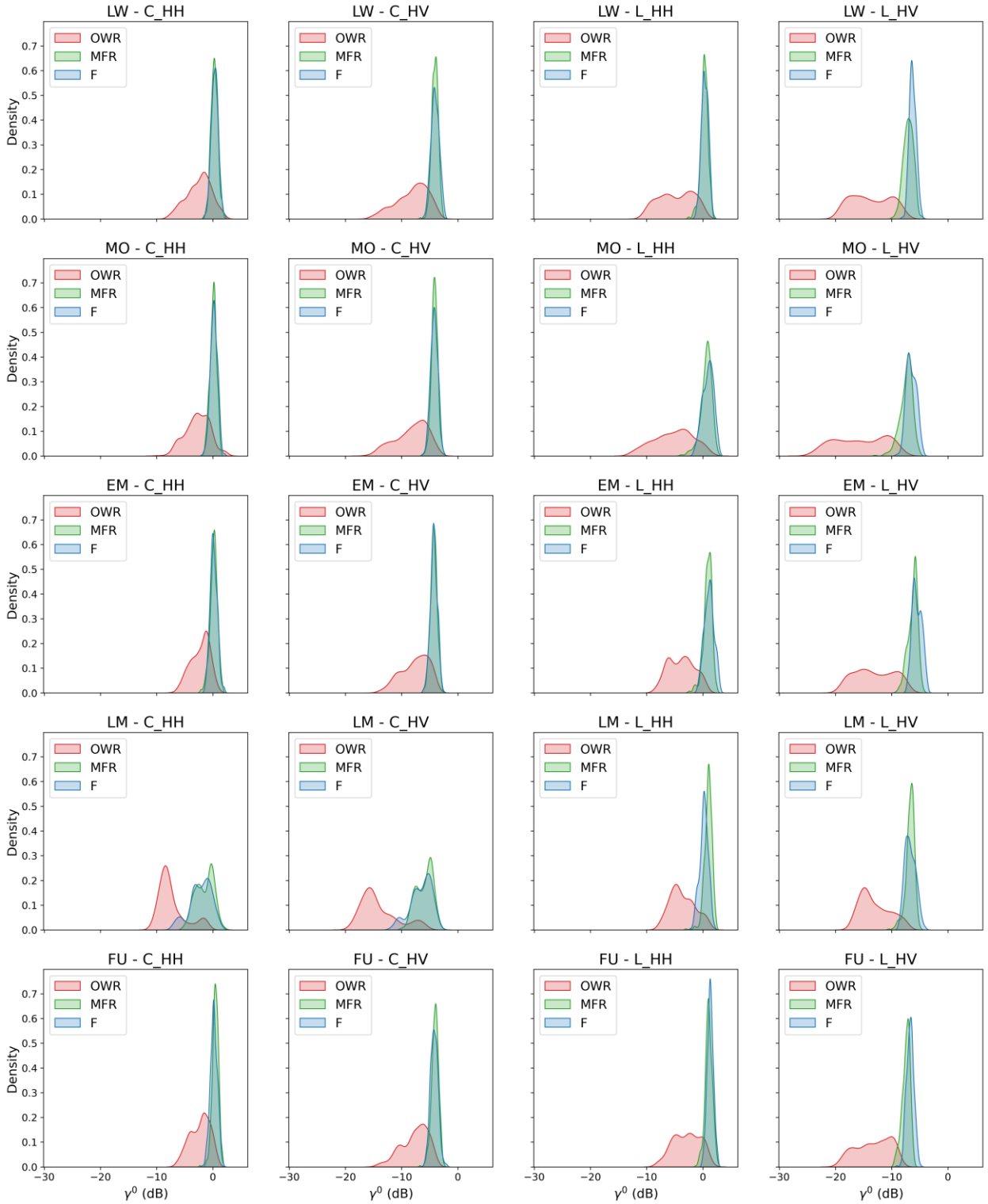

Figure 16. *Kernel density estimates of firn (F), mélange-filled rifts (MFR), and open-water rift (OWR) backscatter, for all configurations (C: C-band frequency; L: L-band frequency; HH and HV polarizations) and seasons (LW: late-winter; MO: melt onset; EM: early melt; LM: late melt; FU: freeze-up).*

5.2 Backscatter statistics and melt trends

Upon visual inspection of rifts in SAR images, large, open rifts appear as linear features that maintain very low γ^0 compared to the surrounding ice throughout all seasons, independent of SAR frequency or polarization. The backscatter from within these rifts is at or near the noise floor and a high backscatter line can often be seen at the farthest edge due to radar foreshortening. Thin or buried/snow-bridged fractures and mélange-filled rifts also appear as linear features with low γ^0, though these features have higher γ^0 than that of open-water rifts. Wide fractures are more easily distinguishable than narrow fractures as they display two linear edges, while narrow fractures appear only as one small line and become increasingly difficult to identify as image resolution is reduced; the fracture width must exceed the image resolution to be reliably detected. Melt in SAR images also appears as a dark region with very low γ^0, which closely overlaps the backscatter from rifts. Rifts are therefore more visible in winter imagery that allows for deep penetration of surface snow and ice mélange and is not complicated by surface melt. L-band imagery offers enhanced visibility of rifts compared to C-band and optical imagery, revealing the true structure and location of fractures even before any separability analysis has taken place.

5.2.1 ASCAT time series

Unfractured ice during the winter season is characterized by high ASCAT σ^0 (~0 dB) when air temperatures are typically below -10°C (Figure 12). Starting in October, there is a clear warming trend until early November. There is a sudden melt event from 1-8 November, where air temperature rises above 0°C and σ^0 is reduced to -7.5 dB. Melt begins in the northwest corner of the ice shelf at the base of the mountains (Figure A4), erupting into near-complete melt of the LCIS with melt extent peaking on 5 November. This is followed by a brief period of refreezing, which can be seen through a reduction in air temperature down to -8°C and an increase in σ^0. Melt during this time is focused around the Cabinet, Mill, and Whirlwind inlets until early December. While full melt may not be achieved throughout the GIR region in the melt onset and early melt dates, σ^0 in this area is consistently 1-2 dB below the winter mean, which indicates minor changes in the surface characteristics and liquid water content of the ice. Widespread surface melt occurs from 8 December to 5 March, with the entire LCIS in a state of melt from 29 December to 12 January. This period is characterized by very low σ^0 values and fluctuating but warm air

temperatures, often rising above 0°C; the highest air temperature of 2°C occurs on 10 February 2021. On 8 January 2021, σ^0 reaches its lowest at -15 dB, indicating widespread surface melting and the presence of liquid water on the ice, which drastically reduces backscatter. By March, air temperatures have begun to drop and σ^0 increases again, reflecting the freezing of the ice and a return to winter conditions. Throughout all seasons, OWR shows consistently low backscatter compared to MFR and F (Figure 16). Mélange-filled rifts exhibit higher backscatter than open-water rifts, particularly in HH polarization; this indicates enhanced scattering from mélange-filled rifts compared to open-water rifts, which do not return as much of the radar signal. In melt conditions, open-water rifts show significantly reduced backscatter compared to firn and mélange-filled rifts, likely due to increased signal attenuation from ocean water. The range of backscatter values during melt for all classes increases at C-band frequency, while the L-band range is relatively unchanged.

5.2.2 ICESat-2 rift profiles

Wide, deep rifts are easily detected in SAR imagery due to their very low γ^0 signatures (Figure 17a) and sharp contrast with the surrounding ice; this is evident in the profile through a greater difference between rift edges and interior. These rifts possess a width ~500-1,000 m and a depth > 20 m. A strong reduction in γ^0 occurs across the rift profile for both frequencies, though C-band profiles display lower contrast and occasionally a spike in γ^0 in the interior of the rift due to signal return from ice mélange. Narrow, deep rifts with a width of ~200-400 m and a depth of 20-25 m are also well identified in SAR images, though the fine rift tip is often obscured in C-band images due to speckle noise (Figure 17b). Wide but shallow rifts (~1-2 km wide, 10-15 m deep; Figure 17c) possess a thick m that comprises much of their interior. These rifts are easy to visually identify in SAR imagery, though the mélange layer very closely resembles the surrounding unfractured firn surfaces due to its similar relief and γ^0 values. Narrow fractures with a shallow depth (~100-200 m wide, 5-10 m deep; Figure 17d) are more difficult to identify. These fractures often do not show enough contrast with their surroundings to stand out in SAR imagery, particularly amongst highly variable γ^0 signatures from speckle noise and surface melt. Once again, it is important to acknowledge that the depth discussed here refers to the difference between the rift edge and the interior mélange layer and therefore may not be entirely representative of the true depth of full-thickness fractures.

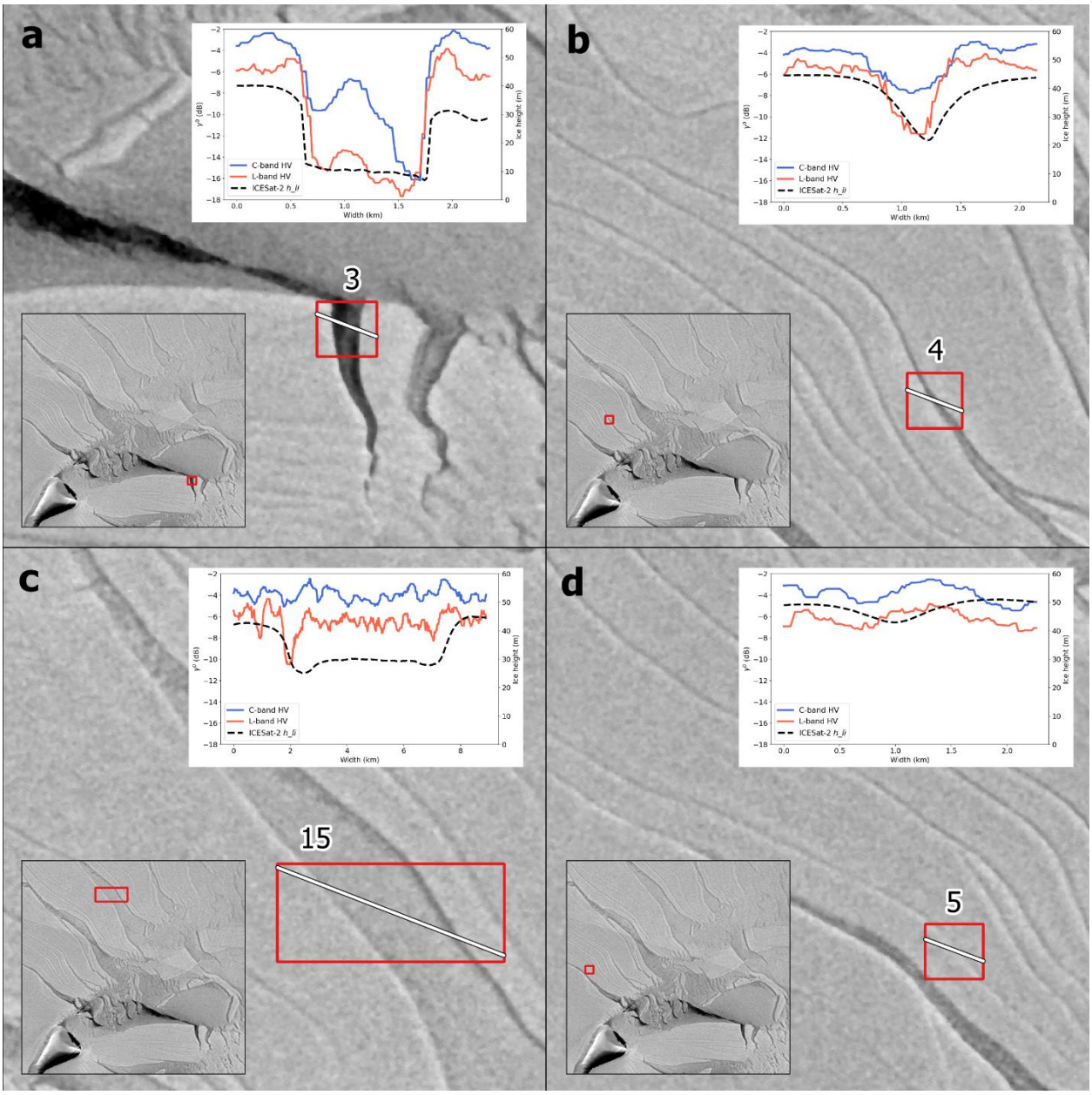

Figure 17. *Cross-sectional profiles of elevation and C- and L-band backscatter for different rift types, where h_li is ICESat-2 land ice height and C- and L-band γ^0 is Sentinel-1 and PALSAR-2 backscatter, respectively.* ***(a)*** *Wide, deep rift (ROI #3).* ***(b)*** *Narrow, deep rift (ROI #4).* ***(c)*** *Wide, shallow rift (ROI # 15).* ***(d)*** *Narrow, shallow rift (ROI #5).*

5.3 Evolution of ice type separability throughout the melt year

5.3.1 Late winter

During the winter, OWR has notably lower γ^0 and higher variance compared to F and MFR; this shows a greater spread of γ^0 values, which enhances the discrimination of this class from

others. L-band frequency offers improved contrast over C-band between OWR and other classes (Figure 18a,b). While HV polarization consistently outperforms HH for separating DR, good separability is maintained in both polarizations (Figure 19a,c); this indicates that OWR is not as sensitive to polarization changes as the other two classes. L_{HV} offers the greatest contrast and separability between OWR and F (7.46 dB; KS = 0.99), and OWR and MFR (6.69 dB; KS = 0.90). Alternatively, F and MFR show similar γ^0, and relatively low variance for all configurations; this suggests that the samples for these classes are more homogeneous and F and MFR may be less distinguishable. This is especially true for HH polarization, as there is almost no contrast for F-MFR (Figure 18c). Noticeable increases in contrast and separability between these classes occur with L_{HV} (0.77 dB; KS = 0.42; Figure 19b); however, it is important to note that the KS statistic is still < 0.7. The small mean difference and low variance between these classes in other configurations support their poor separability.

5.3.2 Melt onset and early melt

At the onset of melt, OWR shows a significant drop in γ^0 across almost all configurations as the liquid water content of the ice increases. F and MFR also display a drop in γ^0 in all configurations except L_{HH}. OWR maintains its internal variability as variance and standard deviation remain higher and γ^0 remains distinctly negative compared to other classes. Contrast and separability are also consistently higher between OWR and other classes; contrast is above 2.5 dB for HH and 4 dB for HV, and KS > 0.7 for all configurations. L_{HV} continues to provide the greatest contrast and separability for all classes, though F and MFR maintain the poor separation as during winter (~0 dB; KS = 0.3) As the season progresses into early melt, the general behaviours remain the same; greater contrast is found with HV , though slightly reduced compared to melt onset, and OWR is the most well-separated class. γ^0 increases relative to melt onset for nearly all configurations. Variance generally decreases except for MFR in C-band channels; this indicates that this class experiences an increase in spectral variability after the refreezing period. L_{HV} remains superior and F and MFR remain inseparable.

5.3.3 Late melt

During late melt, surface conditions become more heterogeneous as widespread surface melt is present. γ^0 decreases for all classes and the spread of values increases, except for OWR and

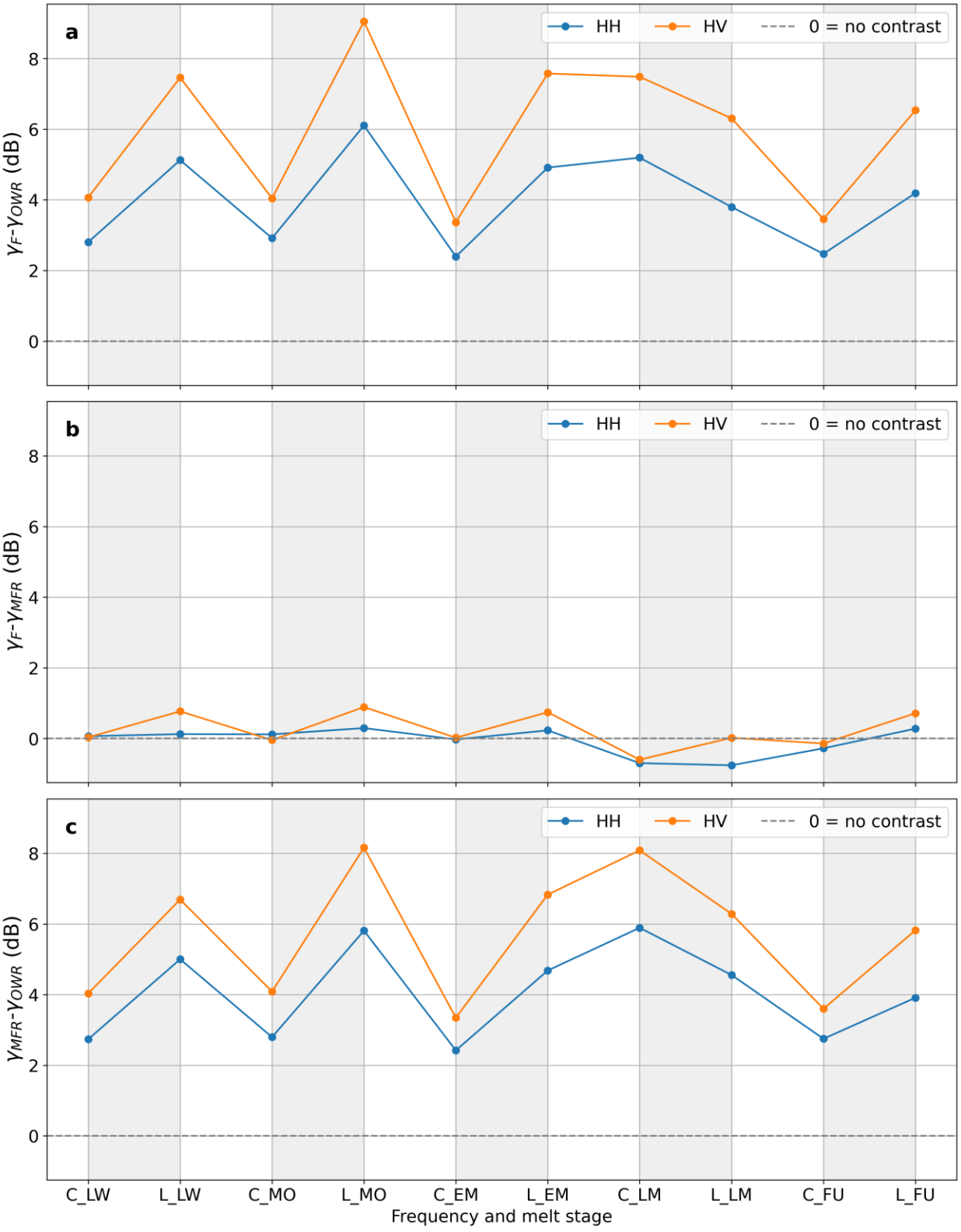

Figure 18. *Mean backscatter contrast between* ***(a)*** *F-OWR,* ***(b)*** *F-MFR, and* ***(c)*** *MFR-OWR for each SAR configuration and season. The blue line refers to HH polarization and the orange line refers to HV. Dotted grey line represents no contrast. Values are reported in decibels.*

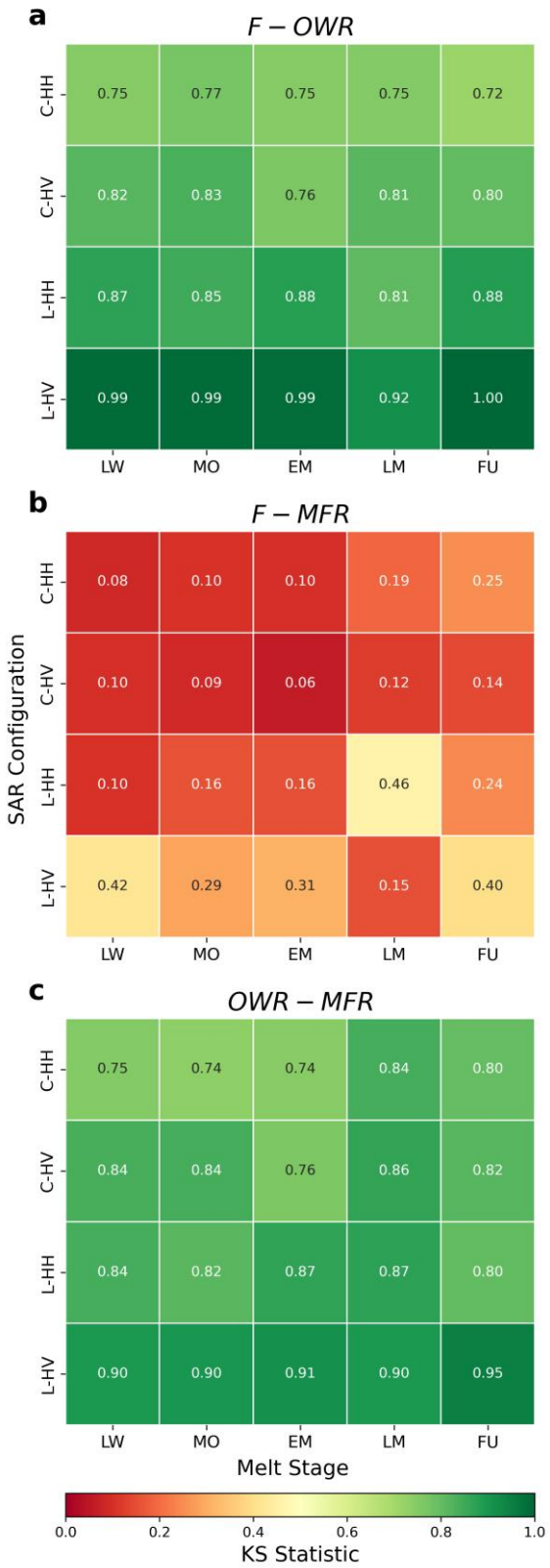

Figure 19. *Kolmogorov-Smirnov statistics for* ***(a)*** *F-OWR,* ***(b)*** *F-MFR, and* ***(c)*** *OWR-MFR throughout all seasons for various SAR configurations. Green indicates classes with high separability, and red indicates low separability.*

MFR in L-band. OWR maintains lower γ^0 and higher variance than other classes. The contrast between all classes is higher at C-band, though the separability is higher at L-band. As in the winter, high contrast and separability (> 4 dB; KS > 0.7) for OWR is maintained for all configurations and L_{HV} continues to offer the greatest separation. F and MFR show a negative relative contrast for both polarizations at C-band and for HH polarization at L-band, i.e., MFR γ^0 is higher than F γ^0 for these configurations during this season. Contrast and separability between F and MFR are highest with L_{HH} polarization (-0.76 dB; KS = 0.46); this is notably different from other seasons, which showed the superiority of L_{HV} for separating the two classes. Overall, this could indicate an increased presence of double-bounce scattering from the mélange layer and the rift walls compared to other seasons, where the lower depth of the mélange layer, compared to OWR, enables more signal return to the sensor.

5.3.4 Freeze up

During freeze up, the surface begins to roughen again as it refreezes. This season reflects a return to winter conditions as γ^0 values begin to rise and the ice surface becomes colder and drier, enhancing signal penetration into the volume. All classes experience an increase in γ^0 for all configurations except L_{HV}, though the change is more pronounced in C-band channels. Variance and standard deviation decrease for all classes and configurations, with the exception of OWR in L-band channels. The contrast between OWR and other classes generally decreases from the late melt season, while separability increases. Contrast returns to being higher in L-band channels and is positive for F and MFR, indicating that MFR γ^0 is once again higher than F γ^0. L_{HV} returns to providing the greatest contrast and separability between all classes, including F and MFR, though these classes continue to be poorly separated.

5.4 Pair-wise separability between class ROIs

This section addresses the separability between notable ROI pairs; this provides insight into the processes controlling the separability between the three classes and evaluates why high or low separability occurs between certain ROIs. The two F-MFR ROI pairs with the lowest consistent separability are ROI #2 and #7, and ROI #26 and #23; these pairs have a KS statistic below 0.2 for all configurations and seasons. Both ROIs for these pairs fall within a flat region of

the ice shelf with low γ^0 variation (Figure 20a, Figure 21), which makes it difficult to separate them from other ROIs. ROIs with poor separability have high Bhattacharyya coefficients (0.94-1; Figure 22a) and low Bhattacharyya distances (< 0.5; Figure 22b). Here, behaviours in separability and contrast between classes hold true to the behaviours observed for the full separability dataset: the greatest separability and contrast occur with L_{HV} during late winter and L_{HH} during late melt. Alternatively, the pair #15 and #9 has a KS statistic above 0.8 for all configurations and seasons. ROIs with relatively good consistent separability are within regions with very different γ^0 values; in the case of #15 and #9, ROI #15 is located in a region of the ice shelf that appears to be shadowed from the topography around Cape Agassiz and is darkened by surface melt, while ROI #9 is located in a region with less melt and no shadow (Figure 20b). For this pair, the Bhattacharyya coefficients are still quite high (0.56-0.89), and the distances are low (< 0.5). This indicates that the distributions for this ROI pair have a lower degree of overlap than #2 and #7, though not as low as ROI #26 and #21, which is a F-OWR pair. Separability for the #15 and #9 pair differs slightly from the behaviour typically observed with F-MFR pairs. Typically, the greater penetration depth of L_{HV} offers better discrimination of the mélange layer and enhances the separability between the two classes during the winter; however, the shadow observed in ROI #15 reduces the γ^0 values for this sample, causing the two ROIs to display a greater degree of similarity. Additionally, the ROIs for this pair have a greater difference between γ^0 values for C-band, though this difference likely occurs due to more severe melt present in ROI #15 during the Sentinel-1 date. While melt is present for this ROI in both scenes, the degree of γ^0 reduction is slightly greater on February 10 compared to February 12 (Figures A3 and A4).

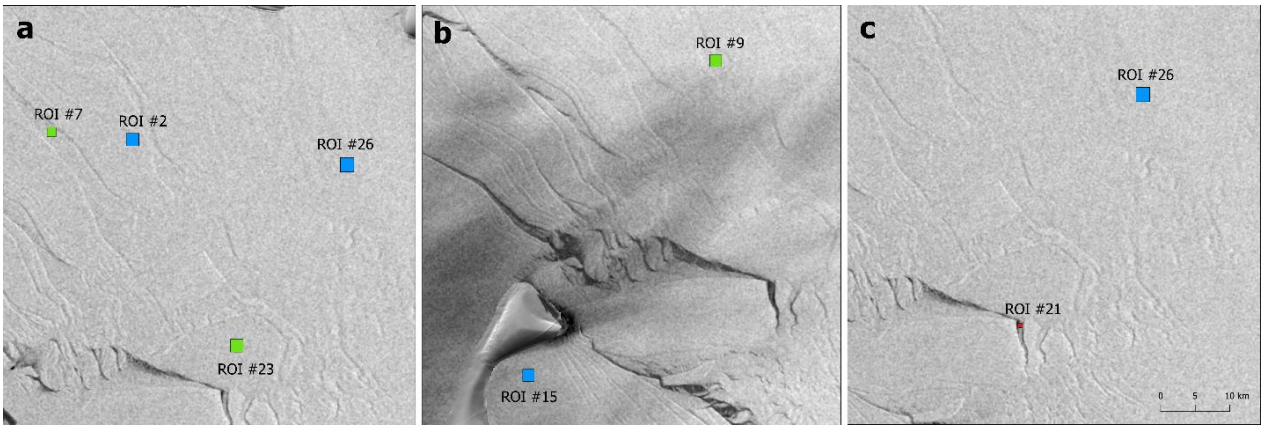

Figure 20. *Location of ROI pairs discussed in Section 5.4.* ***(a)*** *Poorly separated F-MFR pairs ([2,7], [26, 23]), shown against C_{HH} late winter scene.* ***(b)*** *Well separated F-MFR pair ([15, 9]) shown with C_{HH} late melt scene.* ***(c)*** *Well separated F-OWR pair ([26, 21]) with C_{HH} late winter scene. All SAR scenes have been converted to decibels.*

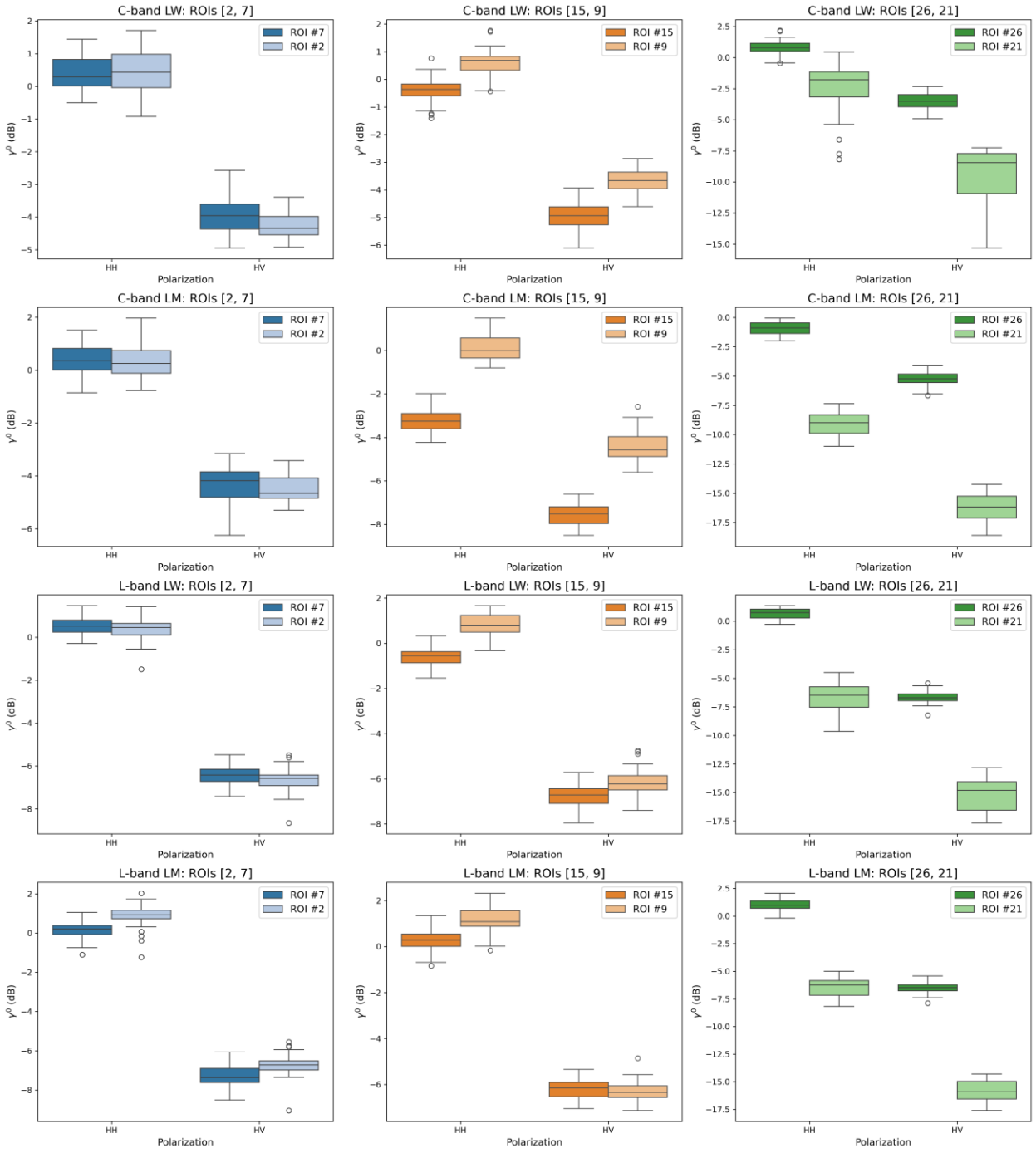

Figure 21. *Box plots showing range of backscatter values for each ROI pair. C-band values are shown in the first two rows and L-band values in the last two; HH polarization is shown in the left side of the box plot and HV polarization in the right. ROI pairs are grouped into columns differentiated by color. Pair [2, 7] (blue) represent firn and mélange-filled rift ROIs that are consistently poorly separated, with KS < 0.7 across all configurations. ROI pair [15, 9] (orange) is a firn and mélange-filled rift pair that have the highest consistent separability (KS > 0.8) among all F-MFR pairs. Pair [26, 21] (green) is a firn and open-water rift pair of ROIs with KS = ~1.0 across all configurations. Backscatter values for C- and L-band HH and HV are shown for the late winter and late melt season and reported in decibels.*

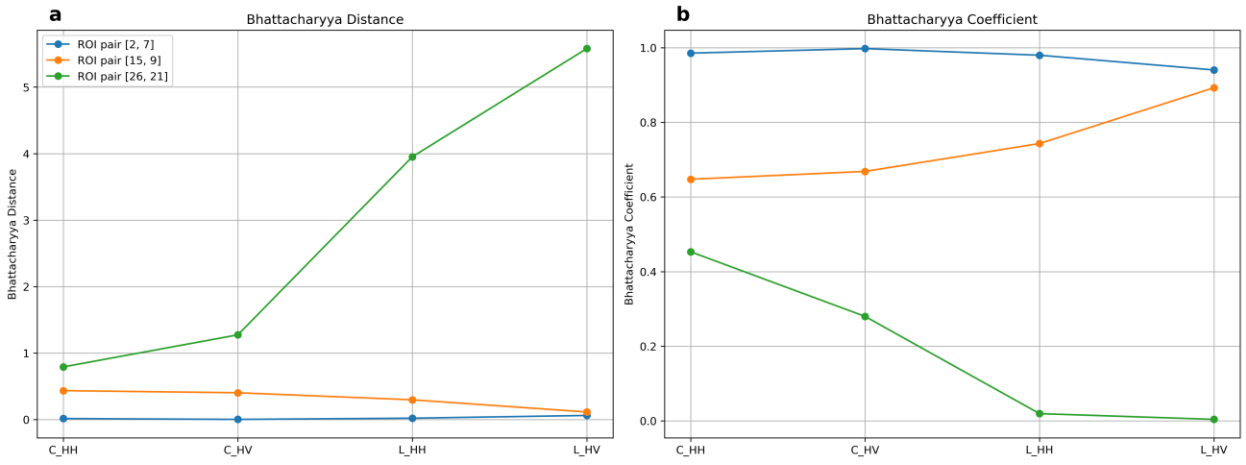

Figure 22. *Bhattacharyya metrics for ROI pairs discussed in Section 5.4, for each SAR configuration.* ***(a)*** *Bhattacharyya coefficients.* ***(b)*** *Bhattacharyya distances. ROI pair [2, 7] (blue) represents a poorly separated F-MFR ROI pair, [15, 9] (orange) is a well separated F-MFR pair, and [26, 21] (green) is a well separated F-OWR pair.*

The ROI #26 and #21 pairing represents samples for the firn and open-water rift classes, respectively. These classes show good class separability for all SAR configurations throughout the entire melt year. This pair reflects a F-OWR pair that is among the pairs with the highest consistent separability, with KS statistics all around 1.0. Bhattacharyya coefficients are close to 0 and distances are above 1.0 for all configurations except C_{HH}; this indicates that γ^0 values for this pair are very dissimilar and that their distributions only slightly overlap with C-band. The open-water rift ROI for this pair is located within one of the most well-identified rifts throughout the GIR region; this is a wide (~1 km), deep rift (Figure 17a) that is identified in all classifications tested and displays very low γ^0 values across all SAR configurations. Conversely, the firn ROI for this pair is located in a very flat region of the ice shelf that consistently displays high γ^0 values (Figure 20c). As a result, the γ^0 contrast between these ROIs is high and the samples are consistently very well separated.

5.5 Classification of rifts

Visual inspection of classification results indicates that the L-band and C+L-band classifications during freeze produce the best results and succeed at correctly identifying rifts, while eliminating the unfractured firn surfaces on either side of the rift (Figure 23a,b). C+L-band successfully identifies the complex rifted area directly to the west of Cape Agassiz; this area consists of fractures with varying depths, high concentrations of ice mélange, and large calved blocks, therefore presenting a highly variable surface to assess which features the classification

can separate. Both C-band and HH polarizations struggle to classify rifts, particularly during the melt phase (Figure 23d-f). The C-band classification during freeze, and all classifications during melt contain many objects that are misclassified as rifts. Optical classifications succeeded at identifying narrow rifts due to enhanced spatial resolution; however, shallow snow-bridged rifts, ice rumples, and areas partially covered by cloud were poorly classified. During segmentation, C-band SAR scenes did not produce objects that resemble the shape of rifts; these objects were highly fragmented and often followed the organization of speckle noise present in the imagery, which resulted in inaccurate identification of rifts and poor classification performance. Optical images produced very clear objects that were not affected by speckle, but they struggled to properly segment mélange-filled rifts or small, buried cracks that are not expressed at the surface. In contrast, L-band is less affected by speckle noise, can detect buried cracks and mélange-filled rifts, and segmentation using L-band scenes produced objects that closely resembled the shape of rifts during both freeze and melt conditions. Therefore, the combination of high-resolution optical and HH and HV L-band imagery performs well during segmentation and produces high-quality objects; consequently, this combination was used to produce the objects for all classifications.

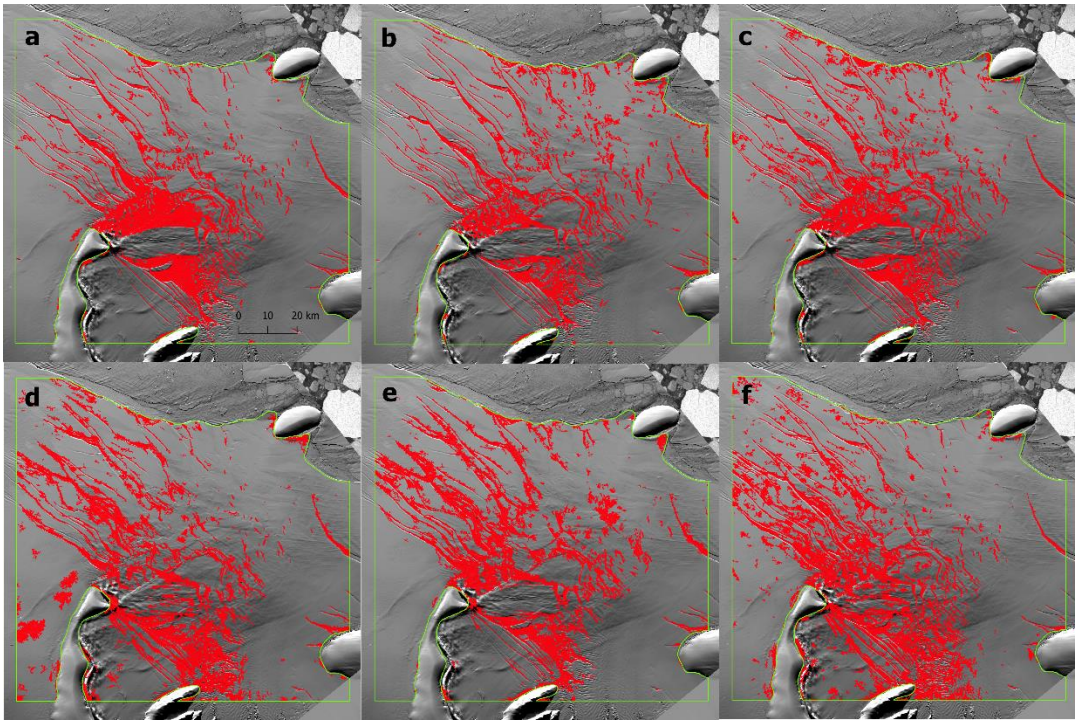

Figure 23. *Object-based classifications with the three highest and lowest classification accuracies. Classified rifts shown in red. Background image is Landsat 8 panchromatic band from 30 August 2020. Highest performing classifications:* ***(a)*** *C+L-bands freeze,* ***(b)*** *L-bands freeze,* ***(c)*** *HV bands freeze. Lowest performing classifications:* ***(d)*** *C-bands melt,* ***(e)*** *HH bands melt,* ***(f)*** *C-bands freeze.*

Object-based classification greatly improved the detection of rifts relative to pixel-based classification, though its success was highly dependent on the segmentation process, as images that do not produce quality segments will not produce quality classifications (Hossain & Chen, 2019). Classifications with parameters which are more sensitive to volume scattering (i.e., L-band, C+L-band, HV band) tend to have the greatest classification accuracy and κ values. Classification accuracy and κ are higher for all fields during freeze conditions; the greatest accuracy occurs with C+L-band, with 87.9% of objects classified correctly. HV band (C_{HV} and L_{HV}) consistently outperforms HH band (C_{HH} and L_{HH}), and C-band consistently shows the lowest accuracy and poorly classifies both the Unfractured ice and Rift class. The greatest classification accuracy for both classes occurs with C+L-band during freeze. The Unfractured ice class generally has a higher accuracy than the Rift class, but a consistently lower κ.

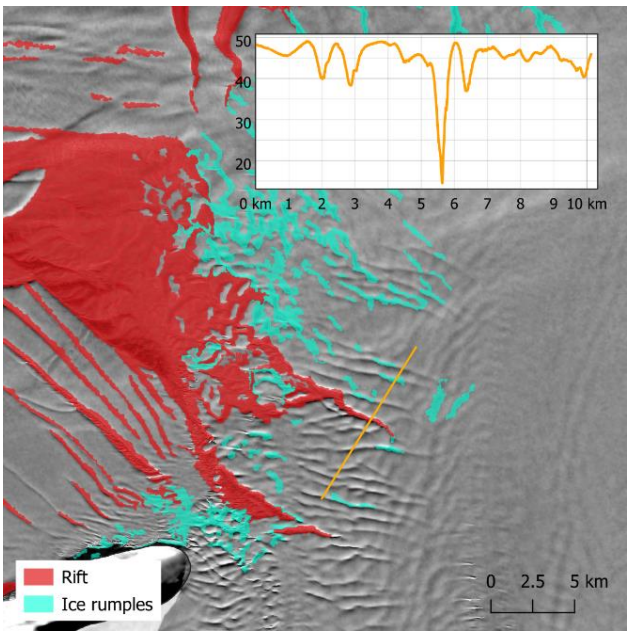

Figure 24. *Ice rumples misclassified as rifts with object-based L-band classification during freeze. Rifts shown in red and misclassified ice rumples shown in cyan. Inset plot shows a REMA DEM elevation profile across a rift and a surrounding ice rumple field.*

Features such as ice rumples and minor variations in ice height are often misclassified as rifts due to shadow (Figure 24); the inclusion of L-band improves the classification of these features as well. In all cases, L-band provides enhanced γ^0 contrast between the rift interior and the surrounding ice due to greater penetration into snow and ice mélange, though this is most pronounced with wide, deep rifts. Ice rumples are successfully classified during object-based classification though this technique tends to include many adjacent objects. In contrast, the pixel-

based classification classifies only the darkest ice rumples, which tends to reduce misclassification of these features.

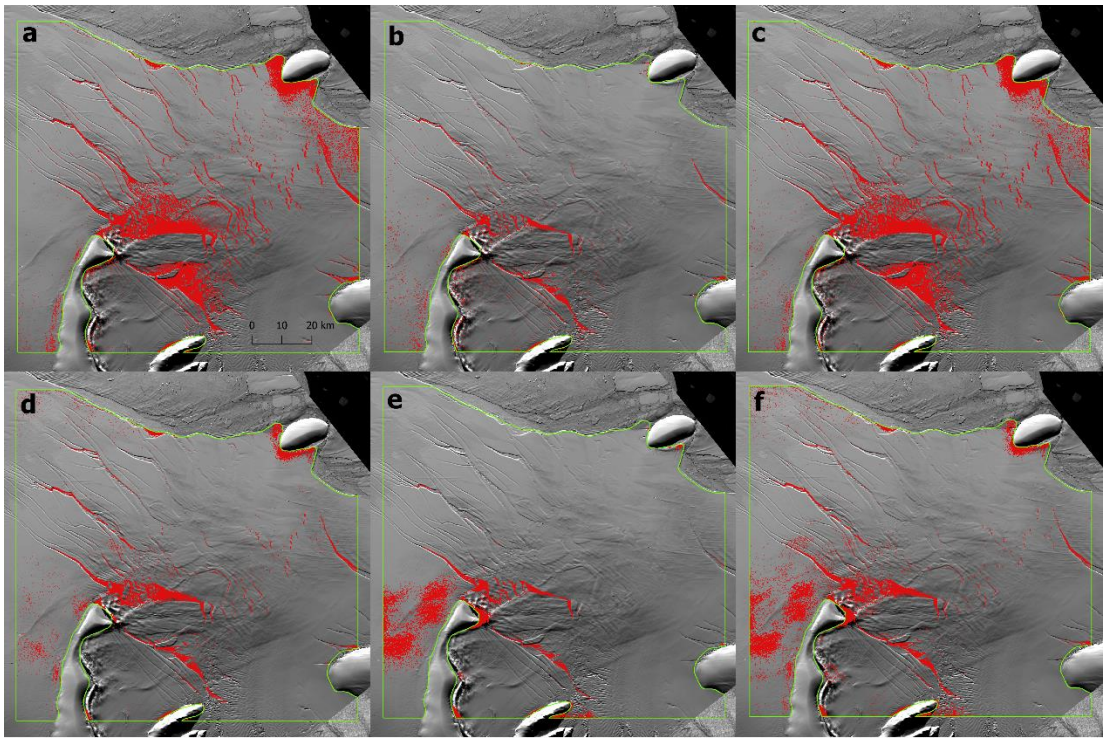

Figure 25. *Pixel-based classifications for* ***(a)*** *L-bands freeze,* ***(b)*** *C-bands freeze,* ***(c)*** *C+L-bands freeze, (****d****) L-bands melt,* ***(e)*** *C-bands melt, and* ***(f)*** *C+L-bands melt. Classified rifts shown in red. Background image is Landsat 8 panchromatic band from 30 August 2020.*

Pixel-based classifications tend to classify features at a higher spatial resolution compared to object-based classification. However, the spectral similarity between MFR and F, and OWR and surface melt suggests that pixel-based classifiers will struggle to separate these features; this was found to be true, as all pixel-based classifications tested did not reliably identify large, mélange-filled rifts or small fractures. The performance of pixel-based classifications improved significantly during freeze with many more rift edges identified, though mélange-filled rifts remained largely undetected (Figure 25a-c). During melt, only the darkest, deepest rifts were successfully identified (Figure 25d-f). Mélange-filled rifts were not identified with any of the configurations tested, though any inclusion of L-band (i.e., L-band or C+L-band) did slightly improve the detection of the rift edge. L-band also helps to prevent misclassification of large, dark regions of surface melt. In all cases, C-band classifications contained many more pixels/objects that were misclassified as rifts; the inclusion of L-band improves classification performance and reduce errors associated with surface melt and shadow.

6 Discussion

6.1 Scattering mechanisms influencing ice type separability

Throughout all seasons, open-water rifts appear as large, linear features with uniquely low backscatter due to signal loss and attenuation by ocean water within the interior of the rift. This makes the mean backscatter values for this class significantly lower than other classes, and the spread of values is greater. As a result, this class has high contrast and only a small proportion of its distribution overlaps with other classes; this means that open-water rifts are well separated during all seasons independent of sensor configuration. Wide, deep rifts are easily classified in all configurations; however, shallower or narrower rifts often blend into the surrounding environment, particularly in SAR imagery with considerable speckle noise. Firn and mélange-filled rifts are consistently difficult to separate because their mean values and distributions are very similar.

6.1.1 Freeze conditions

The LCIS is located below the dry snow line of the eastern AP (~700 m asl; Rau et al., 2000). The lack of melt events above this line creates a snowpack with small grain sizes and no internal ice layers; therefore, variations in backscatter in this region are largely controlled by variations in snow grain sizes. At lower elevations – such as around the GIR – combined with relatively low snow accumulation rates, create larger snow grains and rough, stratified ice layers within the snowpack (Rau et al., 2000). During late winter, scattering from dry snow and ice is dominated by volume scattering from snow/ice crystals or frozen inclusions within the snow (Rott & Matzler, 1987). L-band provides deeper penetration compared to C-band, allowing the signal to travel further through the firn layer and interact with the internal structure of the snow and ice. L-band is more sensitive to volume scattering from subsurface structures, while C-band experiences relatively higher rates of surface scattering; the greater sensitivity to volume scattering improves the discrimination of mélange-filled rifts from unfractured firn. The deeper interactions of these signals help discriminate between firn and mélange-filled rifts, as mélange-filled rifts contain various types of ice which exhibit different subsurface properties and a more complex scattering signal (Borstad et al., 2017; Larour et al., 2021), compared to the relatively homogeneous characteristics of unfractured ice. This heterogeneity also tends to depolarize the radar signal, thus

L_{HV} is particularly effective at distinguishing mélange-filled rifts from unfractured firn. During classification, SAR channels with greater sensitivity to volume scattering (i.e., L-band and HV polarization) consistently outperform those with sensitivity to surface scattering; this indicates that enhanced penetration into the volume also helps discriminate rifts and unfractured ice during classification.

6.1.2 Melt conditions

As the melt year progresses to late melt, firn densification reduces infiltration of surface meltwater produced by foehn winds at higher elevations (Luckman et al., 2014); this can be seen in the accumulation of melt ponds in northwestern inlets (e.g., Cabinet, Adie, and Mill) on the LCIS. These features appear as dark patches in SAR imagery and are likely responsible for much of the observed backscatter variability across the LCIS during melt (Rau et al., 2000; Luckman et al., 2014). While firn densification and the associated meltwater ponding is less common near the GIR, specular reflection from water and partially-thawed snow and ice dominates the scattering response of the ice surface. This is particularly true for the firn class, where the formation of meltwater pools, slush, and varying moisture levels across the ice shelf make the surface more heterogeneous. This results in highly variable γ^0 signatures, especially from channels that are sensitive to surface scattering (i.e., C-band, HH polarization); the use of these channels in classification often leads to many regions of unfractured ice misclassified as rifts. L-band remains superior for rift detection during late melt due to lower attenuation loss and reduced sensitivity to surface melt compared to C-band (Ulaby & Stiles, 1981); this allows for continued penetration depth and volume scattering contributions, even in the presence of liquid water. The contrast between classes during melt is higher with C-band, though separability is higher with L-band. This occurs as C-band experiences a more pronounced decrease in backscatter due to its greater sensitivity to wetness and roughness changes at the surface, while L-band is less affected by melt-induced changes in backscatter and is more sensitive to internal ice structures that enhance separability between firn and mélange-filled rifts. Additionally, the firn class undergoes a more uniform melt, resulting in a flatter water-covered surface that is a more effective specular reflector. This reduced roughness lowers the backscatter return from firn, causing γ^0 values to drop below those of mélange-filled rifts. As a result, negative contrast is observed between firn and mélange-filled rifts during late melt.

While HV polarization at both C- and L-band frequencies is ideal for distinguishing classes through volume scattering in winter, its effectiveness diminishes during melt. As the liquid water content of the ice increases, the surface is smoothed and water absorbs incident radar waves, reducing δ_p and increasing contributions from surface scattering (Rau et al., 2000). HH polarization is more sensitive to small-scale surface roughness changes; smooth, horizontal surfaces such as liquid water represent a deviation from the rougher volume scattering from snow grains and refrozen ice layers. This provides enhanced separation of firn and mélange-filled rifts during melt as firn surfaces appear smoother and darker in contrast to the rougher, brighter surfaces of rifts. This effect must be considered during classification as the change from L_{HV} to L_{HH} superiority indicates that rift visibility is dependent on polarization selection throughout the year.

6.1.3 Transitional seasons

At low elevations – such as around the GIR – percolating and subsequently refreezing meltwater, results in a higher radar return during transitional seasons (i.e., melt onset, early melt, freeze up) as the interaction between microwaves and internal ice layers causes the ice surface in this region to appear brighter in SAR imagery (Rott & Matzler, 1987). This likely contributes to the higher backscatter observed in mélange-filled rifts relative to unfractured firn, as these features display a high degree of internal variability and roughness. The creation of refrozen ice layers within the firn layer helps to separate rifts from unfractured ice and improve separability between firn and mélange-filled rifts. From late winter to early melt, the lack of C_{HH} contrast between firn and mélange-filled rifts occurs because these classes display considerable spectral similarity near the surface, i.e., where C-band signals interact most with the snow and firn. During early melt, the ice surface briefly refreezes and becomes rougher. Mélange-filled rifts experience an increase in γ^0 variability after refreezing, reflecting scattering variations within the mélange layer as new ice layers form and enhance the spectral heterogeneity of the rift interior (Rott & Matzler, 1987). This is detected more in C-band channels as this frequency is sensitive to shallow roughness changes, particularly in HH polarization; this can be observed through a greater change in mélange-filled rift γ^0 between melt onset to early melt with C_{HH} compared to C_{HV}. Similarly, the enhanced γ^0 variability increases the amount of overlap between mélange-filled rifts and firn γ^0, reducing scattering contrast between the two classes. The surface of the firn class tends to be more consistent in density and water content and forms a relatively homogeneous snow/firn layer during refreezing

compared to other classes; this minimizes internal scattering variability, leading to a lower variance in γ^0 when compared to mélange-filled rifts. Additionally, the scattering return from open-water rifts tends to be lower and the mélange layer is either absent or not as thick. This means this class is less affected by melting and refreezing cycles relative to mélange-filled rifts, as the signal return is already dominated by ocean water; in the event that a mélange layer exists within these features, any changes to the surface likely occur deep within the rift and may not be detected by the sensor.

During the freeze up season, snow and ice crystals begin to reform on the surface as the ice refreezes. The deep winter snowpack has not yet reformed, thus scattering during this season is dominated by volume scattering from glacier ice and a shallow snow layer. Dry snow and ice accommodate deeper penetration into the volume, thus enhancing the return from volume scattering effects and increasing γ^0 in both C- and L-band channels. These increases are more pronounced in C-band due partially to enhanced sensitivity to increasing surface roughness. Here, higher γ^0 is observed since dry snow and ice accommodate deeper penetration into the volume, thus enhancing the return from volume scattering effects. Configurations which have lower δ_p (i.e., C-band, HH polarization) are more sensitive to these changes as they experience enhanced interaction with shallow volume inhomogeneities which form during refreezing; L_{HV} does not experience such a pronounced increase in γ^0 since the signal penetrates further into the snow/ice volume and interaction with shallow inhomogeneities is reduced. Additionally, the more pronounced increase observed with C-band may also occur due to the larger increase in the spread of γ^0 values that occurred during late melt.

6.1.4 Impact of radiometric accuracy on separability

The γ^0 contrast between firn and mélange-filled rifts is often below the in-scene radiometric accuracy of the sensor (< 1 dB for Sentinel-1, < 0.5 dB for PALSAR-2 and SAOCOM) (Attema et al., 2005; Motohka et al., 2018; Recchia et al., 2022). Outside of the late melt season, L_{HV} is the only configuration with contrast values above ±0.5 dB, thus this configuration provides the most reliable ice type separability during these periods; alternatively, only L_{HH} exceeds contrast of ±0.5 dB during late melt and therefore provides the most reliable separability during this season. Given these results, the enhanced separability that occurs with L-band may be partially due to the higher

radiometric resolution of PALSAR-2 and SAOCOM, thus these sensors may provide improved separation of F and MFR when contrast between classes is low. In comparison, the contrast values between OWR and other classes are well above the radiometric accuracy of the sensors across all seasons; therefore, separability between these classes is likely unaffected by variations in radiometric accuracy.

6.2 Classification performance

The consistent difficulty in separating mélange-filled rifts from firn highlights the superiority of the OBIA detection technique. Pixel-based classifiers tend to treat each pixel independently, making them vulnerable to misclassification when features share similar backscatter characteristics. This results in many undetected rifts, especially narrow or shallow features, and misclassified regions of firn during widespread surface melt. Pixel-based classifications perform better during freeze conditions as the low γ^0 of rifts becomes more pronounced against the more uniform backdrop of dry snow and firn. However, the inability to classify mélange-filled rifts presents a significant limitation, as these features represent critical structural components of ice shelf rift systems. This compromises the accuracy of rift mapping and can lead to underestimation of the extent of the rift network. The reliance on radar backscatter for classification can lead to ambiguities, particularly in regions where surface conditions fluctuate due to melting and refreezing. Here, OBIA can significantly enhance rift detection relative to pixel-based methods due to their decreased reliance on backscatter values and the inclusion of contextual information. While the sensitivity of OBIA to sensor configuration is lower than in pixel-based approaches, frequency and polarization must still be selected to optimize rift visibility under varying surface conditions. Adding geometric and texture attributes to OBIA improves classification accuracy, especially when using SAR imagery and classifying features with unique spatial characteristics (Gao & Mas, 2008). GLCMs record how often a pixel with a certain grey level (intensity) is adjacent to another pixel with a different grey level; these attributes focus more on spatial relationships than absolute intensity values, therefore their inclusion in OBIA can help differentiate between classes that have overlapping pixel intensities (such as firn and mélange-filled rifts). GLCMs also increase the robustness of OBIA to SAR speckle noise, which tends to obscure class separability based on intensity values alone.

Through segmentation, OBIA techniques demonstrate a greater sensitivity to the geometric properties of rifts and can delineate rift edges more effectively. L-band presents an advantage over C-band by providing more meaningful object segmentation due to lower speckle noise and clearer delineation of the rift edge. This enhances the quality of the resulting objects and improves the subsequent image classification. Optical imagery is often used in object segmentation (Gao & Mas, 2008; Zhao et al., 2012; Wright & Polashenski, 2018; Zheng et al., 2024) as it tends to have more consistent textures and spectral values and smoother transitions between surfaces than SAR. Therefore, optical imagery can be very effective at producing clear object delineations, particularly for features such as rifts which display very pronounced linear geometry. Despite these advantages, optical data often does not reveal features such as mélange-filled rifts or buried/bridged fractures. Occasionally, a rift may originate at the ice shelf base, extending upward from a basal fracture and propagating towards the surface (van der Veen, 2002). In this case, optical imagery will not detect the fracture since it does not yet display surface-level expression. This indicates that optical data can complement, but not replace, SAR data for effective rift detection. Given the reliance on accurate segmentation for object-based classification, developing algorithms that can better handle speckle and enhance the delineation of rift features is critical. Here, combining L-band and optical imagery for segmentation is suggested to be the best practice for producing high quality objects prior to rift classification. Additionally, combining C- and L-band during the winter produces the best classification results, providing sufficient penetration of snow and ice mélange, and revealing bridged rifts and small fractures. This approach leverages the strengths of each sensor, allowing for accurate detection of both surface and subsurface features.

Surface melt and heavy shadowing reduces classification performance and causes frequent misclassification of unfractured ice as rifts; this effect is more prominent in pixel-based classification, though OBIA also experiences reduced performance in areas with variable topography (i.e., ice rumples) or extensive snow moisture. In both cases, the γ^0 of unfractured ice is reduced, more closely resembling the γ^0 signature of rifts. Dark shadows cast by topographic features can contribute to the development of erroneous rift objects by fostering the growth of segments in areas where they would not otherwise form. The region-growing process used in segmentation may further expand these objects, as shadowed regions often exhibit similar backscatter characteristics to rifts. In areas with heavy surface water ponding, rifts and fractures may be obscured entirely (Figure 26). This effect is more pronounced with C-band, as wet snow

affects the appearance of fractures more due to greater signal attenuation during melt, but also due to more significant snow moisture over the ice shelf during the Sentinel-1 scene date (Figure A2). As a result, rifts are obscured by surface melt more often and to a greater extent in Sentinel-1 imagery when compared to PALSAR-2. The effect of surface melt on rift detectability shows considerable spatial variability. Rifts around the GIR region of the LCIS are unlikely to be significantly obscured by heavy surface melt as ponding is concentrated around the northwestern inlets (Luckman et al., 2014). Melt in this region occurs only for approximately 25 days per year (Bevan et al., 2018), thus rift detection around GIR would not be impeded by drastic backscatter reductions for all but the most intense melt days. In contrast, rifts around the Bawden Ice Rise are frequently obscured by heavy surface melting for at least 75 days per year (Bevan et al., 2018). These differences suggest that the potential for accurate rift detection is dependent on seasonality and highly localized surface melt trends. The accuracy of object-based rift classifiers may also be improved by placing less emphasis on backscatter values and more on geometric attributes at different times of the year; increasing the weight of geometric attributes during melt conditions may produce a more capable classifier that reduces the misclassification of rifts and surface melt.

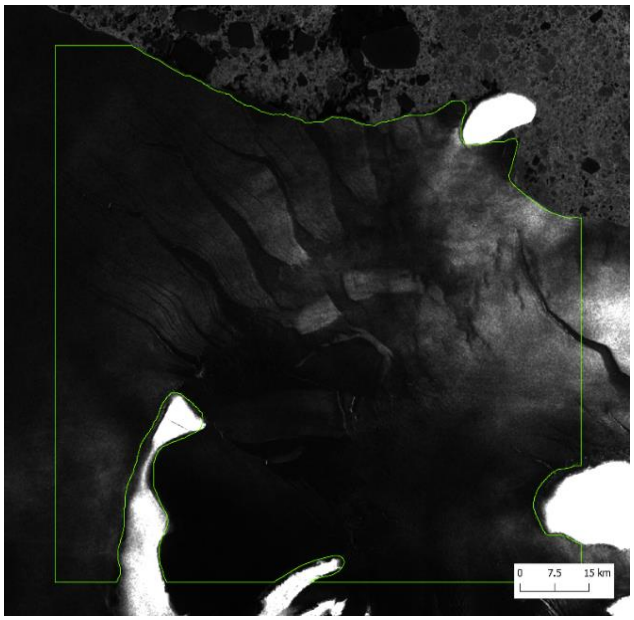

Figure 26. *Sentinel-1 HH image of Gipps Ice Rise region on 5 January 2021, three days before minimum ASCAT σ^0. Significant surface melt drastically darkens C-band SAR images during this time and obscures the location of rifts.*

It is important to note that the unfractured ice class is more prevalent throughout the image, which can lead to increased accuracy as most of the classification aligns with this class (Foody, 2020). The unfractured ice class generally has a higher accuracy than the rift class, but a

consistently lower κ; the higher κ value of the rift class suggests that the low overall accuracy is due to rifts being less dominant in the image. Therefore, it is assumed that the misclassification of rifts may be partially due to this effect and, as a result, may not be entirely related to differences in the performance of SAR parameters.

Rift geometry impacts classification performance because the backscatter from rifts varies greatly depending on their shape and size. Wide, deep rifts such as ROI #3 (Figure 17a) are always classified in the pixel- and object-based classifiers; these rifts have a unique backscatter signature and display sharp contrast with their surroundings, which makes them easier to classify correctly. However, classification is more prone to errors with decreasing rift depth since rifts with a thicker mélange layer have a larger scattering surface, thus more signal is returned from the interior of the rift and the backscatter signature more closely resembles firn/unfractured ice. Wide, shallow rifts (Figure 17b) are almost always identified to some degree, but the success of classification varies with frequency and surface conditions. With the pixel-based classifier, the interiors of these rifts are always misclassified as unfractured ice and the rift edge is only classified correctly during freeze conditions; alternatively, the edges and the interiors of the rifts are often classified correctly with the object-based classifier. Lastly, narrow, deep rifts are correctly classified at both C- and L-band frequency though their narrow tips are often missed during segmentation; this is particularly true for C-band due to speckle noise.

6.3 Comparison of sensor types for rift detection

The rift tip often represents the smallest and most difficult part of the rift to identify, yet its detection is crucial for monitoring rift propagation. High-resolution optical imagery proves advantageous towards this task, as the clarity provided by these images allows for precise discrimination of the rift tip. Other studies that have tracked the LC2017 rift using optical imagery have reported similar observations of rift propagation reported in Section 5.4 (Jansen et al., 2015; Borstad et al., 2017; Walker & Gardner, 2019). These studies report limitations in rift monitoring due to the low frequency of observations (Jansen et al., 2015) and the rift tip being obscured by snow bridges (Walker et al., 2013). SAR-based rift detection can alleviate these issues by providing all-year, all-weather imaging and penetration of surface snow to reveal buried fractures. This allows for a higher frequency of observations and detecting changes in rift geometry every

~1-3 days, as with Sentinel-1. L-band provides a particular advantage over other SAR frequencies by enabling the detection of rifts and discrimination of the rift tip deep below the surface during both dry and wet conditions. Upon applying L-band SAR to the detection of the LC2017 rift, results reveal that what appears to be the LC2017 rift was present on the LCIS up to 5 years after its formation in 2005 (Borstad et al., 2017), and at least 3 years prior to iceberg detachment. Through enhanced ice and snow penetration, L-band can reveal deep fractures and structural weaknesses that are invisible in both optical and C-band imagery; this is crucial for understanding how rifts may be propagating internally, and how this internal propagation aligns with the surface expression of the rift. This study shows that L-band may be capable of providing deeper insights into the structural integrity of ice shelves, allowing for predictions of iceberg calving events years prior to detachment.

SAR-based rift detection can be further improved with laser altimetry (i.e., ICESat-2). Elevation data adds crucial information to rift detection, especially in unfractured regions of the ice shelf that are darkened by surface melt or shadow; these regions occasionally display similar backscatter signatures to rifts, therefore altimetry can help prevent misclassification by verifying that there is no change in elevation and thus no fracture exists. Laser altimetry can also guide training site selection by validating the location of fractures and helping to characterize their morphology. Supplementing SAR-based rift detection with high resolution laser altimetry or elevation data can therefore enhance the detection of rifts and help contextualize rift development relative to ice mélange thickness and the presence or absence of suture zones.

6.4 Impact of speckle

Speckle noise has a significant impact on SAR-based classification by controlling the image quality and defining the size and shape of features that can be classified. Speckle filtering must be performed before image classification, as the performance of both pixel- and object-based classifiers is reduced by noise. The choice in speckle filter contributes to the success of classification by controlling spatial resolution and the sharpness of features in the image. In pixel-based classification, speckle affects pixel intensity values which makes it challenging to distinguish between classes that have subtle differences in backscatter; applying speckle filtering enhances the separation of all polarization channels and significantly improves classification

accuracy (Lee et al., 1999; Dasari et al., 2015). OBIA is less affected by this issue due to the decreased reliance on pixel intensity, though speckle noise influences the segmentation stage of OBIA by affecting the shape of segmented objects and may result in extreme over-segmentation (producing too many small segments) when no filter is applied (Morandeira et al., 2016). Furthermore, the choice in speckle filter affects the performance of the segmentation stage as some filters are superior at edge preservation. For this study, the median filter was chosen as it performs better than mean filters at preserving texture information and edges between features (Lee et al., 1994; Qiu et al., 2004). More advanced edge-preserving speckle filters have been developed specifically for SAR-based segmentation (Shamsoddini & Trinder, 2011; Morandeira et al., 2016; Meester & Baslamisli, 2022; Parhad et al., 2023); these may be a good option for future segmentation and object-based rift classifications, particularly with C-band SAR.

C-band frequency is more sensitive to small surface roughness through its shorter wavelength relative to L-band. Therefore, C-band typically experiences greater speckle noise; this tends to obscure rifts more in C-band images, especially when the fracture width is smaller than a few hundred meters. In these cases, rifts may not have enough backscatter contrast to stand out against the highly variable background, resulting in features becoming blurred or merged with the surrounding noise. This makes it difficult to identify fractures since segmentation algorithms search for contiguous, homogeneous areas to grow a region and rely on the contrast between features to delineate an edge. The main result of this is that speckle noise patterns may be identified as false edges (Meester & Baslamisli, 2022). When segmenting SAR images, noise introduces abrupt intensity changes that can cause the algorithm to over-segment (Delves et al., 1992; Morandiera et al., 2016). This was particularly the case for Sentinel-1 segmentation, where the presence of speckle caused over-segmentation with a low scale parameter (small objects); with a high scale parameter (large objects), under-segmentation was observed as the algorithm frequently merged dissimilar regions and struggled to delineate one or both edges of a fracture. To overcome this and attempt to optimize C-band for image segmentation, efforts were taken to further reduce speckle by increasing the filter window, but this resulted in significant loss of resolution and erasure of smaller fractures from the image. Overall, PALSAR-2 has a more homogeneous texture compared to Sentinel-1 with less speckle noise, thus rifts have greater contrast with their surroundings and segmentation produces objects that better delineate the rift edge. This must be considered when choosing frequencies to use in segmentation and classification; based on the

examined segmentation parameters and inputs bands used in this study, C-band is less likely to produce meaningful image objects and therefore rift classification will be less successful.

6.5 Impact of viewing geometry

One important consideration on the limitations of satellite-based rift detection using is the effect of different viewing geometries (i.e., θ, sensor look direction) on fracture visibility. θ for class samples were all within the mid- (30-40°) to far-range (40-50+°); samples retrieved from Sentinel-1 were more consistently in the mid-range, while PALSAR-2 and SAOCOM samples were more in the far-range. No θ dependence was observed for the examined study sites, though samples fell within a narrow θ range. Nevertheless, the difference in θ range between C- and L-band sensors in this study may contribute to the observed difference in rift visibility. θ may impact rift visibility by controlling δ_p, feature contrast, and shadowing at the rift wall; lower θ is typically associated with greater δ_p and greater contrast between fractures and the surrounding ice (Marsh et al., 2021). Using this rationale, enhanced rift visibility would be expected in the C-band scenes, but the opposite is observed. While incidence angle effects on δ_p and feature contrast may not be significant enough to stand out against variations in rift visibility due to frequency or polarization, they may still play a role. In cases where volume scattering contributions are significant, dry snow will show a weaker dependence on θ (Rees, 2012); as a result, L-band may be more resistant to θ effects than C-band during dry snow conditions. This study used scenes from both ascending and descending orbits. While it is generally not recommended to combine data from different orbits in time series analyses, differences that may arise due to sensor orientation are expected to be minimal due to the relatively flat terrain of ice shelves. While there is no apparent pattern in class separability between scenes with different orbits, the look direction of the sensor appears to have an impact on the segmentation process. Radar foreshortening creates a line of high backscatter at the edges of larger rifts that are oriented towards the sensor look direction; during segmentation, this line produces narrow, elongated objects that are shaped like rifts, but with much higher backscatter values. These features will often be misclassified in OBIA techniques if too much weight is placed on geometric or shape attributes, as they will fail to capture the difference in backscatter intensity between dark elongated objects (rifts) and bright elongated objects (rift edge). Incidence angle effects may also be limited to differences in rift geometry. Large, open fractures are unlikely to be affected by θ differences as they provide a strong scattering surface even in sub-

optimal imaging conditions, while small unbridged rifts and thin cracks may be more sensitive to viewing geometry.

7 Conclusions

This analysis demonstrates the superiority of L-band frequency when applied to SAR-based rift detection. Rifts are more contrasted against surrounding snow in L-band SAR imagery when compared to C-band. Additionally, rifts are more reliably detected using machine learning-based detection techniques which include L-band in classification. Longer wavelength L-band penetrates deeper into the firn layer to provide enhanced separability between fractured and unfractured ice shelf surfaces throughout the entire melt year. Deep rifts with a thin or absent mélange layer have very low backscatter and are easily distinguishable from the surrounding firn in both visual inspection and automated classification, independent of SAR frequency or polarization; in contrast, rifts with a thick mélange layer are consistently difficult to identify. The deeper penetration depth of L-band provides an advantage to rift detection by enhancing the separability of mélange-filled rifts during both freeze and melt conditions. Furthermore, the use of both HH and HV polarizations enhances the detection of rifts across seasonal conditions due to the varying effectiveness of each polarization under different melt conditions. The unique transition to HH polarization for optimal mélange-filled rift separability during late melt suggests that seasonal changes in surface characteristics play a role in the performance of rift detection techniques. Polarization selection must therefore consider local surface melt conditions to improve the detection of bridged rifts. L-band is advantageous here as well, as its resilience to surface melt can be particularly useful in rapidly changing environments where melt dynamics are prominent.

These results highlight challenges in detecting rifts filled with mélange, as these features often blend in with the surrounding unfractured ice and firn due to their similar backscatter signatures. While pixel-based classification approaches struggle with separability and misclassification due to spectral similarities and SAR speckle noise, object-based classification provides a more robust solution, albeit contingent on effective segmentation. By adding geometric information to the classification and considering the spatial context of features, the OBIA approach may help reduce the dependence of fracture detection on feature/acquisition geometry that occurs

with SAR backscatter techniques. Additionally, fracture geometry and orientation must be considered, as detection is limited to the shape and size of fractures relative to the SAR viewing geometry and sensor resolution. Future work on understanding the constraints of SAR system parameters on rift detection is needed before high-quality rift classifiers can be implemented into routine observations and process studies related to ice sheet stability.

Understanding the strengths and limitations of each classification approach, especially in the context of ice type and fracture characteristics, is crucial for developing accurate rift detection techniques. Optimizing the full potential of both C- and L-band SAR and developing object-based machine learning techniques which integrate multiple remote sensing technologies, will lay the groundwork for future automated rift detection and calving studies. Developing these techniques will allow for the implementation of a standardized detection method which leverages the most widely available data with high temporal resolution. The methods outlined above offer promising avenues for improving the monitoring of rifts and their implications for fracture development and ice shelf calving dynamics. Accurately detecting rifts will aid in locating the orientation and distribution of stresses within an ice shelf, therefore improving predictions of rift propagation and iceberg calving, and future ice shelf collapse.

References

Agrawal, S., & Khairnar, G. B. (2019). A comparative assessment of remote sensing imaging techniques: Optical, SAR, and LiDAR. *The International Archives of the Photogrammetry, Remote Sensing and Spatial Information Sciences*, *XLII-5/W3*, 1–6. doi: 10.5194/isprs-archives-XLII-5-W3-1-2019

Alley, K. E., Scambos, T. A., Alley, R. B., & Holschuh, N. (2019). Troughs developed in ice-stream shear margins precondition ice shelves for ocean-driven breakup. *Science Advances*, *5*(10), eaax2215. doi: 10.1126/sciadv.aax2215

Alley, K. E., Scambos, T. A., & Alley, R. B. (2022). The role of channelized basal melt in ice-shelf stability: Recent progress and future priorities. *Annals of Glaciology*, *63*(87–89), 18–22. doi: 10.1017/aog.2023.5

Andreasen, J. R., Hogg, A. E., & Selley, H. L. (2023). Change in Antarctic ice shelf area from 2009 to 2019. *The Cryosphere*, *17*(5), 2059–2072. doi: 10.5194/tc-17-2059-2023

Arcone, S. A., Lever, J. H., Ray, L. E., Walker, B. S., Hamilton, G., & Kaluzienski, L. (2016). Ground-penetrating radar profiles of the McMurdo Shear Zone, Antarctica, acquired with an unmanned rover: Interpretation of crevasses, fractures, and folds within firn and marine ice. *Geophysics*, *81*(1), WA21–WA34. doi: 10.1190/geo2015-0132.1

Arndt, S., & Haas, C. (2019). Spatiotemporal variability and decadal trends of snowmelt processes on Antarctic sea ice observed by satellite scatterometers. *The Cryosphere*, *13*(7), 1943–1958. doi: 10.5194/tc-13-1943-2019

Arnold, E., Leuschen, C., Rodriguez-Morales, F., Li, J., Paden, J., et al. (2020). CReSIS airborne radars and platforms for ice and snow sounding. *Annals of Glaciology*, *61*(81), 58–67. doi: 10.1017/aog.2019.37

Ashcraft, I. S., & Long, D. G. (2006). Comparison of methods for melt detection over Greenland using active and passive microwave measurements. *International Journal of Remote Sensing*, *27*(12), 2469–2488. doi: 10.1080/01431160500534465

Attema, E., Bargellini, P., Edwards, P., Levrini, G., Lokas, S., et al. (2005). Sentinel-1: The Radar Mission for GMES Operational Land and Sea Services. *Esa Bulletin*.

Banwell, A. F., MacAyeal, D. R., & Sergienko, O. V. (2013). Breakup of the Larsen B Ice Shelf triggered by chain reaction drainage of supraglacial lakes. *Geophysical Research Letters*, *40*(22), 5872–5876. doi: 10.1002/2013GL057694

Banwell, A. F., Willis, I. C., Macdonald, G. J., Goodsell, B., Mayer, D. P., et al. (2017). Calving and rifting on the McMurdo Ice Shelf, Antarctica. *Annals of Glaciology*, *58*(75pt1), 78–87. doi: 10.1017/aog.2017.12

Barrand, N. E., Vaughan, D. G., Steiner, N., Tedesco, M., Kuipers Munneke, P., et al. (2013). Trends in Antarctic Peninsula surface melting conditions from observations and regional climate modeling. *Journal of Geophysical Research: Earth Surface*, *118*(1), 315–330. doi: 10.1029/2012JF002559

Barry, R. G., & Gan, T. Y. (2022). *The Global Cryosphere: Past, Present, and Future*. Cambridge University Press.

Bassis, J. N., Coleman, R., Fricker, H. A., & Minster, J. B. (2005). Episodic propagation of a rift on the Amery Ice Shelf, East Antarctica. *Geophysical Research Letters*, *32*(6). doi: 10.1029/2004GL022048

Bassis, J. N., & Jacobs, S. (2013). Diverse calving patterns linked to glacier geometry. *Nature Geoscience*, *6*(10), 833–836. doi: 10.1038/ngeo1887

Bassis, J. N., & Walker, C. C. (2012). Upper and lower limits on the stability of calving glaciers from the yield strength envelope of ice. *Proceedings of the Royal Society A: Mathematical, Physical and Engineering Sciences*. (world). doi: 10.1098/rspa.2011.0422

Bassis, J. N., Crawford, A., Kachuck, S. B., Benn, D. I., Walker, C., et al. (2024). Stability of Ice Shelves and Ice Cliffs in a Changing Climate. *Annual Review of Earth and Planetary Sciences*, *52*(Volume 52, 2024), 221–247. doi: 10.1146/annurev-earth-040522-122817

Bassis, J. N., Fricker, H. A., Coleman, R., & Minster, J.-B. (2008). An investigation into the forces that drive ice-shelf rift propagation on the Amery Ice Shelf, East Antarctica. *Journal of Glaciology*, *54*(184), 17–27. doi: 10.3189/002214308784409116

Baumhoer, C. (2020). *Glacier Front Dynamics of Antarctica-Analysing Changes in Glacier and Ice Shelf Front Position based on SAR Time Series*. Julius-Maximilians-Universität Würzburg.

Baumhoer, C. A., Dietz, A. J., Dech, S., & Kuenzer, C. (2018). Remote sensing of Antarctic glacier and ice-shelf front dynamics—A review. *Remote Sensing*, *10*(9), 1445. doi: 10.3390/rs10091445

Bell, R. E., Banwell, A. F., Trusel, L. D., & Kingslake, J. (2018). Antarctic surface hydrology and impacts on ice-sheet mass balance. *Nature Climate Change 2018 8:12*, *8*(12), 1044–1052. doi: 10.1038/s41558-018-0326-3

Bell, R. E., & Seroussi, H. (2020). History, mass loss, structure, and dynamic behavior of the Antarctic Ice Sheet. *Science*, *367*(6484), 1321–1325. doi: 10.1126/science.aaz5489

Benn, D. I., & Åström, J. A. (2018). Calving glaciers and ice shelves. *Advances in Physics: X*, *3*(1), 1513819. doi: 10.1080/23746149.2018.1513819

Benn, D. I., Warren, C. R., & Mottram, R. H. (2007). Calving processes and the dynamics of calving glaciers. *Earth-Science Reviews*, *82*(3), 143–179. doi: 10.1016/j.earscirev.2007.02.002

Berg, B., & Bassis, J. (2022). Crevasse advection increases glacier calving. *Journal of Glaciology*, *68*(271), 977–986. doi: 10.1017/jog.2022.10

Bevan, S. L., Luckman, A. J., Kuipers Munneke, P., Hubbard, B., Kulessa, B., & Ashmore, D. W. (2018). Decline in Surface Melt Duration on Larsen C Ice Shelf Revealed by The Advanced Scatterometer (ASCAT). *Earth and Space Science*, *5*(10), 578–591. doi: 10.1029/2018EA000421

Bhardwaj, A., Sam, L., Singh, S., & Kumar, R. (2016). Automated detection and temporal monitoring of crevasses using remote sensing and their implications for glacier dynamics. *Annals of Glaciology*, *57*(71), 81–91. doi: 10.3189/2016AoG71A496

Bintanja, R., van Oldenborgh, G. J., Drijfhout, S. S., Wouters, B., & Katsman, C. A. (2013). Important role for ocean warming and increased ice-shelf melt in Antarctic sea-ice expansion. *Nature Geoscience*, *6*(5), 376–379. doi: 10.1038/ngeo1767

Blaschke, T. (2010). Object based image analysis for remote sensing. *ISPRS Journal of Photogrammetry and Remote Sensing*, *65*(1), 2–16. doi: 10.1016/j.isprsjprs.2009.06.004

Blaschke, T., Hay, G. J., Kelly, M., Lang, S., Hofmann, P., et al. (2014). Geographic Object-Based Image Analysis – Towards a new paradigm. *ISPRS Journal of Photogrammetry and Remote Sensing*, *87*, 180–191. doi: 10.1016/j.isprsjprs.2013.09.014

Borstad, C., McGrath, D., & Pope, A. (2017). Fracture propagation and stability of ice shelves governed by ice shelf heterogeneity. *Geophysical Research Letters*, *44*(9), 4186–4194. doi: 10.1002/2017GL072648

Breiman, L. (2001). Random Forests. *Machine Learning*, *45*(1), 5–32. doi: 10.1023/A:1010933404324

Breivik, L. A., Eastwood, S., & Lavergne, T. (2012). Use of C-Band Scatterometer for Sea Ice Edge Identification. *IEEE Transactions on Geoscience and Remote Sensing*, *50*(7), 2669–2677. doi: 10.1109/TGRS.2012.2188898

Brock, B. C. (2010). *On the detection of crevasses in glacial ice with synthetic-aperture radar.* (No. SAND2010-0363). Sandia National Laboratories (SNL), Albuquerque, NM, and Livermore, CA (United States). doi: 10.2172/989382

Bromwich, D. H., Nicolas, J. P., Monaghan, A. J., Lazzara, M. A., Keller, L. M., et al. (2012). Central West Antarctica among the most rapidly warming regions on Earth. *Nature Geoscience*, *6*(2), 139–145. doi: 10.1038/ngeo1671

CATALYST Earth. (n.d.). *Object Analyst Module Description*.

Committee on Earth Observation Satellites (CEOS). (2021). *CARD4L: Normalized Radar Backscatter Product Specification*.

Committee on Earth Observation Satellites (CEOS). (2020). *CARD4L: Surface Reflectance Product Specification*.

Casey, J. A., Howell, S. E. L., Tivy, A., & Haas, C. (2016). Separability of sea ice types from wide swath C- and L-band synthetic aperture radar imagery acquired during the melt season. *Remote Sensing of Environment*, *174*, 314–328. doi: 10.1016/j.rse.2015.12.021

Christie, F. D. W., Benham, T. J., Batchelor, C. L., Rack, W., Montelli, A., & Dowdeswell, J. A. (2022). Antarctic ice-shelf advance driven by anomalous atmospheric and sea-ice circulation. *Nature Geoscience*, *15*(5), 356–362. doi: 10.1038/s41561-022-00938-x

Colgan, W., Rajaram, H., Abdalati, W., McCutchan, C., Mottram, R., et al. (2016). Glacier crevasses: Observations, models, and mass balance implications. *Reviews of Geophysics*, *54*(1), 119–161. doi: 10.1002/2015RG000504

Convey, P., Bindschadler, R., Di Prisco, G., Fahrbach, E., Gutt, J., et al. (2009). Antarctic climate change and the environment. *Antarctic Science*, *21*(6), 541–563. doi: 10.1017/S0954102009990642

Cook, A. J., & Vaughan, D. G. (2010). Overview of areal changes of the ice shelves on the Antarctic Peninsula over the past 50 years. *The Cryosphere*.

Craven, M., Allison, I., Fricker, H. A., & Warner, R. (2009). Properties of a marine ice layer under the Amery Ice Shelf, East Antarctica. *Journal of Glaciology*, *55*(192), 717–728. doi: 10.3189/002214309789470941

Dasari, K., Anjaneyulu, L., Jayasri, P. V., & Prasad, A. V. V. (2015). Importance of speckle filtering in image classification of SAR data. *2015 International Conference on Microwave, Optical and Communication Engineering (ICMOCE)*, 349–352. doi: 10.1109/ICMOCE.2015.7489764

de Lavergne, C., Madec, G., Roquet, F., Holmes, R. M., & McDougall, T. J. (2017). Abyssal ocean overturning shaped by seafloor distribution. *Nature*, *551*(7679), 181–186. doi: 10.1038/nature24472

de Roda Husman, S., Hu, Z., Wouters, B., Kuipers Munneke, P., Veldhuijsen, S., & Lhermitte, S. (2023). Remote Sensing of Surface Melt on Antarctica: Opportunities and Challenges. *IEEE Journal of Selected Topics in Applied Earth Observations and Remote Sensing*, *16*, 2462–2480. doi: 10.1109/JSTARS.2022.3216953

De Rydt, J., Gudmundsson, G., Nagler, T., Wuite, J., & King, E. (2018). Recent rift formation and impact on the structural integrity of the Brunt Ice Shelf, East Antarctica. *The Cryosphere*, *12*, 505–520. doi: 10.5194/tc-12-505-2018

DeConto, R. M., & Pollard, D. (2016). Contribution of Antarctica to past and future sea-level rise. *Nature*, *531*(7596), 591–597. doi: 10.1038/nature17145

Delves, L. M., Wilkinson, R., Oliver, C. J., & White, R. G. (1992). Comparing the performance of SAR image segmentation algorithms. *International Journal of Remote Sensing*, *13*(11), 2121–2149. doi: 10.1080/01431169208904257

Depoorter, M. A., Bamber, J. L., Griggs, J. A., Lenaerts, J. T. M., Ligtenberg, S. R. M., et al. (2013). Calving fluxes and basal melt rates of Antarctic ice shelves. *Nature*, *502*(7469), 89–92. doi: 10.1038/nature12567

Dietz, A. J., Kuenzer, C., Gessner, U., & Dech, S. (2012). Remote sensing of snow – a review of available methods. *International Journal of Remote Sensing*, *33*(13), 4094–4134. doi: 10.1080/01431161.2011.640964

Doake, C. S. M., Corr, H. F. J., Rott, H., Skvarca, P., & Young, N. W. (1998). Breakup and conditions for stability of the northern Larsen Ice Shelf, Antarctica. *Nature*, *391*(6669), 778–780. doi: 10.1038/35832

Dodge, Y. (2003). *The Oxford Dictionary of Statistical Terms*. Oxford University Press.

Drucker, R., Martin, S., & Kwok, R. (2011). Sea ice production and export from coastal polynyas in the Weddell and Ross Seas. *Geophysical Research Letters*, *38*(17). doi: 10.1029/2011GL048668

Early, D. S., & Long, D. G. (2001). Image reconstruction and enhanced resolution imaging from irregular samples. *IEEE Transactions on Geoscience and Remote Sensing*, *39*(2), 291–302. doi: 10.1109/36.905237

Eayrs, C., Li, X., Raphael, M. N., & Holland, D. M. (2021). Rapid decline in Antarctic sea ice in recent years hints at future change. *Nature Geoscience*, *14*(7), 460–464. doi: 10.1038/s41561-021-00768-3

Favier, V., Krinner, G., Amory, C., Gallée, H., Beaumet, J., & Agosta, C. (2017). Antarctica-Regional Climate and Surface Mass Budget. *Current Climate Change Reports*, *3*(4), 303–315. doi: 10.1007/s40641-017-0072-z

Fogt, R. L., & Marshall, G. J. (2020). The Southern Annular Mode: Variability, trends, and climate impacts across the Southern Hemisphere. *WIREs Climate Change*, *11*(4), e652. doi: 10.1002/wcc.652

Foody, G. M. (2020). Explaining the unsuitability of the kappa coefficient in the assessment and comparison of the accuracy of thematic maps obtained by image classification. *Remote Sensing of Environment*, *239*, 111630. doi: 10.1016/j.rse.2019.111630

Fowler, A., & Ng, F. (Eds.). (2021). *Glaciers and Ice Sheets in the Climate System*. Cham: Springer International Publishing. doi: 10.1007/978-3-030-42584-5

Fox, A. J., Paul, A., & Cooper, R. (1994). Measured properties of the Antarctic ice sheet derived from the SCAR Antarctic digital database. *Polar Record*, *30*(174), 201–206. doi: 10.1017/S0032247400024268

Francis, D., Fonseca, R., Mattingly, K. S., Marsh, O. J., Lhermitte, S., & Cherif, C. (2022). Atmospheric Triggers of the Brunt Ice Shelf Calving in February 2021. *Journal of Geophysical Research: Atmospheres*, *127*(11), e2021JD036424. doi: 10.1029/2021JD036424

Fretwell, P., Pritchard, H. D., Vaughan, D. G., Bamber, J. L., Barrand, N. E., et al. (2013). Bedmap2: Improved ice bed, surface and thickness datasets for Antarctica. *The Cryosphere*, *7*(1), 375–393. doi: 10.5194/tc-7-375-2013

Fricker, H. A., Young, N. W., Coleman, R., Bassis, J. N., & Minster, J.-B. (2005). Multi-year monitoring of rift propagation on the Amery Ice Shelf, East Antarctica. *Geophysical Research Letters*, *32*(2). doi: 10.1029/2004GL021036

Fürst, J. J., Durand, G., Gillet-Chaulet, F., Tavard, L., Rankl, M., et al. (2016). The safety band of Antarctic ice shelves. *Nature Climate Change*, *6*(5), 479–482. doi: 10.1038/nclimate2912

Gao, J., & Liu, Y. (2016). Applications of remote sensing, GIS and GPS in glaciology: A review. *Progress in Physical Geography*, *25*(4), 520–540. doi: 10.1177/030913330102500404

Gao, Y., & Mas, J. F. (2008). *A comparison of the performance of pixel-based and object-based classifications over images with various spatial resolutions*.

Gardner, A. S., Moholdt, G., Scambos, T., Fahnstock, M., Ligtenberg, S., et al. (2018). Increased West Antarctic and unchanged East Antarctic ice discharge over the last 7 years. *The Cryosphere*, *12*(2), 521–547. doi: 10.5194/tc-12-521-2018

Glasser, N. F., Kulessa, B., Luckman, A., Jansen, D., King, E. C., et al. (2009). Surface structure and stability of the Larsen C ice shelf, Antarctic Peninsula. *Journal of Glaciology*, *55*(191), 400–410. doi: 10.3189/002214309788816597

Grosvenor, D. P., King, J. C., Choularton, T. W., & Lachlan-Cope, T. (2014). Downslope föhn winds over the Antarctic Peninsula and their effect on the Larsen ice shelves. *Atmospheric Chemistry and Physics*, *14*(18), 9481–9509. doi: 10.5194/acp-14-9481-2014

Hall, D. (2012). *Remote Sensing of Ice and Snow*. Springer Science & Business Media.

Hanna, E., Navarro, F. J., Pattyn, F., Domingues, C. M., Fettweis, X., et al. (2013). Ice-sheet mass balance and climate change. *Nature*, *498*(7452), 51–59. doi: 10.1038/nature12238

Hattermann, T., Nicholls, K. W., Hellmer, H. H., Davis, P. E. D., Janout, M. A., et al. (2021). Observed interannual changes beneath Filchner-Ronne Ice Shelf linked to large-scale atmospheric circulation. *Nature Communications*, *12*(1), 2961. doi: 10.1038/s41467-021-23131-x

He, L.-Y., Ke, C.-Q., Zhou, X., Cui, Y.-N., & Shan, L. (2016). Antarctic sea ice change based on a new sea ice dataset from 1992 to 2008. *Climate Research*, *71*(2), 155–169. doi: 10.3354/cr01436

Hogg, A. E., & Gudmundsson, G. H. (2017). Impacts of the Larsen-C Ice Shelf calving event. *Nature Climate Change*, *7*(8), 540–542. doi: 10.1038/nclimate3359

Holland, P. R., Corr, H. F. J., Pritchard, H. D., Vaughan, D. G., Arthern, R. J., et al. (2011). The air content of Larsen Ice Shelf. *Geophysical Research Letters*, *38*(10). doi: 10.1029/2011GL047245

Holland, P. R., Corr, H. F. J., Vaughan, D. G., Jenkins, A., & Skvarca, P. (2009). Marine ice in Larsen Ice Shelf. *Geophysical Research Letters*, *36*(11). doi: 10.1029/2009GL038162

Hossain, M. D., & Chen, D. (2019). Segmentation for Object-Based Image Analysis (OBIA): A review of algorithms and challenges from remote sensing perspective. *ISPRS Journal of Photogrammetry and Remote Sensing*, *150*, 115–134. doi: 10.1016/j.isprsjprs.2019.02.009

Hubbard, B., Luckman, A., Ashmore, D. W., Bevan, S., Kulessa, B., et al. (2016). Massive subsurface ice formed by refreezing of ice-shelf melt ponds. *Nature Communications*, *7*(1), 11897. doi: 10.1038/ncomms11897

Hulbe, C. L., LeDoux, C., & Cruikshank, K. (2010). Propagation of long fractures in the Ronne Ice Shelf, Antarctica, investigated using a numerical model of fracture propagation. *Journal of Glaciology*, *56*(197), 459–472. doi: 10.3189/002214310792447743

IMBIE. (2018). Mass balance of the Antarctic Ice Sheet from 1992 to 2017. *Nature*, *558*(7709), 219–222. doi: 10.1038/s41586-018-0179-y

Jacobs, S. S. (2004). Bottom water production and its links with the thermohaline circulation. *Antarctic Science*, *16*(4), 427–437. doi: 10.1017/S095410200400224X

Janiesch, C., Zschech, P., & Heinrich, K. (2021). Machine learning and deep learning. *Electronic Markets*, *31*(3), 685–695. doi: 10.1007/s12525-021-00475-2

Jansen, D., Luckman, A. J., Cook, A., Bevan, S., Kulessa, B., et al. (2015). Brief Communication: Newly developing rift in Larsen C Ice Shelf presents significant risk to stability. *The Cryosphere*, *9*(3), 1223–1227. doi: 10.5194/tc-9-1223-2015

Jansen, D., Luckman, A., Kulessa, B., Holland, P. R., & King, E. C. (2013). Marine ice formation in a suture zone on the Larsen C Ice Shelf and its influence on ice shelf dynamics. *Journal of Geophysical Research: Earth Surface*, *118*(3), 1628–1640. doi: 10.1002/jgrf.20120

Jeong, S., Howat, I. M., & Bassis, J. N. (2016). Accelerated ice shelf rifting and retreat at Pine Island Glacier, West Antarctica. *Geophysical Research Letters*, *43*(22), 11,720-11,725. doi: 10.1002/2016GL071360

Johnson, A., Fahnestock, M., & Hock, R. (2020). Evaluation of passive microwave melt detection methods on Antarctic Peninsula ice shelves using time series of Sentinel-1 SAR. *Remote Sensing of Environment*, *250*, 112044. doi: 10.1016/j.rse.2020.112044

Joughin, I., & MacAyeal, D. R. (2005). Calving of large tabular icebergs from ice shelf rift systems. *Geophysical Research Letters*, *32*(2). doi: 10.1029/2004GL020978

Joughin, I., Smith, B. E., & Abdalati, W. (2010). Glaciological advances made with interferometric synthetic aperture radar. *Journal of Glaciology*, *56*(200), 1026–1042. doi: 10.3189/002214311796406158

Kacimi, S., & Kwok, R. (2022). Arctic Snow Depth, Ice Thickness, and Volume From ICESat-2 and CryoSat-2: 2018–2021. *Geophysical Research Letters*, *49*(5), e2021GL097448. doi: 10.1029/2021GL097448

Kuipers Munneke, P, Ligtenberg, S. R. M., Broeke, M. R. V. D., & Vaughan, D. G. (2014). Firn air depletion as a precursor of Antarctic ice-shelf collapse. *Journal of Glaciology*, *60*(220), 205–214. doi: 10.3189/2014JoG13J183

Kuipers Munneke, P., Luckman, A. J., Bevan, S. L., Smeets, C. J. P. P., Gilbert, E., et al. (2018). Intense Winter Surface Melt on an Antarctic Ice Shelf. *Geophysical Research Letters*, *45*(15), 7615–7623. doi: 10.1029/2018GL077899

Kulessa, B., Booth, A. D., O'Leary, M., McGrath, D., King, E. C., et al. (2019). Seawater softening of suture zones inhibits fracture propagation in Antarctic ice shelves. *Nature Communications*, *10*(1), 5491. doi: 10.1038/s41467-019-13539-x

Kulessa, B., Jansen, D., Luckman, A. J., King, E. C., & Sammonds, P. R. (2014). Marine ice regulates the future stability of a large Antarctic ice shelf. *Nature Communications*, *5*(1), 3707. doi: 10.1038/ncomms4707

Lai, C.-Y., Kingslake, J., Wearing, M. G., Chen, P.-H. C., Gentine, P., et al. (2020). Vulnerability of Antarctica's ice shelves to meltwater-driven fracture. *Nature*, *584*(7822), 574–578. doi: 10.1038/s41586-020-2627-8

Larour, E., Rignot, E., Poinelli, M., & Scheuchl, B. (2021). Physical processes controlling the rifting of Larsen C Ice Shelf, Antarctica, prior to the calving of iceberg A68. *Proceedings of the National Academy of Sciences*, *118*(40), e2105080118. doi: 10.1073/pnas.2105080118

Larour, Eric, Rignot, E., & Aubry, D. (2004). Processes involved in the propagation of rifts near Hemmen Ice Rise, Ronne Ice Shelf, Antarctica. *Journal of Glaciology*, *50*(170), 329–341. doi: 10.3189/172756504781829837

Lee, J., Jurkevich, L., Dewaele, P., Wambacq, P., & Oosterlinck, A. (1994). Speckle filtering of synthetic aperture radar images: A Review. *Remote Sensing Reviews*, *8*. doi: 10.1080/02757259409532206

Lee, J.-S., Grunes, M. R., & de Grandi, G. (1999). Polarimetric SAR speckle filtering and its implication for classification. *IEEE Transactions on Geoscience and Remote Sensing*, *37*(5), 2363–2373. doi: 10.1109/36.789635

Lefebvre, W., Goosse, H., Timmermann, R., & Fichefet, T. (2004). Influence of the Southern Annular Mode on the sea ice–ocean system. *Journal of Geophysical Research: Oceans*, *109*(C9). doi: 10.1029/2004JC002403

Lenaerts, J. T. M., Lhermitte, S., Drews, R., Ligtenberg, S. R. M., Berger, S., et al. (2017). Meltwater produced by wind–albedo interaction stored in an East Antarctic ice shelf. *Nature Climate Change*, *7*(1), 58–62. doi: 10.1038/nclimate3180

Lenaerts, J. T. M., Medley, B., van den Broeke, M. R., & Wouters, B. (2019). Observing and Modeling Ice Sheet Surface Mass Balance. *Reviews of Geophysics*, *57*(2), 376–420. doi: 10.1029/2018RG000622

Li, W., Lhermitte, S., & López-Dekker, P. (2021). The potential of synthetic aperture radar interferometry for assessing meltwater lake dynamics on Antarctic ice shelves. *Cryosphere*, *15*(12), 5309–5322. doi: 10.5194/tc-15-5309-2021

Li, Z., & Wu, Q. (2022). Capturing the crack process of the Antarctic A74 iceberg with Sentinel-1 based offset tracking and radar interferometry techniques. *International Journal of Digital Earth*, *15*(1), 397–415. doi: 10.1080/17538947.2022.2032851

Libert, L., Wuite, J., & Nagler, T. (2022). Automatic delineation of cracks with Sentinel-1 interferometry for monitoring ice shelf damage and calving. *Cryosphere*, *16*(4), 1523–1542. doi: 10.5194/tc-16-1523-2022

Lima, L. S., Pezzi, L. P., Mata, M. M., Santini, M. F., Carvalho, J. T., et al. (2022). Glacial meltwater input to the ocean around the Antarctic Peninsula: Forcings and consequences. *Anais Da Academia Brasileira de Ciências*, *94*, e20210811. doi: 10.1590/0001-3765202220210811

Lipovsky, B. P. (2018). Ice Shelf Rift Propagation and the Mechanics of Wave-Induced Fracture. *Journal of Geophysical Research: Oceans*, *123*(6), 4014–4033. doi: 10.1029/2017JC013664

Lipovsky, B. P. (2020). Ice shelf rift propagation: Stability, three-dimensional effects, and the role of marginal weakening. *The Cryosphere*, *14*(5), 1673–1683. doi: 10.5194/tc-14-1673-2020

Liu, L., Dong, X., Lin, W., & Lang, S. (2023). Polar Sea Ice Detection Using a Rotating Fan Beam Scatterometer. *Remote Sensing*, *15*(20), 5063. doi: 10.3390/rs15205063

Liu, Y., Moore, J. C., Cheng, X., Gladstone, R. M., Bassis, J. N., et al. (2015). Ocean-driven thinning enhances iceberg calving and retreat of Antarctic ice shelves. *Proceedings of the National Academy of Sciences*, *112*(11), 3263–3268. doi: 10.1073/pnas.1415137112

Luckman, A., Elvidge, A., Jansen, D., Kulessa, B., Kuipers Munneke, P., et al. (2014). Surface melt and ponding on Larsen C Ice Shelf and the impact of föhn winds. *Antarctic Science*, *26*(6), 625–635. doi: 10.1017/S0954102014000339

Lumpkin, R., & Speer, K. (2007). *Global Ocean Meridional Overturning*. doi: 10.1175/JPO3130.1

MacAyeal, D. R., & Rignot, E. (1998). Ice-shelf dynamics near the front of the Filchner-Ronne Ice Shelf, Antaretica, revealed by SAR interferometry. *Journal of Glaciology*, *44*(147), 419–428. doi: 10.3189/S0022143000002744

MacAyeal, D. R., Scambos, T. A., Hulbe, C. L., & Fahnestock, M. A. (2003). Catastrophic ice-shelf break-up by an ice-shelf-fragment-capsize mechanism. *Journal of Glaciology*, *49*(164), 22–36. doi: 10.3189/172756503781830863

Macdonald, G. J. (2019). Investigating the Hydrology of Ice Shelves, and its Implications for Ice-Shelf Stability. *SSRN Electronic Journal*, (December).

Machguth, H., Box, J. E., Fausto, R. S., & Pfeffer, W. T. (2018). Melt Water Retention Processes in Snow and Firn on Ice Sheets and Glaciers: Observations and Modeling. *Frontiers in Earth Science*, *6*. doi: 10.3389/feart.2018.00105

Marsh, O. J., Price, D., Courville, Z. R., & Floricioiu, D. (2021). Crevasse and rift detection in Antarctica from TerraSAR-X satellite imagery. *Cold Regions Science and Technology*, *187*, 103284. doi: 10.1016/j.coldregions.2021.103284

Massom, R. A., Scambos, T. A., Bennetts, L. G., Reid, P., Squire, V. A., & Stammerjohn, S. E. (2018). Antarctic ice shelf disintegration triggered by sea ice loss and ocean swell. *Nature*, *558*(7710), 383–389. doi: 10.1038/s41586-018-0212-1

McGrath, D., Steffen, K., Holland, P. R., Scambos, T., Rajaram, H., et al. (2014). The structure and effect of suture zones in the Larsen C Ice Shelf, Antarctica. *Journal of Geophysical Research: Earth Surface*, *119*(3), 588–602. doi: 10.1002/2013JF002935

Meester, M. J., & Baslamisli, A. S. (2022). SAR image edge detection: Review and benchmark experiments. *International Journal of Remote Sensing*, *43*(14), 5372–5438. doi: 10.1080/01431161.2022.2131480

Miele, C., Bartholomaus, T. C., & Enderlin, E. M. (2023). Marginal Detachment Zones: The Fracture Factories of Ice Shelves? *Journal of Geophysical Research: Earth Surface*, *128*(6), e2022JF006959. doi: 10.1029/2022JF006959

Moctezuma-Flores, M., & Parmiggiani, F. (2016). SAR observations of the Nansen Ice Shelf fracture. *The European Physical Journal Plus*, *131*(11), 384. doi: 10.1140/epjp/i2016-16384-y

Morandeira, N. S., Grimson, R., & Kandus, P. (2016). Assessment of SAR speckle filters in the context of object-based image analysis. *Remote Sensing Letters*, *7*(2), 150–159. doi: 10.1080/2150704X.2015.1117153

Moreira, A., Prats-Iraola, P., Younis, M., Krieger, G., Hajnsek, I., & Papathanassiou, K. P. (2013). A tutorial on synthetic aperture radar. *IEEE Geoscience and Remote Sensing Magazine*, *1*(1), 6–43. doi: 10.1109/MGRS.2013.2248301

Morlighem, M., Rignot, E., Binder, T., Blankenship, D., Drews, et al. (2020). Deep glacial troughs and stabilizing ridges unveiled beneath the margins of the Antarctic ice sheet. *Nature Geoscience*, *13*(2), 132–137. doi: 10.1038/s41561-019-0510-8

Morris, A., Lipovsky, B. P., Walker, C. C., & Marsh, O. J. (2023). Measurement of Ice Shelf Rift Width with ICESat-2 Laser Altimetry: Automation, Validation, and the behavior of Halloween Crack, Brunt Ice Shelf, East Antarctica. *The Cryosphere Discussions*, 1–31. doi: 10.5194/tc-2023-63

Morris, E. M., & Vaughan, D. G. (2003). Spatial and Temporal Variation of Surface Temperature on the Antarctic Peninsula And The Limit of Viability of Ice Shelves. In *Antarctic Peninsula Climate Variability: Historical and Paleoenvironmental Perspectives* (pp. 61–68). American Geophysical Union (AGU). doi: 10.1029/AR079p0061

Motohka, T., Isoguchi, O., Sakashita, M., & Shimada, M. (2018). Results of ALOS-2 PALSAR-2 Calibration and Validation After 3 Years of Operation. *IGARSS 2018 - 2018 IEEE International Geoscience and Remote Sensing Symposium*, 4169–4170. doi: 10.1109/IGARSS.2018.8519118

Mouginot, J., Rignot, E., Scheuchl, B., & Millan, R. (2017). Comprehensive Annual Ice Sheet Velocity Mapping Using Landsat-8, Sentinel-1, and RADARSAT-2 Data. *Remote Sensing*, *9*(4), 364. doi: 10.3390/rs9040364

Neme, J., England, M. H., & McC. Hogg, A. (2022). Projected Changes of Surface Winds Over the Antarctic Continental Margin. *Geophysical Research Letters*, *49*(16), e2022GL098820. doi: 10.1029/2022GL098820

Neumann, T. A., Martino, A. J., Markus, T., Bae, S., Bock, M. R., et al. (2019). The Ice, Cloud, and Land Elevation Satellite – 2 mission: A global geolocated photon product derived from the Advanced Topographic Laser Altimeter System. *Remote Sensing of Environment*, *233*, 111325. doi: 10.1016/j.rse.2019.111325

Nicolas, J. P., Vogelmann, A. M., Scott, R. C., Wilson, A. B., Cadeddu, M. P., et al. (2017). January 2016 extensive summer melt in West Antarctica favoured by strong El Niño. *Nature Communications*, *8*(1), 15799. doi: 10.1038/ncomms15799

Oerter, H., Kipfstuhl, J., Determann, J., Miller, H., Wagenbach, D., et al. (1992). Evidence for basal marine ice in the Filchner–Ronne ice shelf. *Nature*, *358*(6385), 399–401. doi: 10.1038/358399a0

Orsi, A. H., Johnson, G. C., & Bullister, J. L. (1999). Circulation, mixing, and production of Antarctic Bottom Water. *Progress in Oceanography*, *43*(1), 55–109. doi: 10.1016/S0079-6611(99)00004-X

Pang, A., Liang, Q., Li, W., Zheng, L., Li, T., & Cheng, X. (2023). The distribution and evolution of surface fractures on pan-Antarctic ice shelves. *International Journal of Digital Earth*, *16*(1), 3295–3320. doi: 10.1080/17538947.2023.2246436

Parhad, S. V., Warhade, K. K., & Shitole, S. S. (2024). Speckle noise reduction in sar images using improved filtering and supervised classification. *Multimedia Tools and Applications*, *83*(18), 54615–54636. doi: 10.1007/s11042-023-17648-0

Parkinson, C. L., & Cavalieri, D. J. (2012). Antarctic sea ice variability and trends, 1979-2010. *The Cryosphere*, *6*(4), 871–880. doi: 10.5194/tc-6-871-2012

Parkinson, C. L. (2019). A 40-y record reveals gradual Antarctic sea ice increases followed by decreases at rates far exceeding the rates seen in the Arctic. *Proceedings of the National Academy of Sciences*, *116*(29), 14414–14423. doi: 10.1073/pnas.1906556116

Pohl, B., Favier, V., Wille, J., Udy, D. G., Vance, T. R., et al. (2021). Relationship Between Weather Regimes and Atmospheric Rivers in East Antarctica. *Journal of Geophysical Research: Atmospheres*, *126*(24), e2021JD035294. doi: 10.1029/2021JD035294

Pritchard, H. D., Ligtenberg, S. R. M., Fricker, H. A., Vaughan, D. G., van den Broeke, M. R., & Padman, L. (2012). Antarctic ice-sheet loss driven by basal melting of ice shelves. *Nature*, *484*(7395), 502–505. doi: 10.1038/nature10968

Qi, M., Liu, Y., Liu, J., Cheng, X., Lin, Y., et al. (2021). A 15-year circum-Antarctic iceberg calving dataset derived from continuous satellite observations. *Earth System Science Data*, *13*(9), 4583–4601. doi: 10.5194/essd-13-4583-2021

Qiu, F., Berglund, J., Jensen, J. R., Thakkar, P., & Ren, D. (2004). Speckle Noise Reduction in SAR Imagery Using a Local Adaptive Median Filter. *GIScience & Remote Sensing*, *41*(3), 244–266. doi: 10.2747/1548-1603.41.3.244

Racoviteanu, A. E., Williams, M. W., & Barry, R. G. (2008). Optical Remote Sensing of Glacier Characteristics: A Review with Focus on the Himalaya. *Sensors*, *8*(5), 3355–3383. doi: 10.3390/s8053355

Raphael, M. N., Hobbs, W., & Wainer, I. (2011). The effect of Antarctic sea ice on the Southern Hemisphere atmosphere during the southern summer. *Climate Dynamics*, *36*(7), 1403–1417. doi: 10.1007/s00382-010-0892-1

Rau, F., Braun, M., Saurer, H., Goßmann, H., Kothe, G., et al. (2000). *Monitoring Multi-Year Snow Cover Dynamics on the Antarctic Peninsula Using SAR Imagery*.

Recchia, A., Guidici, D., & Albinet, C. (2022). *SAOCOM 1 A/B Quality Assessment Summary*.

Rees, W. G. (2012). *Physical Principles of Remote Sensing* (3rd ed.). Cambridge: Cambridge University Press. doi: 10.1017/CBO9781139017411

Richards, J. A. (2009). *Remote Sensing with Imaging Radar*. Berlin, Heidelberg: Springer Berlin Heidelberg. doi: 10.1007/978-3-642-02020-9

Rignot, E., Jacobs, S., Mouginot, J., & Scheuchl, B. (2013). Ice-Shelf Melting Around Antarctica. *Science*, *341*(6143), 266–270. doi: 10.1126/science.1235798

Rignot, E., Mouginot, J., & Scheuchl, B. (2011). Ice Flow of the Antarctic Ice Sheet. *Science*, *333*(6048), 1427–1430. doi: 10.1126/science.1208336

Rignot, E., Bamber, J. L., van den Broeke, M. R., Davis, C., Li, Y., et al. (2008). Recent Antarctic ice mass loss from radar interferometry and regional climate modelling. *Nature Geoscience*, *1*(2), 106–110. doi: 10.1038/ngeo102

Rignot, E., Echelmeyer, K., & Krabill, W. (2001). Penetration depth of interferometric synthetic-aperture radar signals in snow and ice. *Geophysical Research Letters*, *28*(18), 3501–3504. doi: 10.1029/2000GL012484

Rignot, E., Mouginot, J., Scheuchl, B., van den Broeke, M., van Wessem, M. J., & Morlighem, M. (2019). Four decades of Antarctic Ice Sheet mass balance from 1979–2017. *Proceedings of the National Academy of Sciences*, *116*(4), 1095–1103. doi: 10.1073/pnas.1812883116

Ronneberger, O., Fischer, P., & Brox, T. (2015). U-Net: Convolutional Networks for Biomedical Image Segmentation. In N. Navab, J. Hornegger, W. M. Wells, & A. F. Frangi (Eds.), *Medical Image Computing and Computer-Assisted Intervention – MICCAI 2015* (pp. 234–241). Cham: Springer International Publishing. doi: 10.1007/978-3-319-24574-4_28

Rott, H., & Mätzler, C. (1987). Possibilities and Limits of Synthetic Aperture Radar for Snow and Glacier Surveying. *Annals of Glaciology*, *9*, 195–199. doi: 10.3189/S0260305500000604

Scambos, T. A., Hulbe, C., Fahnestock, M., & Bohlander, J. (2000). The link between climate warming and break-up of ice shelves in the Antarctic Peninsula. *Journal of Glaciology*, *46*(154), 516–530. doi: 10.3189/172756500781833043

Scambos, T., Fricker, H. A., Liu, C.-C., Bohlander, J., Fastook, J., et al. (2009). Ice shelf disintegration by plate bending and hydro-fracture: Satellite observations and model results of the 2008 Wilkins ice shelf break-ups. *Earth and Planetary Science Letters*, *280*(1), 51–60. doi: 10.1016/j.epsl.2008.12.027

Schoof, C. (2007). Ice sheet grounding line dynamics: Steady states, stability, and hysteresis. *Journal of Geophysical Research: Earth Surface*, *112*(F3). doi: 10.1029/2006JF000664

Shah, E., Jayaprasad, P., & James, M. E. (2019). Image Fusion of SAR and Optical Images for Identifying Antarctic Ice Features. *Journal of the Indian Society of Remote Sensing*, *47*(12), 2113–2127. doi: 10.1007/S12524-019-01040-3/FIGURES/13

Shah, E., Jayaprasad, P., James, M. E., Putrevu, D., & Misra, A. (2020). Changes in Antarctic Ice-Shelf Margins between 1997 and 2019 using Sentinel and Radarsat Data. *Current Science*, *119*(10), 1633. doi: 10.18520/cs/v119/i10/1633-1640

Shamsoddini, A., & and Trinder, J. C. (2011). Edge-detection-based filter for SAR speckle noise reduction. *International Journal of Remote Sensing*, *33*(7), 2296–2320. doi: 10.1080/01431161.2011.614286

Shepherd, A., Gilbert, L., Muir, A. S., Konrad, H., McMillan, M., et al. (2019). Trends in Antarctic Ice Sheet Elevation and Mass. *Geophysical Research Letters*, *46*(14), 8174–8183. doi: 10.1029/2019GL082182

Shepherd, A., Ivins, E. R., A, G., Barletta, V. R., Bentley, M. J., Bettadpur, S., et al. (2012). A Reconciled Estimate of Ice-Sheet Mass Balance. *Science*, *338*(6111), 1183–1189. doi: 10.1126/science.1228102

Shepherd, A., Wingham, D., Wallis, D., Giles, K., Laxon, S., & Sundal, A. V. (2010). Recent loss of floating ice and the consequent sea level contribution. *Geophysical Research Letters*, *37*(13). doi: 10.1029/2010GL042496

Shu, S., Liu, H., Frappart, F., Huang, Y., Wang, S., et al. (2018). Estimation of snow accumulation over frozen Arctic lakes using repeat ICESat laser altimetry observations – A case study in northern Alaska. *Remote Sensing of Environment*, *216*, 529–543. doi: 10.1016/j.rse.2018.07.018

Silva, T. a. M., Bigg, G. R., & Nicholls, K. W. (2006). Contribution of giant icebergs to the Southern Ocean freshwater flux. *Journal of Geophysical Research: Oceans*, *111*(C3). doi: 10.1029/2004JC002843

Silvano, A., Foppert, A., Rintoul, S. R., Holland, P. R., Tamura, T., et al. (2020). Recent recovery of Antarctic Bottom Water formation in the Ross Sea driven by climate anomalies. *Nature Geoscience*, *13*(12), 780–786. doi: 10.1038/s41561-020-00655-3

Smith, B., Fricker, H. A., Holschuh, N., Gardner, A. S., Adusumilli, S., et al. (2019). Land ice height-retrieval algorithm for NASA's ICESat-2 photon-counting laser altimeter. *Remote Sensing of Environment*, *233*, 111352. doi: 10.1016/j.rse.2019.111352

Surawy-Stepney, T., Hogg, A. E., Cornford, S. L., & Hogg, D. C. (2023). Mapping Antarctic crevasses and their evolution with deep learning applied to satellite radar imagery. *The Cryosphere*, *17*(10), 4421–4445. doi: 10.5194/tc-17-4421-2023

Swart, N. C., & Fyfe, J. C. (2013). The influence of recent Antarctic ice sheet retreat on simulated sea ice area trends. *Geophysical Research Letters*, *40*(16), 4328–4332. doi: 10.1002/grl.50820

Swithinbank, C. W. (1988). *Satellite Image Atlas of Glaciers of the World*.

Tedesco, M. (2015). *Remote Sensing of the Cryosphere*.

Tedesco, M., & Monaghan, A. J. (2009). An updated Antarctic melt record through 2009 and its linkages to high-latitude and tropical climate variability. *Geophysical Research Letters*, *36*(18). doi: 10.1029/2009GL039186

Thomas, E. R., Hosking, J. S., Tuckwell, R. R., Warren, R. A., & Ludlow, E. C. (2015). Twentieth century increase in snowfall in coastal West Antarctica. *Geophysical Research Letters*, *42*(21), 9387–9393. doi: 10.1002/2015GL065750

Turner, J., Lu, H., White, I., King, J. C., Phillips, T., et al. (2016). Absence of 21st century warming on Antarctic Peninsula consistent with natural variability. *Nature*, *535*(7612), 411–415. doi: 10.1038/nature18645

Turner, J., Phillips, T., Thamban, M., Rahaman, W., Marshall, G. J., et al. (2019). The Dominant Role of Extreme Precipitation Events in Antarctic Snowfall Variability. *Geophysical Research Letters*, *46*(6), 3502–3511. doi: 10.1029/2018GL081517

Turton, J. V., Kirchgaessner, A., Ross, A. N., & King, J. C. (2018). The spatial distribution and temporal variability of föhn winds over the Larsen C ice shelf, Antarctica. *Quarterly Journal of the Royal Meteorological Society*, *144*(713), 1169–1178. doi: 10.1002/qj.3284

Ulaby, F., & Long, D. (2014). *Microwave Radar and Radiometric Remote Sensing*. University of Michigan Press. doi: 10.3998/0472119356

Ulaby, F. T., & Stiles, H. W. (1981). Microwave response of snow. *Advances in Space Research*, *1*(10), 131–149. doi: 10.1016/0273-1177(81)90389-6

Ulaby, F. T., Stiles, W. H., & Abdelrazik, M. (1984). Snowcover Influence on Backscattering from Terrain. *IEEE Transactions on Geoscience and Remote Sensing*, *GE-22*(2), 126–133. doi: 10.1109/TGRS.1984.350604

van der Veen, C. J. (2002). Calving glaciers. *Progress in Physical Geography: Earth and Environment*, *26*(1), 96–122. doi: 10.1191/0309133302pp327ra

Vaughan, D. G., Marshall, G. J., Connolley, W. M., Parkinson, C., Mulvaney, R., et al. (2003). Recent Rapid Regional Climate Warming on the Antarctic Peninsula. *Climatic Change*, *60*, 243–274. doi: 10.1023/A:1026021217991

Walker, C. C., Bassis, J. N., Fricker, H. A., & Czerwinski, R. J. (2013). Structural and environmental controls on Antarctic ice shelf rift propagation inferred from satellite monitoring. *Journal of Geophysical Research: Earth Surface*, *118*(4), 2354–2364. doi: 10.1002/2013JF002742

Walker, C. C., & Gardner, A. S. (2019). Evolution of ice shelf rifts: Implications for formation mechanics and morphological controls. *Earth and Planetary Science Letters*, *526*, 115764. doi: 10.1016/j.epsl.2019.115764

Walker, C. C., Bassis, J. N., Fricker, H. A., & Czerwinski, R. J. (2015). Observations of interannual and spatial variability in rift propagation in the Amery Ice Shelf, Antarctica, 2002–14. *Journal of Glaciology*, *61*(226), 243–252. doi: 10.3189/2015JoG14J151

Wang, S., Alexander, P., Wu, Q., Tedesco, M., & Shu, S. (2021). Characterization of ice shelf fracture features using ICESat-2 – A case study over the Amery Ice Shelf. *Remote Sensing of Environment*, *255*, 112266. doi: 10.1016/j.rse.2020.112266

Wang, S., Liu, H., Jezek, K., Alley, R. B., Wang, L., et al. (2022). Controls on Larsen C Ice Shelf Retreat From a 60-Year Satellite Data Record. *Journal of Geophysical Research: Earth Surface*, *127*(3), e2021JF006346. doi: 10.1029/2021JF006346

Wearing, M. G., Hindmarsh, R. C. A., & Worster, M. G. (2015). Assessment of ice flow dynamics in the zone close to the calving front of Antarctic ice shelves. *Journal of Glaciology*, *61*(230), 1194–1206. doi: 10.3189/2015JoG15J116

Weiß, T. (2018). *SAR Pre-processing Documentation*.

Wright, N. C., & Polashenski, C. M. (2018). Open-source algorithm for detecting sea ice surface features in high-resolution optical imagery. *The Cryosphere*, *12*(4), 1307–1329. doi: 10.5194/tc-12-1307-2018

Xiao, W., Hui, F., Cheng, X., & Liang, Q. (2023). An automated algorithm to retrieve the location and depth of supraglacial lakes from ICESat-2 ATL03 data. *Remote Sensing of Environment*, *298*, 113730. doi: 10.1016/j.rse.2023.113730

Xu, C., Wang, Z., Zhai, X., Lin, W., & He, Y. (2023). SVM-Based Sea Ice Extent Retrieval Using Multisource Scatterometer Measurements. *Remote Sensing*, *15*(6), 1630. doi: 10.3390/rs15061630

Zhai, X., Xu, R., Wang, Z., Zheng, Z., Shou, Y., et al. (2023). Classification of Arctic Sea Ice Type in CFOSAT Scatterometer Measurements Using a Random Forest Classifier. *Remote Sensing*, *15*(5), 1310. doi: 10.3390/rs15051310

Zhang, Z., Yu, Y., Shokr, M., Li, X., Ye, Y., et al. (2022). Intercomparison of Arctic Sea Ice Backscatter and Ice Type Classification Using Ku-Band and C-Band Scatterometers. *IEEE Transactions on Geoscience and Remote Sensing*, *60*, 1–18. doi: 10.1109/TGRS.2021.3099835

Zhao, J., Liang, S., Li, X., Duan, Y., & Liang, L. (2022). Detection of Surface Crevasses over Antarctic Ice Shelves Using SAR Imagery and Deep Learning Method. *Remote Sensing*, *14*(3), 487. doi: 10.3390/rs14030487

Zhao, Z., Liu, Z., & Gong, P. (2012). Automatic extraction of floating ice at Antarctic continental margin from remotely sensed imagery using object-based segmentation. *Science China Earth Sciences*, *55*(4), 622–632. doi: 10.1007/s11430-011-4270-6

Zheng, K., Li, Q., Wang, Z., An, J., Huang, F., et al. (2024). CREVNet: A Transformer and CNN-Based Network for Accurate Segmentation of Ice Shelf Crevasses. *IEEE Geoscience and Remote Sensing Letters*, *21*, 1–5. doi: 10.1109/LGRS.2024.3407860

Zhu, T., Cui, X., & Zhang, Y. (2021). Analysis of temporal and spatial variability of fronts on the Amery ice shelf automatically detected using Sentinel-1 SAR data. *Remote Sensing*, *13*(17), 3528. doi: 10.3390/rs13173528

Zwally, H. J., Yi, D., Kwok, R., & Zhao, Y. (2008). ICESat measurements of sea ice freeboard and estimates of sea ice thickness in the Weddell Sea. *Journal of Geophysical Research: Oceans*, *113*(C2). doi: 10.1029/2007JC004284

Appendix

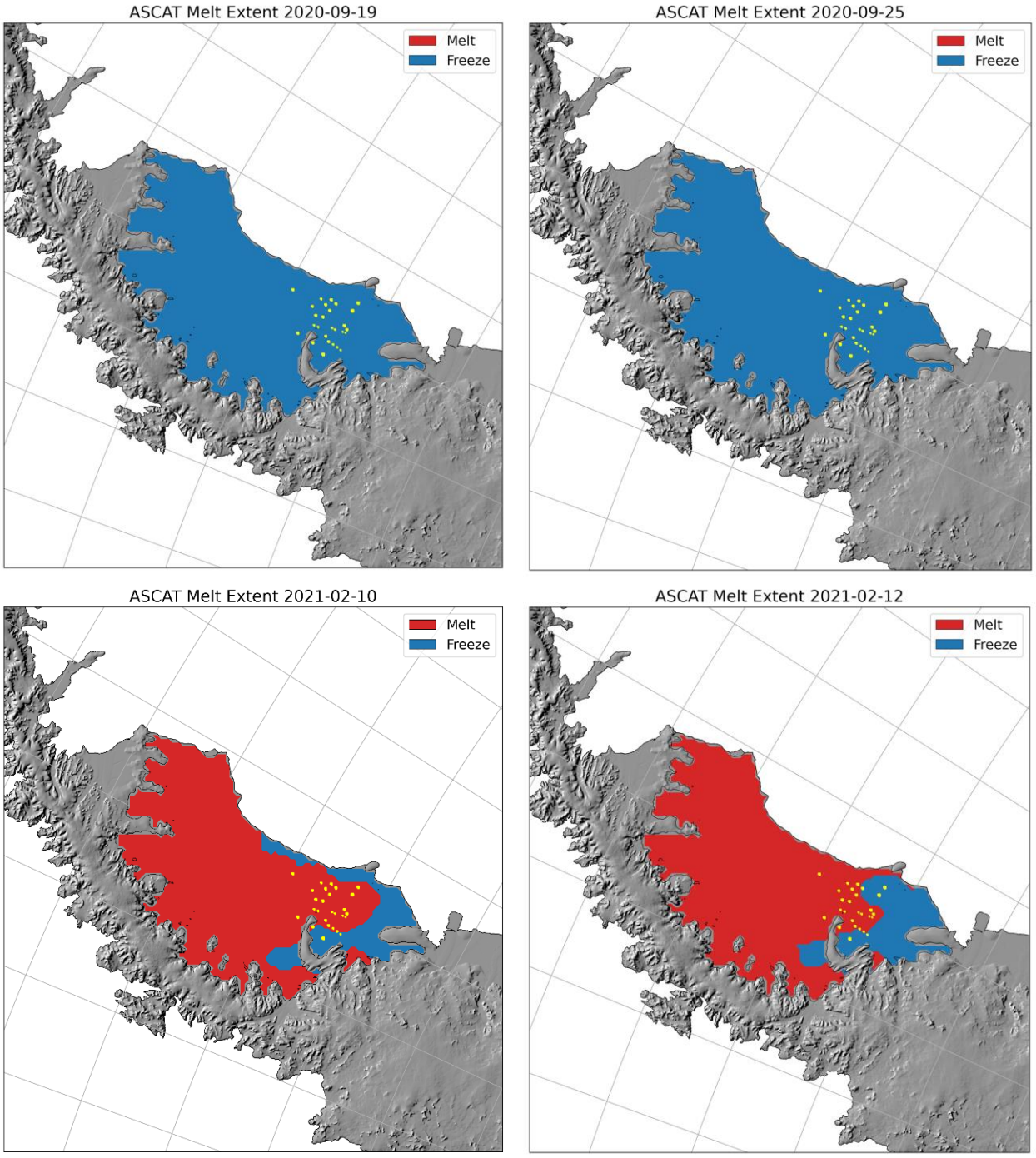

Figure A1. *Extent of ASCAT-derived melt for late winter and late melt SAR scene dates. From top left to bottom right: C-band late winter, L-band late winter, C-band late melt, and L-band late melt. Red indicates the presence of melt, blue indicates no melt.*

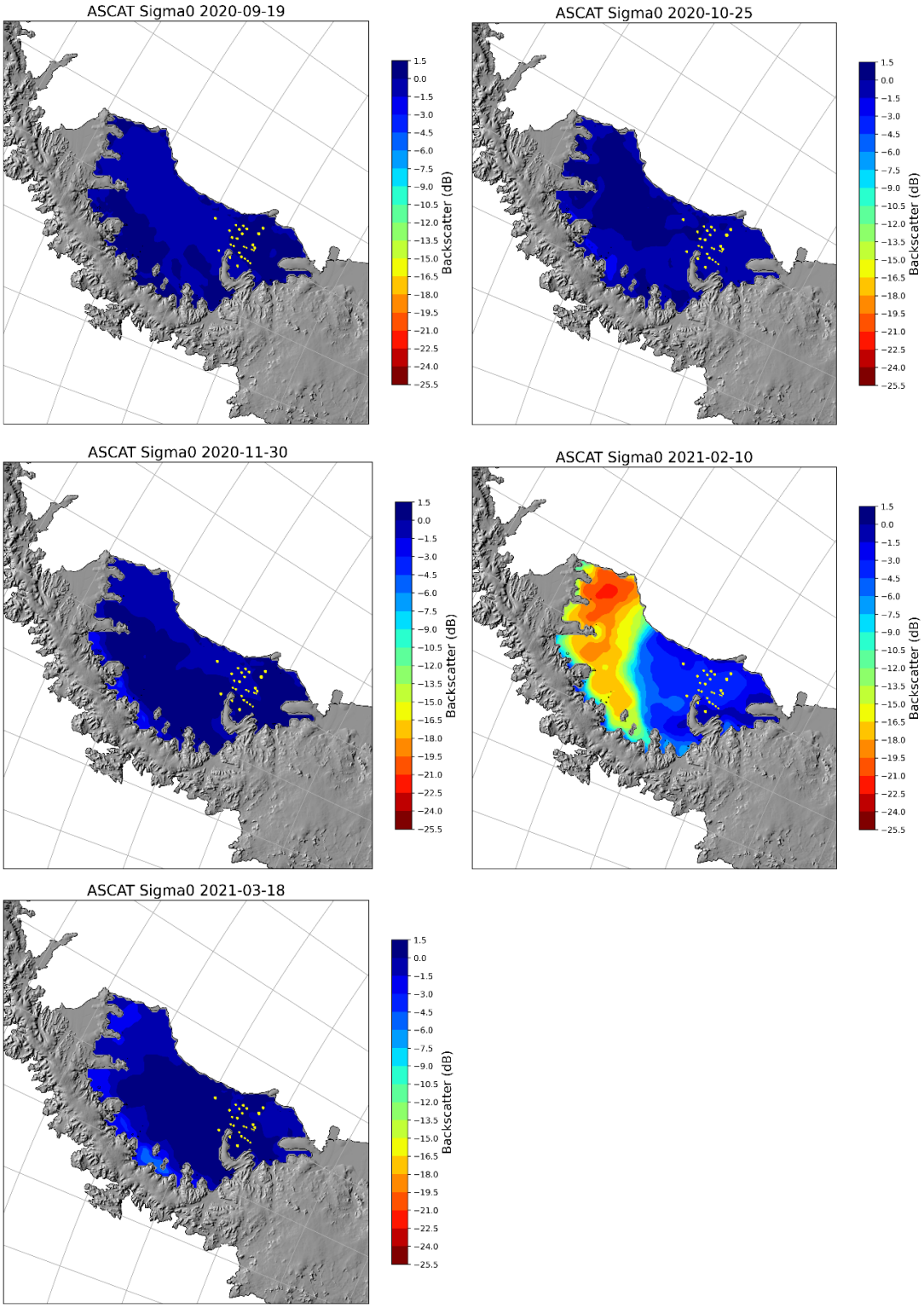

Figure A2. *Plots of ASCAT Sigma0 deviation from winter mean, for C-band SAR scenes. From top left to bottom right: late winter, early melt, melt onset, late melt, and freeze up.*

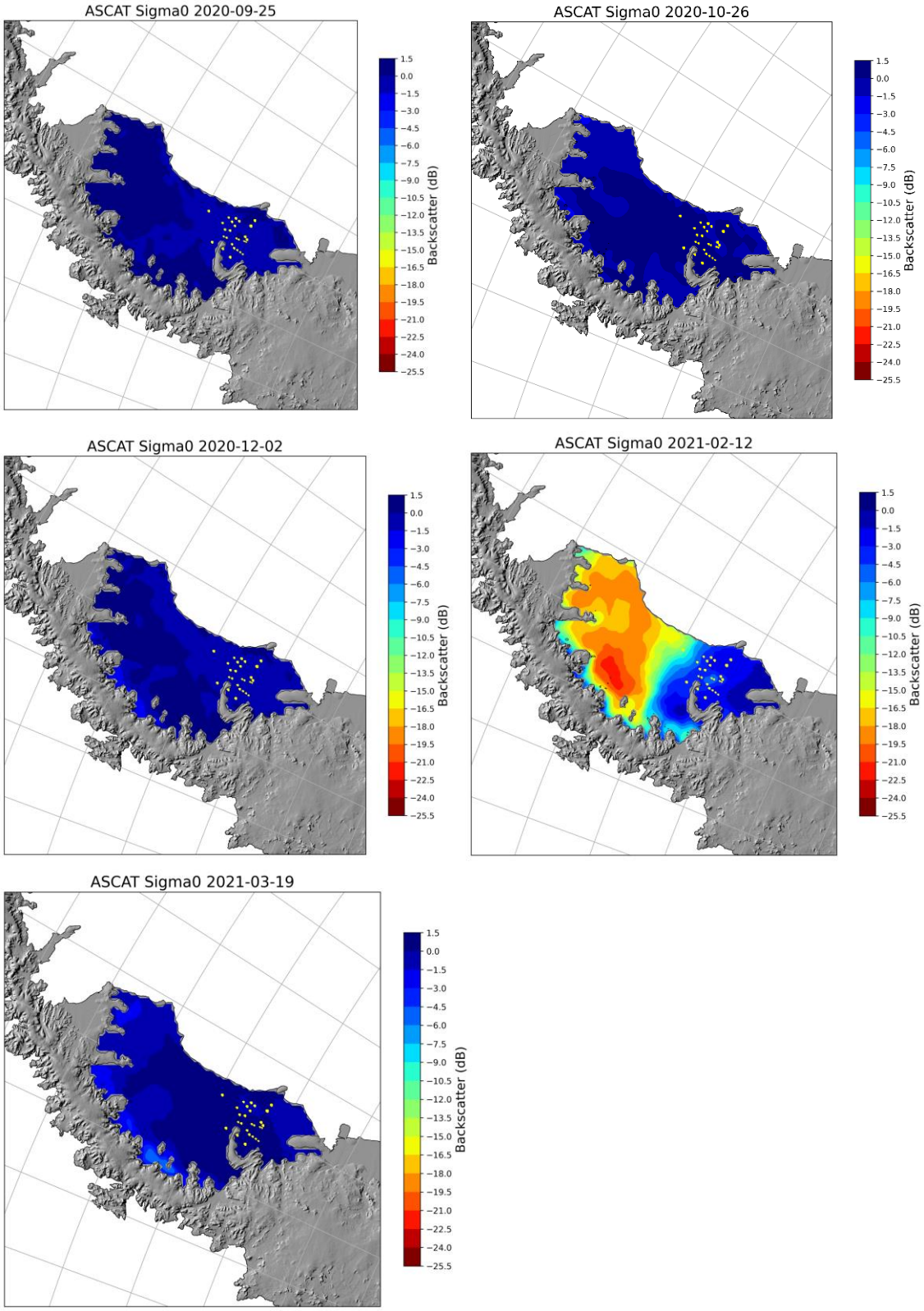

Figure A3. *Plots of ASCAT Sigma0 deviation from winter mean, for L-band SAR scenes. From top left to bottom right: late winter, early melt, melt onset, late melt, and freeze up.*

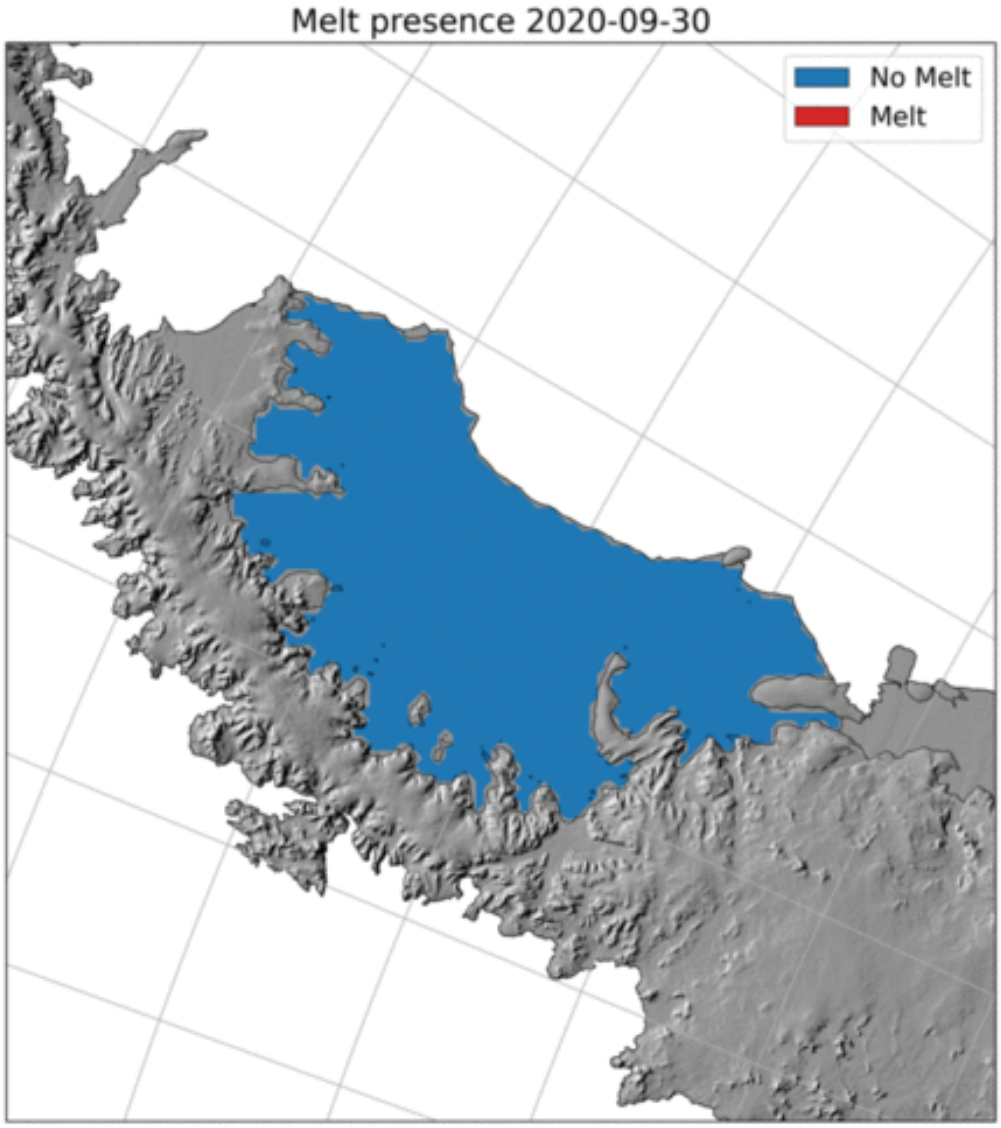

Figure A4. *Animated visualization of ASCAT-derived melt progression from September 2020 to April 2021. Melt is represented as a binary variable, with red indicating melt has been detected and blue indicating no melt.*